University of Alberta

Effect of Compressive Loading on Transport Properties of Cement-Based Materials

by

Meghdad Hoseini

A thesis submitted to the Faculty of Graduate Studies and Research
in partial fulfillment of the requirements for the degree of

Doctor of Philosophy
in
Structural Engineering

Department of Civil and Environmental Engineering

Dedication

To:

My Parents and My Lovely Wife, Gelareh

Abstract

The durability of concrete is one of its most important properties and has been an attractive subject for research in recent years. One of the criteria that affect concrete durability is permeability. Transport processes in concrete have been investigated for several decades. However, the correlation between transport coefficients and applied stress has received only little attention. On the other hand, measuring permeability involves a time-consuming test, with attendant concerns about system equilibrium and load control. Non Destructive Testing (NDT) of concrete makes it possible to obtain many test results from a single specimen and thus gives the opportunity to follow the changes in the properties of the specimen with time and under external influences. The scope of this study encompasses two major points of research focus. The first involves developing an experimental model for relating the permeability of cement-based materials under stress through non-destructive means, by measuring the Ultrasonic Pulse Velocity. The second part of this study examines the change in microstructure in cement-based materials under stress by employing x-ray tomography. A new parameter, pore connectivity, is introduced and was found to relate better to the permeability and damage caused by compressive stress. In all cases, the effect of fibre inclusion in mix designs is examined.

The results show that both permeability and ultrasonic pulse velocity are stress-dependent and there is a correlation between the change of permeability and ultrasonic pulse velocity in cement-based materials under stress. The proposed

permeability-UPV model has shown to have a good accuracy in predicting the permeability of concrete via a Non-Destructive Test method.

On the other hand, the presented method for determining the pore connectivity of cement-based materials, has shown a good agreement with the permeability results (which also depend on the interconnectivity of the voids and pores). This study showed that more than the creation of new voids, it is the forging of connectivity between existing pores and microcracks that leads to increases in permeability. Moreover, by introducing a damage value parameter, the onset of damage was found to occur around the same stress level that the sharp increase in permeability, UPV and pore connectivity happen. These findings support a design approach which limits service load stresses to 60% of peak capacity. The defined damage value parameter was also found to be a good criterion for examining the concrete structures under service conditions.

Acknowledgement

First, I would like to sincerely thank my supervisor, Dr. Vivek Bindiganavile, for his unrestricted support. Without him, this research would not have been possible. I particularly want to thank him for the opportunity given to me to pursue my interests in the field of concrete technology. He is not only a friendly advisor, but also a very intelligent person in solving the problems. He inspired me in every step of my research and helped me to enhance my knowledge as a student and also as a researcher.

I would like to thank Dr. Tayfun Babadagli for his technical support and contribution as a member of my advisory committee. Many thanks also to Professor Nemkumar Banthia at University of British Columbia for his technical support and advice during this research.

I wish to express my deep appreciation to Mr. Rizadly Mariano at the concrete laboratory; Mr. Greg Miller and Mr. Sean Watt at I.F. Morison Structural laboratory for their technical assistance in developing the permeability apparatus as well as setting up and maintenance of the MTS machine for this research. I am also thankful to Dr. Michael Doschak and Ms. Jillian Chapman for their skilled assistance in x-ray tomography scans. I am also grateful to the administrative staff of the Department of Civil and Environmental Engineering at University of Alberta for their assistance throughout the years.

I would like to express my gratitude to undergraduate summer students Mr. Zafir Lalani, Mr. Dennis Rosillo and Mr. Alexander O. Melnik for their help during summer months. I would also like to thank my fellow graduate students Mr. Mehrdad Mahoutian and Mr. Mohammad Mamun for the enjoyable moments that I had in working with them.

Words cannot express how I am indebted to my family, especially my mother and father, who have been unconditionally supporting me from the beginning of my life. None of my success would be possible without their dedication.

Finally, I would like to convey my special appreciation and gratitude to my wife, Gelareh, for the unconditional love, patience and dedication during my Ph.D. Studies. She has been helping me emotionally at all times especially when I was faced with difficult situations.

This project was financially supported by Cement Association of Canada and the Alberta Centre for Transportation Engineering and Planning (C-TEP). The continued support of the Natural Sciences and Engineering Research Council of Canada (NSERC) is also gratefully acknowledged.

Table of Contents

List of Figures

List of Tables

List of Symbols

A = permeation area (m^2); air content

a = mean radius of the cracks

α = specific surface area of the pores; a material constant

b = Klinkenberg coefficient; a parameter related to Poisson's ratio at zero porosity

C = ionic concentration (mol/l)

D = coefficient of Diffusion (m^2/s)

d, d_i = pore diameter

d_E = Damage value calculated from Modulus of elasticity change

d_v = damage value calculated from ultrasonic pulse velocity changes

E_d = Modulus of Elasticity

E_S = secant stiffness modulus of damaged material

E = secant modulus of elasticity in damaged specimen at different loading levels

E_0 = initial modulus of elasticity (undamaged specimen)

ε = strain

φ_c = connected porosity

φ_{co} = connected porosity under no stress

φ_t = total porosity

φ_{to} = total porosity under no stress

φ_0 = porosity of unstressed specimen

g = acceleration due to gravity

h = specimen's length (m)

Δh = pressure head (m)

η = dynamic viscosity of the fluid (N s/m^2)

I.d. = Inside diameter

J = molar flow rate (mol/m^2s); the volumetric flow rate (m/s)

K' = intrinsic permeability, which is independent of the fluid involved (m^2)

K = coefficient of water permeability

K_0 = permeability under no stress

k_l = coefficient of liquid permeabity

k_g = coefficient of gas permeability

L = specimen thickness or the length of flow path (m); void spacing factor

λ = second order elastic (SOE) constants generally known as Lame' constants

l = Murnaghan's third order elastic (TOE) constant

m = Murnaghan's third order elastic (TOE) constant

MSA = Maximum size aggregate

μ = second order elastic (SOE) constants generally known as Lame' constants

n = number of cracks per unit volume; Murnaghan's third order elastic (TOE) constant

n_i = number of voids with a particular diameter

ν = Poisson's ratio

ν_0 = Poissions's ratio f uncracked material

P = absolute inlet pressure (Pa); volume of paste in the cement-based material

P_a = atmospheric pressure

P_o = pressure at which the volume flow rate is determined

ΔP = pressure head (m)

Q = rate of flow of water (m^3/s)

R = area of the void

r_1 = inner diameter of the hollow cylinder (m)

r_2 = the outer diameter of the hollow cylinder (m)

ρ = density of the fluid (kg/m^3); density

ρ_0 = density in unstressed condition

S = void shape factor

σ = nominal values of stress; stress level

T = perimeter of the void

V = longitudinal ultrasonic pulse velocity of specimen at each stress level

V_0 = longitudinal ultrasonic pulse velocity of each specimen at zero stress.

V_s = shear wave velocity

V_p = surface wave velocity

V_p = longitudinal wave velocity

ΔV = change in ultrasonic pulse velocity

XRT = X-Ray tomography

1. Introduction

1.1. Problem Definition

During its service life, a reinforced concrete structure seldom sees the maximum loads it is designed to withstand. Nonetheless, failure of reinforced concrete does occur, and it is mainly due to deterioration in the quality of concrete with time. Of particular concern is the transport of deleterious fluids, which is an immediate cause for corrosion of the embedded steel and resultant loss in performance. While cement-based composites are inherently porous, the permeability of concrete is further aggravated by progressive cracking under service loads.

Permeability, defined as the movement of fluid under a pressure gradient, is one of the most important properties of concrete governing its long-term durability. The internal pore structure of concrete (number, size, distribution, and interconnectivity of the pores and cracks within concrete) is assumed to play a major role on water flow. These factors are affected by the mix design, conditions of curing and placement of concrete, as well as external loading and environment. Cracks provide connectivity to the flow path and decrease the resistance of the material to fluid flow. The effect of cracks on transport properties of concrete is important and must be understood from a material point of view. The effect of external loading on the permeability of water in cement-based media has not been studied widely in the past and even in the few available studies, there is a large discrepancy in the results reported in the literature. For example, the threshold stress level in compression (defined as the level of stress beyond which fluid permeability begins to rise) was found to lie anywhere between 30% and 90% of ultimate stress. This inconsistency may be attributed to the vast difference in the permeability test setups and the lack of a consistent definition as to what constitutes a simultaneous presence of load: for instance, whether the permeability is measured *under* the load or *after* removing the load. Moreover, establishing the steady state condition is vital to enable test repeatability and reproducibility as each data is obtained under the same state of flow.

Measuring permeability involves a time-consuming test, with attendant concerns about system equilibrium and load control. Therefore, a quick, simple and preferably in-situ test method for investigating the permeability of concrete structures in service is favorable. The use of ultrasonic waves to evaluate cement-based composites presents a non-destructive and readily repeatable test, and its use dates to the 1940s. Relating permeability with ultrasonic pulse velocity offers tremendous potential, especially in condition assessment of existing structures wherein a rapid and non-destructive test method is needed for durability evaluation of concrete.

On the other hand, since the permeability mostly depends on the interconnectivity of the pores and voids in cement-based materials, it is very valuable to be able to quantify the connected porosity and its change during different loading stages of structure. Moreover, many of the studies on the crack initiation and crack propagation in concrete under stress are limited to the crack investigation on the specimens' external surface and even the few reports that are available on the crack investigation in the specimen's volume, do not provide quantitative information on how the connectivity of the pores change under different levels of stress. Therefore, there is a need to study the three dimensional changes in the interconnectivity of the pores under application of different levels of stress.

The efforts presented in this study are designed toward establishing and using a correlation between the effect of stress on water permeability, ultrasonic pulse velocity, and pore connectivity in cement-based systems under compression.

1.2. Research Objectives and Scopes

The objectives of this research is to establish how the permeability of concrete changes with stress. This requires relating the permeability to stress-induced changes in the microstructure. One way of evaluating this using NDT is UPV, and correlating that to damage.

In order to achieve this goal, a multi-scale investigation was carried out. The study consists of four components: measurement of water permeability, evaluation of ultrasonic wave velocity, x-ray tomography and numerical modeling of stress-permeability-UPV. Specifically, the thesis has two distinctive objectives. The first is to examine the change in water permeability of cement-based materials under stress as predicted by the corresponding ultrasonic pulse velocity values. For this purpose, water permeability tests and ultrasonic wave velocity tests were carried out while the specimens were simultaneously under stress. The second objective is to quantify the change in the three-dimensional microstructure and pore connectivity of the cement-based materials under different levels of loading. The x-ray tomography technique was employed to study the specimens' micro-structures. The state of mechanical stress-induced damage has been examined and quantified in both of these research stages.

The scopes of this research include:

- Literature review on the permeability and UPV measured through the concrete under the effect of stress, as well as a review of the application of x-ray tomography in studying cement-based materials;
- Develop a permeability cell to measure the permeability of concrete under simultaneous effects of compression stress under the steady state condition of flow;
- Measurement of UPV through concrete in the presence of stress;
- Employment of the x-ray tomography technique to investigate the effect of stress on the three-dimensional microstructure of mortar specimens and to quantify the connected porosity in cement-based materials

1.3. Outline of the Thesis

This thesis consists of eleven chapters. In this chapter, Chapter 1, an introduction including problem definition, research objectives and scopes as well as significance of research are described. In Chapter 2, a comprehensive literature review on the effect of stress on permeability of water in cement-based materials is presented. The main focus is on the permeability mechanisms and its variation in the presence of stress. The experimental methods developed by different researchers to investigate the stress-dependency of permeability in cement-based materials are described. Finally, the effect of different parameters such as loading history, loading levels, mix design and reinforcement are reviewed. Chapter 3 reviews the previous studies on the variation of Ultrasonic Pulse Velocity (UPV) measured through concrete in the presence of stress. In this chapter, after introducing the different types of waves travelling in materials, the propagation of UPV in both unstressed and stressed cement-based materials is reviewed.

Chapter 4 provides information on the application of x-ray tomography in studying cement-based materials. This chapter describes specifically how to employ this technique for investigating the three-dimensional microstructure of mortar and concrete. Chapter 5 presents the experimental program for this study. Mix designs, specimen preparation, setup for mechanical testing, permeability setup, UPV measurement method, and the x-ray tomography technique including image acquisition and method of analysis of images employed in the present study are described in detail.

Chapter 6 presents and discusses the results of the experiments described in the previous chapter and the effect of stress on permeability, UPV and microstructure of mortar and concrete. In Chapter 7, stress-induced damage in cement-based materials is examined by two different methods and the relationship between the permeability and a damage parameter introduced in this chapter is presented.

Chapter 8 introduces a new method for quantifying the number of connected pores in cement-based materials using the x-ray tomography scan method. In particular, the difference between connected components and connected pores are explained and, by using a connected component labeling algorithm, the number of connected pores in specimens at each stress level is calculated. Moreover, a parameter called “connected porosity” is introduced to quantify the pore connectivity.

In Chapter 9 the relations between pore connectivity and other parameters such as permeability, UPV, and damage are illustrated and the effectiveness of application of “connected porosity” in micro-crack models is investigated. Chapter 10 provides the correlations between permeability and UPV in stressed concrete using the experimental results of previous chapters. Moreover, in this section, by using available analytical models and relationships between stress, permeability and UPV, a new permeability-UPV model is introduced and calibrated.

Finally, Chapter 11 relates the findings of the research to its goals and provides recommendations for future studies.

1.4. Significance of the Research

The work on which this document is based, generated the most data available on the effect of stress on permeability and ultrasonic pulse velocity of plain and fiber reinforced cement-based materials. It is also the first work that develops a model for predicting the change of water permeability of cement-based materials under stress by measuring the corresponding ultrasonic pulse velocity values. Moreover, this research is one of the few efforts to investigate the three-dimensional microstructure in cement-based systems by measuring the interconnectivity of the pores in cement-based materials and is the first attempt to quantify the change in pore connectivity of these materials under different levels of stress up to the ultimate.

The study determines how the effect of stress-induced damage on transport properties could have an impact on design and construction procedures in regard to limiting service load stresses. This information could also be useful in condition evaluation of concrete structures by employing non-destructive test methods in predicting changes in transport properties over the service life of the structure.

2. Permeability of Cracked Concrete

2.1. Introduction

The problem of deteriorating infrastructure due to the corrosion of reinforcement in concrete has taken on urgency in North America. A turn of the century estimate in the United States puts the cost of corrosion damage caused by deicing and sea salt on highway bridges at over US$ 150 billion [1]. Here in Canada, of an estimated 80,000 bridges, approximately 50% have an average age between 30 and 45 years, and many of them require major rehabilitation if not complete replacement. Alarmingly, with between 150 to 200 bridges taken out of service each year, it is estimated that nearly $50 billion CDN is required to restore them to their original functionality [2]. According to Alberta Infrastructure and Transportation, between 2002 and 2012 about 2500 bridges must be replaced in Alberta alone, which requires $40 million CDN per year at 2002 costs [3].

During their service life, concrete structures are subjected to different types of distress (mechanical, thermal and chemical). Generally, service loads by themselves are not enough to cause significant degradation to the mechanical properties of structural concrete [4]. However, with time the degradation accumulates, which leads to cracking, and in turn, to an increase in permeability [5]. It is well known that corrosion of embedded steel depends upon the availability of oxygen, moisture and chlorides around the reinforcement [1]. Progressive cracking creates a path of ingress for water, chlorides or other deleterious agents, which in turn leads to the corrosion of embedded steel. Thus, the transport properties of concrete (notably, permeability and diffusion) directly impact the durability of a reinforced concrete structure. Clearly, characterizing the mechanical properties alone is not adequate to describe the durability of concrete. However, there exists very limited documentation on how the transport properties of concrete are affected by the application of mechanical stress. Conventional assessment of the effect of mechanical loads on permeability or diffusion is based on first inducing damage in a specimen and then evaluating the transport property (subsequent to the stress test). For instance, Samaha and Hover [6] did not find any correlation between compressive strength and mass transport properties of concrete, up to 75% of the failure load. However, in service conditions, the ingress of harmful agents occurs even as the structure is under load and hence it is essential to evaluate the transport properties of concrete under the simultaneous application of stress. This chapter offers a review of the state-of-the-art on this subject. Only such stress as is induced due to the direct application of mechanical loading will be considered so that others (due to shrinkage, thermal and creep effects) will not be included in this discussion. A short description of transport properties in uncracked concrete is followed by an account of test methods in vogue for evaluating fluid transport in cracked concrete. The review summarizes the effect of loading type, crack dimensions, admixtures and fibre reinforcement on fluid and ion transport in concrete under an applied load.

2.2. Transport properties of uncracked concrete

Steel reinforcement, when embedded in concrete, is protected from exposure to deleterious liquids and gases that could otherwise result in corrosion. For, as is well known, an increase in the chloride ion-to-hydroxyl ion ratio (Cl^-/OH^-) destroys the passivation film protecting the rebar and leads to the initiation of corrosion which in the presence of readily available oxygen accelerates the progressive corrosion of rebars [1, 7].

There are various transport mechanisms that a fluid can undergo in concrete namely, permeability, diffusion, absorption, migration, and convection [8]. In some cases, e.g. the tidal zone of a marine environment, the movement of fluid through concrete can also be due to the combination of two or more of the mechanisms listed above [9]. In all cases, it is the connected porosity, which is the degree of continuity of the pore system, that significantly affects the transport properties of concrete [10]. The two most important mechanisms of transport of fluids within concrete from the durability point of view are permeability and diffusion as discussed in the following sections.

2.2.1. Permeability

The permeability of concrete is defined as the transport of fluid through it due to a pressure gradient. It depends largely on microcracking within concrete and the interconnected pore network within the hydrated cement paste. While the former can be the result of applied stress, the latter is related to the mix design, curing and placement technique [11, 12]. Quantitatively, permeability is understood as a transport mechanism by bulk flow and is described as follows [13]:

$$J = -\frac{K\prime}{\eta}\, grad\,(\mathrm{P}) \qquad 2.1$$

Where, J is the volumetric flow rate (m/s), k´ is the intrinsic permeability (m^2), η is the dynamic viscosity (kg/ms) and P is the pressure (Pa).

As water is the most significant fluid that flows through concrete and given also that it is the chief agent for soluble aggressive ions that cause the chemical degradation of concrete, it is customary to examine water permeability in concrete. Darcy's Law is applied in determining the coefficient of water permeability of concrete assuming a slow, unidirectional and steady flow. The general form of Darcy's law for a laminar flow through a porous medium can be illustrated as Figure 2. 1 and written as Equation 2.2 [12]. It should be noted that for comparing the permeability of concrete samples obtained from tests using different liquids, the "intrinsic permeability", K', which in theory is only dependent on the pore structure of the concrete is defined as follows:

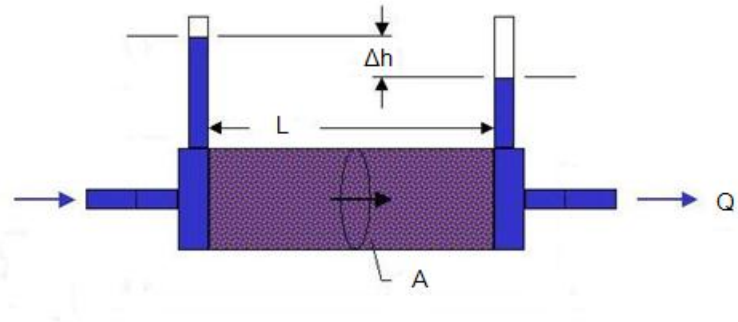

Figure 2. 1. Schematic Illustration of Darcy's Law

$$K' = Q\frac{1}{A}\frac{\eta}{\rho g}\frac{L}{\Delta h} \qquad 2.2$$

Where:

K' = intrinsic permeability, which is independent of the fluid involved (m^2)

Q = rate of water flow (m^3/s)

A = permeation area (m^2)

Δh = pressure head (m)

L = specimen thickness or the length of flow path (m)

η = dynamic viscosity of the fluid ($N\ s/m^2$)

ρ = density of the fluid (kg/m^3)

g = acceleration due to gravity

The coefficient of water permeability, K, is thus given by:

$$K = \frac{K'\rho g}{\eta} \quad 2.3$$

From Equations 2.2 and 2.3, this coefficient may be expressed as:

$$K = \frac{QL}{A\Delta h} \quad 2.4$$

Rewriting Equation 2.3 in terms of the intrinsic permeability, we have:

$$K' = \frac{K\ \eta}{\rho\ g} \quad 2.5$$

For water, ρ=1000 kg/m^3, η= 1 centipoises (= 10^{-3} Ns/m^3) and g= 9.81 m/s^2, hence

$$K' = K \times \frac{10^{-3}}{1000 \times 9.81} = 1.02 \times 10^{-7} K_w \quad 2.6$$

Or

$$K = 9.8 \times 10^{6} K' \quad 2.7$$

Therefore, for water at 20°C, the Darcy permeability coefficient (m/s) is approximately 9.8 $\times 10^6$ times the intrinsic permeability coefficient (m^2).

For gases, the intrinsic permeability can be calculated by the Hagen–Poiseuille equation, which for the laminar flow of a compressible viscous fluid through a porous body under steady-state conditions is given by:

$$K' = \frac{Q}{A}\frac{2\eta L P_0}{(P^2 - P_a^2)} \qquad 2.8$$

Where P = absolute inlet pressure (Pa), P_a = outlet pressure, assumed in this test to be equal to the atmospheric pressure (Pa), and P_o = pressure at which the volume flow rate is determined, (Pa) taken here as the atmospheric pressure.

It has been found that for typical gases such as nitrogen and oxygen, at normal pressures the coefficient of gas permeability (m/s), can be calculated by [14]:

$$K_g = 6.5 \times 10^5\, K' \qquad 2.9$$

As stated before, in theory, the intrinsic permeability in porous media for water and gas should be similar but, test results have shown that there are large differences between values obtained for gases (i.e. nitrogen) and water, with the permeability of nitrogen being one or two orders of magnitude higher than that of water [15]. This difference was first noted by Klinkenberg in 1941 in his study on oil sands [16]. He also found that the difference between liquid and gas permeability were small for a highly permeable medium whereas for a medium of relatively low permeability, this difference was high. He explained this difference by the gas slippage theory whereby the layer of gas closest to the wall has a finite velocity (velocity at the pore wall is different from zero). So, the quantity of gas flowing in a capillary is larger than it would be expected by Equation 2.8 [15]. From the gas slippage theory, the flow of gas is affected by applied pressure. Klinkenberg derived an equation that relates gas or liquid intrinsic permeability coefficient (k_g and k_l, respectively) to the mean pressure (P_m):

$$k_l = \frac{k_g}{(1 + \frac{b}{P_m})} \qquad 2.10$$

Where b is the Klinkenberg coefficient which was derived by Bamforth for concrete as [15]:

$$b = 1.635 \times 10^{-8} \, {k_l}^{-0.5227} \qquad 2.11$$

The intrinsic water permeability of a typical structural concrete lies in the range of 10^{-19} to 10^{-17} m^2 [17] and gas permeability values have been found to be one or two orders of magnitude higher [15].

2.2.2. Diffusion

Diffusion is defined as the transport of a fluid due to a gradient in ionic concentration. It is concerned with the motion of individual ions and in general, can be stated as [13]:

$$J = -D\ grad(C) \qquad 2.12$$

Where, J is the molar flow rate (mol/m^2s), D is the coefficient of Diffusion (m^2/s) and C is the ionic concentration (mol/l). By Fick's Second Law [18], for a non-steady state and one-dimensional diffusion process, the chloride concentration C at a location, X, and time, t, is given by:

$$\frac{\partial C}{\partial t} = D\ \frac{\partial^2 C}{\partial X^2} \qquad 2.13$$

Where, D, is the coefficient that describes the ease of mass transfer by means of diffusion. The coefficient of diffusion is affected by factors such as mix proportions and composition, local concentration of ions (e.g. chlorides), maturity, ambient conditions and the duration of exposure, [9, 19, 20]. The chloride diffusion coefficient of concrete has been reported between 0.1×10^{-12} m^2/s to 25×10^{-12} m^2/s [7, 21].

2.3. Effect of Fiber Reinforcement

The role of fibers in concrete is to inhibit the brittle nature of the material by imparting post cracking strength and toughness to the composite. Banthia and Bhargava [22] observed that purified plantation softwood fibers can reduce the permeability of unloaded concrete proportional to the fiber volume fraction used in concrete. Vondran and Webster [23] also found that water permeability, cracking and steel corrosion is reduced when adding polypropylene fibers to concrete. This result concurs with the findings of Harovel [24] but results of other studies do not necessarily agree [25, 26]. For instance, based on electrical resistivity and water absorption, Hamid et al. [25] observed that the addition of polypropylene fibers does not significantly affect the permeability or corrosion of reinforcement in concrete. Also, Sanjuan et al. [27] did not obtain a clear correlation between cracking in concrete and the corrosion of reinforcement, although they noticed that the mixes containing fibers had fewer cracks and also a lower electro-chemical activity.

2.4. Effect of Mechanical Stress on the Transport Properties of Concrete

2.4.1. Test methods

A summary of the various test methods in existence and their salient findings is presented in Table 2.1 and is discussed on the basis of test parameters in the following sections. While several techniques and test methods have been standardized to measure the permeability of concrete independent of stress [17, 28-32], those devised to evaluate permeability under stress are rather varied. These techniques and their intended outcome may be classified on the basis of i) the permeater, ii) load configuration and iii) instance when the permeability is measured. On this basis, one finds studies on the permeability of i) water [22, 33-39] and nitrogen gas [40-42]; ii) under compression [6, 22, 42, 43], tension [44, 45] and flexure [46]; and iii) measured in the presence of load [22, 36-38, 47] or after unloading [33, 35, 48].

Author	Fluid Examined	Stress State/ compressive strength at test/ Parameter Examined	Remarks
Kermani [15]	Water	Compression/ 30 MPa/ Effect of Mix Composition such as Fly-Ash and Air Entrainers	The specimens were subjected to elevated water pressure and were kept for 5 minutes at each stress level. The corresponding permeability was measured after unloading.
Tsukamoto [40]	Water, Oils & Other Organics	Tension / 55 MPa / Effect of aggregate size, fiber type and size & fiber dosage and fluid viscosity.	The specimen was subjected to 1.4 m column of water pressure. The permeability was measured under load.
Wang et al. [16], Aldea et al. [18,29]	Water	Splitting tension / 45 MPa / Effect of crack width and matrix strength.	Cracks were generated by a feedback controlled splitting tensile test method. Permeability was measured after unloading. (Figure 1-a)
Aldea et al. [18,38],		Permeability of cracked loaded concrete specimen under steady state condition.	
Rapoport et al. [19,20]		Splitting tension / Effect of steel fibers	
Lawler et al. [26,43]	Water	Uniaxial tension / Effect of steel and polymer Micro and macro fibers, hybrid fiber blends.	Data analyzed based on the flow rate measured under unloading. Test set-up shown in Figure 1-b was based on that developed by Ludirdja et al. [27]. Stable test regime was enforced by means of the Partial Elastic Subtraction Method [43,44] to obtain the feedback signal.
Banthia & Associates [14,21,25,45]	Water	Compression / 18 MPa/ Effect of load level, load history and fiber type and dosage	Permeability of concrete was measured on hollow cylindrical cores during compression in a steady state flow condition (Figure 1-c)
Hearn & Associates [22,31,46]	Water and Nitrogen gas	Mortar in compression / 65 MPa/ The mortar disks were vacuum saturated according to AASHTO T-227 [32]	The cracks were induced first corresponding to a strain of 3000 $\mu\varepsilon$ and the permeability was measured after loading. (see Figures 1-d)
Sugiyama et al. [26] Hearn et al. [38]	Nitrogen Gas	Compression / 25-40 MPa/ Effect of concrete density.	Gas flow was perpendicular to the direction of compression. Permeability measured during load (See Figure 1-e)
Picandet et al. [24]	Nitrogen Gas	Compression / 65 MPa/ Effect of strain levels.	Intrinsic permeability was calculated from the Hagen–Poiseuille relationship [47] assuming laminar flow and steady-state conditions. (Figure 1-f). Permeability was measured on a sample extracted after unloading.
Choinska et al. [2]	Nitrogen Gas	Compression / 30 MPa/ Effect of preloading and freshly imposed stress levels	Permeability tests were performed on hollow cylindrical specimens, taken after having been tested in compression, under a steady radial gas flow state (See Figure 1-g)
Samaha and Hover[6]	Chloride	Compression / Effect of load level and cumulative crack length on mixes containing fly ash and air entraining agents	Hollow concrete disks taken after unloading were indirectly assessed for chloride permeability as per ASTM C1202 [48]
Saito & Ishimori [30]	Chloride	Compression / 25 MPa/ Effect of monotonic and cyclic loading	Chloride Permeability was indirectly measured after unloading at each load level according to AASHTO T277 [33]

Table 2.1. A Summary of Test Methods and Remarks on Testing Scheme

2.4.1.1. Water or Liquid Permeability

One of the earliest to study water permeability in concrete under stress was Kermani [33]. He examined ordinary structural concrete (without an admixture) and two mixes – one containing fly ash and the other containing an air entraining agent. The specimens were subjected to a water pressure of 10.5 MPa and were kept for 5 minutes at each stress level before the corresponding permeability was measured. Tsukamoto [49] examined the fluid permeability in stressed concrete containing fibers. Subsequently, investigators at Northwestern University [34, 35, 48] measured the coefficient of water permeability for cracked unloaded concrete specimens. These cracks were generated by a feedback controlled splitting tensile test, Figure 2.1. They used a water pressure head of about 300 mm on the concrete specimen that had been prepared prior to the test by vacuuming and saturation in accordance with AASHTO T277 [50]. A steady state flow was attained in about 7 days at which time Darcy's law was applied to calculate the coefficient of water permeability. While the afore mentioned studies [34, 35, 48] measured the water permeability of cracked, unloaded concrete specimens, Aldea et al. [36, 51] and Rapoport et al. [37, 38] used the same apparatus to study the water permeability of concrete specimens under load.

Lawler et al. [44] developed a test configuration to evaluate water permeability in mortar specimens, cut from the ends of flexural testing specimens after test, subjected to uniaxial tensile load. They modified the test set-up described by

Ludirdja et al. [45]. Noting that the majority of flow in cracked materials occurs through the crack (and not through the bulk material), they analyzed the results of their tests based on the flow rate instead of on the permeability coefficient. A schematic view of their test setup is illustrated in Figure 2.2. A water pressure of 13.8 kPa was achieved during the test. Water travelling through the specimen was collected and weighed in a box on the opposite side. The total duration for each test specimen, including the time required to seal it, was about 48 hours. They recorded the weight of water that was gathered in the box every 30 seconds and from this, they could compute the rate of flow relative to the tensile stress-strain response.

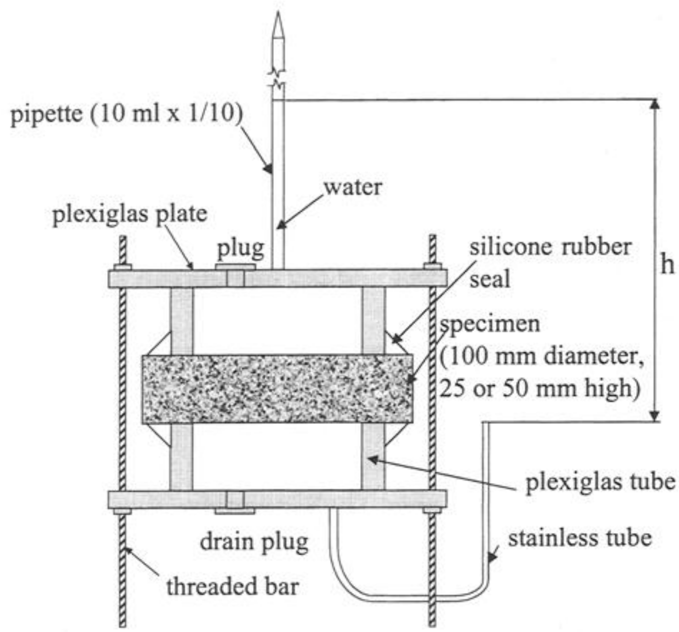

Figure 2.1. Schematic View of the Water Permeability Apparatus Developed and Used by Wang et al. [34] and Aldea et al. [35, 48]

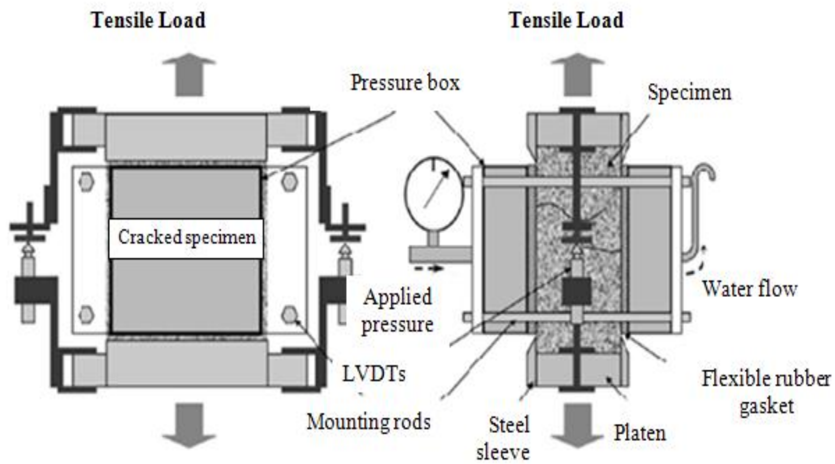

Figure 2.2. Test Set -up Developed by Ludirdja et al. [45]

In addition to monitoring permeability in mortar, Lawler et al. [52] also evaluated the permeability in pre-cracked concrete. For this purpose, the apparatus shown in Figure 2.2 was further modified using a stiffer test machine and a stable test regime was enforced by means of the Partial Elastic Subtraction Method [52, 53] to obtain the feedback signal. This method measures the total specimen deformation and subtracts part of the elastic deformation, leaving inelastic deformation as a stable feedback signal.

Hearn et al. [54] developed a permeameter suitable for measuring both water and gas flow in concrete. The apparatus comprised of a permeability cell (Figure 2.3), where in concrete disks were vacuum saturated according to AASHTO T227 [50] and were sealed with a silicone rubber sleeve. These disks (between 100 to 150 mm in diameter and 40 mm thick) were sawn from a midsection of an oven-dried concrete cylinder, which was previously compressed to predetermined stress values. They monitored both the inflow and the outflow and the compressive stress was applied by means of the piston as shown (Figure 2.4). This apparatus was employed to investigate the effect of load-induced cracking on the water permeability of concrete, where permeability was measured after loading.

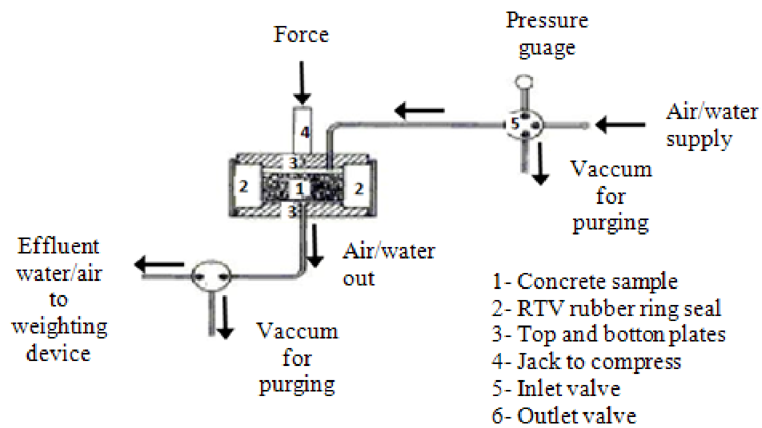

Figure 2.3. Permeability Cell Developed by Hearn et al. [54] for Measuring Both Water and Gas Permeability

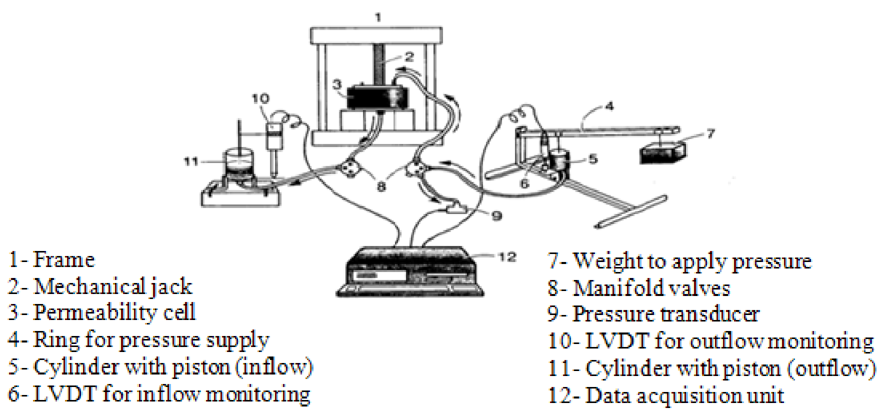

Figure 2.4. Permeameter for Investigating the Effect of Load-induced Cracking on Permeability of Concrete [54]

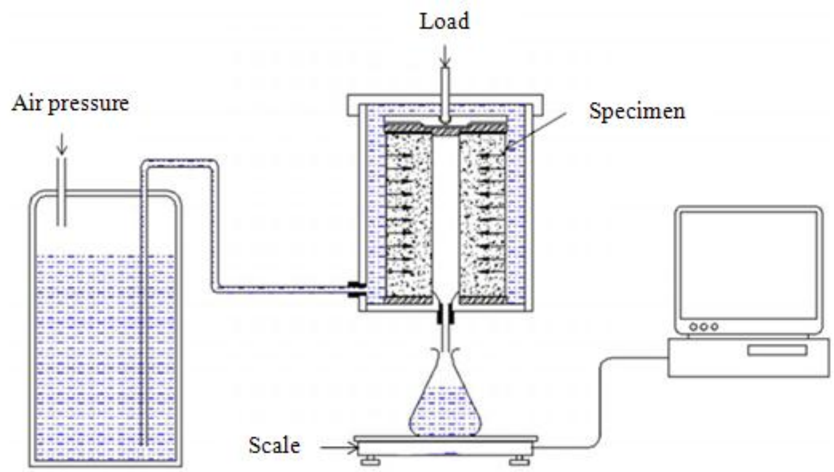

Figure 2.5. Permeability Apparatus Developed by Banthia and Biparva [39].

Studies by Banthia and his associates [22, 39, 43] describe the permeability of concrete on hollow cylindrical cores under compression. They assembled two permeability cells with identical concrete specimens in them (Figure 2.5). One of the cells was placed in a Universal Testing Machine (UTM) whereby a constant stress was applied to the hollow specimen while the other cell remained outside the UTM under conditions of zero stress. The flow of water in both cells prior to loading was kept identical. By measuring the mass of the water permeated through the two cells (collected in separate collection reservoirs) as a function of time and by applying Darcy's law, they calculated the water permeability of concrete in compression. For the set-up shown in Figure 2.5, it took about 30 hours to achieve a condition of full flow equilibrium under the tested water pressure of 0.48 MPa.

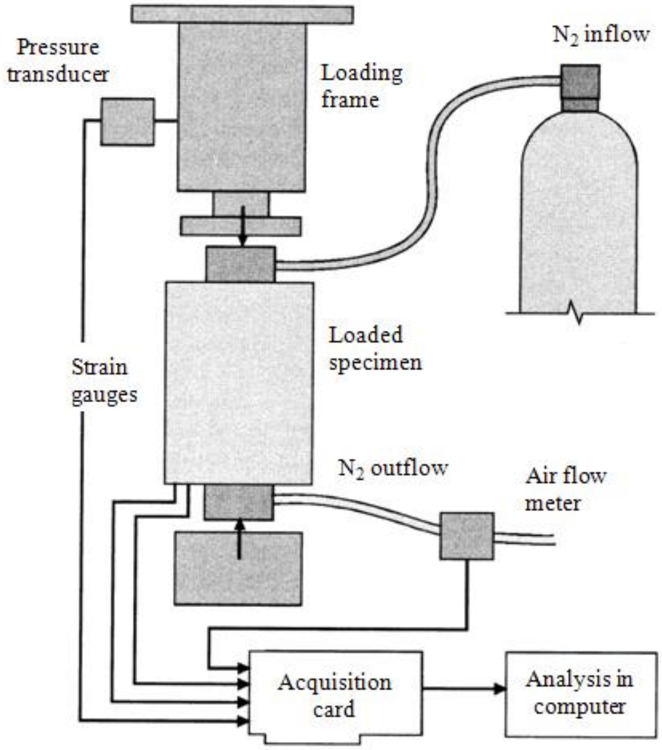

Figure 2.6. Apparatus Developed by Hearn and Lok [40] for Measuring Gas Permeability of Concrete under Compression

2.4.1.2. Gas permeability

While relatively easy to assess, conducting water permeability tests poses certain difficulties. They take over 24 hours in order to achieve a steady state flow. Further, due to the interaction of water with the bulk cement paste and the consequent blockade of pores due to siltation [54], there exists an element of error in relating the test data with the actual permeability. Therefore, gas permeability tests have been developed wherein an inert gas (usually Nitrogen), chosen specifically to have no interaction with concrete, is used [40-42, 55, 56].

Hearn and Lok [40] built a permeability apparatus that measured nitrogen (N_2) permeability of mortar simultaneously during a uniaxial compression test. The two platens that they designed for their apparatus could apply compressive stress and at the same time, control the gas permeability (Figure 2.6).

Figure 2.7 shows a similar set-up developed by Sugiyama et al. [41]. They investigated the permeability of nitrogen gas in hollow cylindrical specimens made of structural lightweight concrete under uniaxial compression.

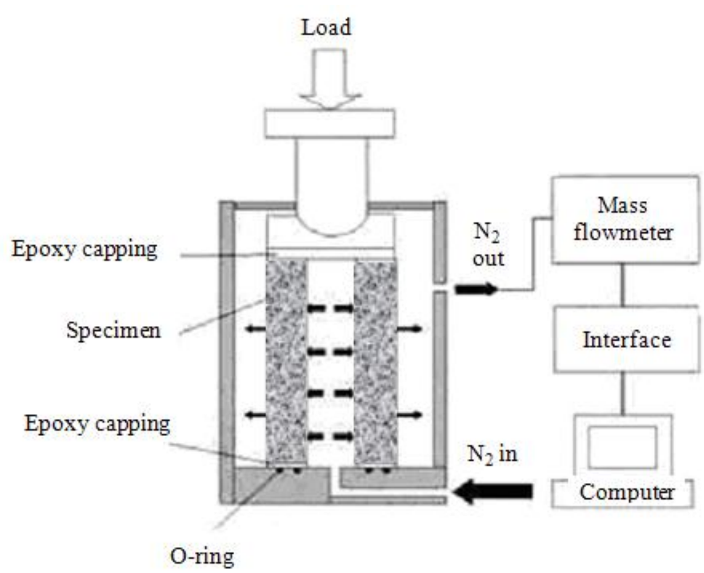

Figure 2.7. Schematic View of Apparatus Developed by Sugiyama et al. [41]

Picandet et al. [42] investigated the effect of uniaxial compression on the axial permeability of nitrogen, using a Cembureau Constant Head Permeameter

(Figure 2.8). Permeability was measured after unloading the specimen. They used the Hagen–Poiseuille relationship (Equation 2.8) for laminar flow of a compressible viscous fluid through a porous body under steady-state conditions to calculate the intrinsic permeability *K′* (m^2). They then applied the Klinkerberg equation, (Equation 2.10), to calculate the intrinsic coefficient of permeability, K_l, (expressed in m^2) relative to the viscous flow.

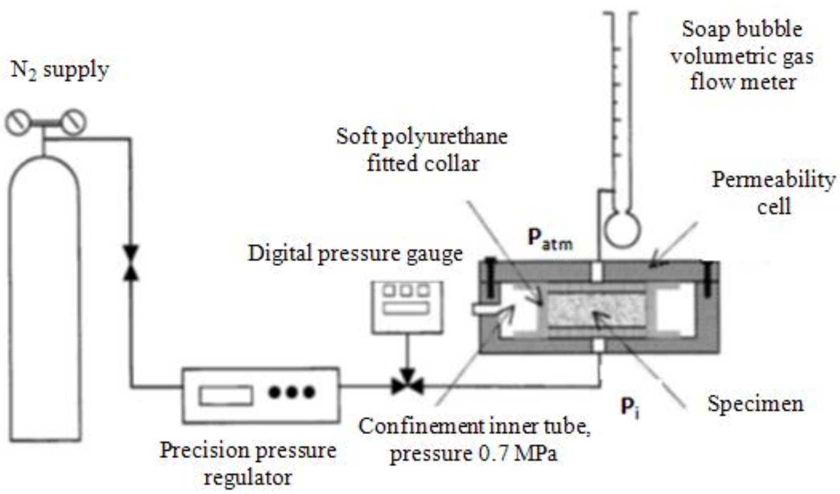

Figure 2.8. Experimental Setup used by Picandet et al. [42] Based on Cembureau Constant Head Permeameter

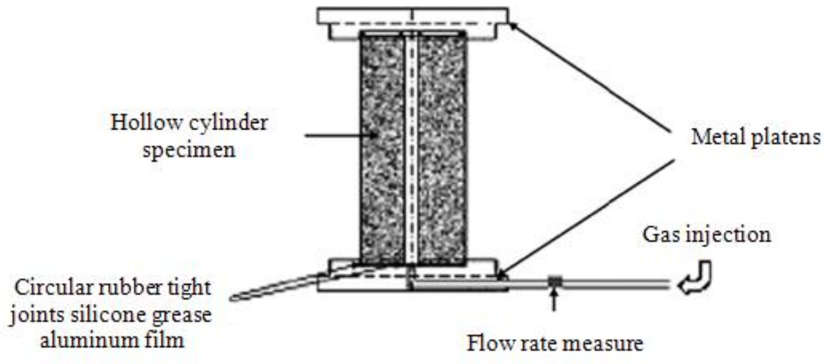

Figure 2.9. Schematic View of Permeability Cell Developed by Choinska et al. [5]

In a recent study by Choinska et al. [5], permeability tests were performed on hollow cylindrical specimens, taken after having been tested in compression (Figure 2.9). Nitrogen gas was used and the apparatus was so designed as to ensure that a radial gas flow was achieved. Upon gas flow stabilization, Darcy's law was applied to calculate the intrinsic permeability, once isothermal conditions prevailed.

2.4.2. Effect of Load Levels and Loading History

The type of applied stress (compression, tension, flexure), the rate of loading and the load level (as a fraction of ultimate load), all influence the crack generation and pattern, which in turn affect the transport properties of concrete [22, 33, 47, 57]. For example, in compression, at low levels of loading (up to 30% of ultimate strength), cracks were restricted to the aggregate-paste interface [11], and this was reflected in very little increase in permeability, if any [6, 22]. As the load approached the peak value, the cracks were seen to extend into the mortar and hence there was a rapid increase in the permeability of concrete [5].

2.4.2.1. Effect of Load Levels

Kermani [33] investigated the permeability of stressed concrete after unloading the specimens. He first loaded the specimens to a desired level (at 10% increments between 0 to 70% of ultimate stress) for 5 minutes and then unloaded and measured the water permeability of the specimen. He found that the water permeability was related to the applied stress and identified a threshold stress level of approximately 40% of ultimate. In other words, at stress levels below the threshold value, there was a small change in permeability, whereas at higher stress levels beyond this threshold, the permeability increased rapidly. Incidentally, in their studies on concrete in compression, Banthia and Bhargava [22, 43] found this threshold to occur for plain concrete at a level of about 30% of peak stress.

Studies show that with gas permeability, this threshold value of applied compressive stress is much higher. Using the apparatus shown in Figure 9, Choinska et al. [5] observed that as seen with water, there is at first a slight drop (up to 20%) in the permeability up to 50-60% of the peak stress. Upon further loading, the permeability increased marginally up to 80% of the peak stress. Only beyond 80% of ultimate stress, did they notice a significant increase in gas permeability (Figure 2.10). Their results are similar to the findings of Sugiyama et al. [41].

A constant permeability (or even a slight drop) initially under compression is due to the effect of consolidation or closing of voids and microcracks in concrete. This is confirmed by Choinska et al. [5] who observed that up to about a threshold stress of 80% of peak stress, permeability when measured after removing the load is more than the permeability during loading. Understandably, beyond 80% of ultimate, there was a rapid increase in the permeability due to the coalescence of cracks prior to failure. They also observed that while there is a stress dependency on the permeability if measured under load, the permeability of the specimens remained constant when measured after the removal of load at each stress level until about 70-80% of peak stress. Again, beyond this threshold value, regardless of whether it was measured during loading or immediately after unloading, the permeability registered an increase.

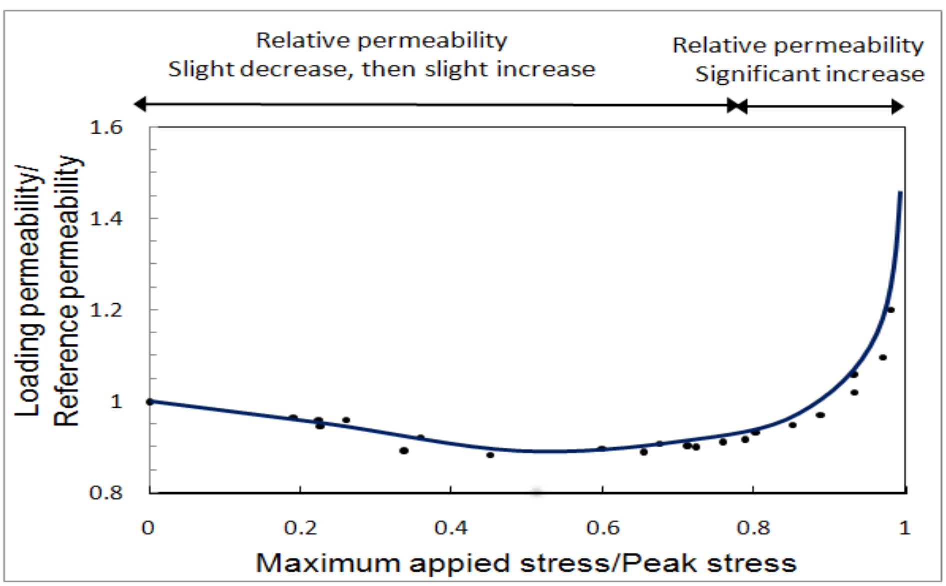

Figure 2.10. Variation of Intrinsic Permeability Values with Loading for Tests at 20°c Temperature [5]

Picandet et al. [42] observed that while a stress level of about 90% of ultimate stress increases the permeability of concrete to 10 times that in a non-stressed specimen, the threshold value for compressive strain is also at about 80% of yield strain. This value is in correlation with the formation of uniformly distributed and connected microcracks through the concrete after unloading [40, 41, 54, 58] (see Figure 2.11).

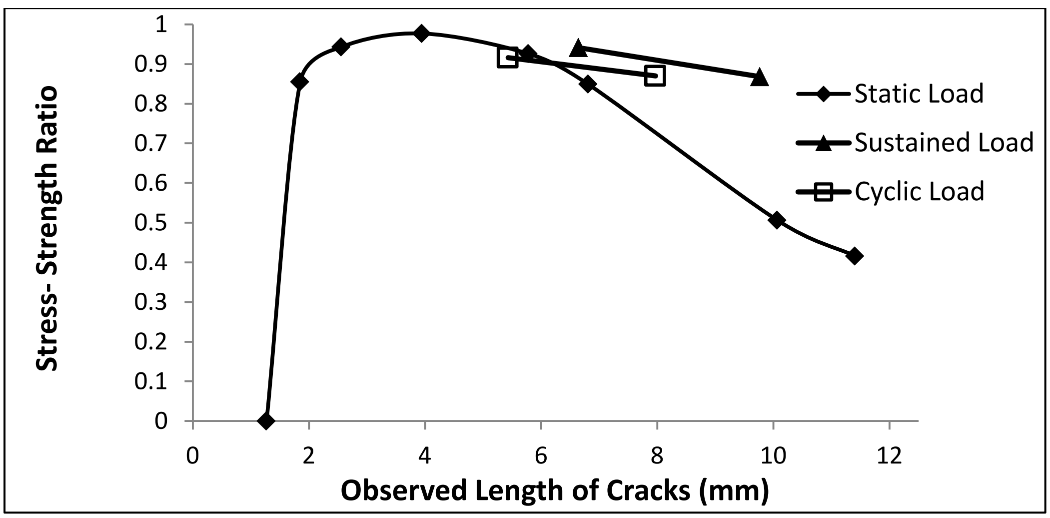

Figure 2.11. Crack Propagation in Concrete [58]

Be it water or nitrogen gas, it is clear that as concrete is compressed, the pre-existing network of conduits namely, the intrinsic pores and micro-cracks, are constricted initially. Hence, permeability dips until a level of load corresponding to the coalescence of microcracks at which point it begins to rise. However, it appears that in compressively loaded specimens, the permeability of water is in fact more sensitive than that of nitrogen gas to the development and coalescence of cracks. It is not clear from the published literature as to why this is so. Interestingly, Hearn [59] obtained a significantly higher threshold than others – at 80 percent of peak stress – for the permeability of water. At the same time, Hearn and Lok [40] noted that the permeability of nitrogen gas registered a lower threshold value of about 70% peak stress.

In their study on the permeability of chlorides, Samaha and Hover [6] did not observe any significant change even at 75 percent of the ultimate stress, and only marginal increase (15 to 20 percent) above 75 percent of the ultimate strength. Their findings are very similar to the results of Ludirdja et al. [45] who too observed a very modest rise in the permeability of water in spite of considerable crack development. Clearly, more research is required to understand the relationship between load-induced cracking and permeability in concrete.

2.4.2.2. Effect of Loading History

Banthia et al. [47] observed that in addition to being affected by the level of current load, permeability is equally influenced by the loading history. At a stress of 30% of ultimate, they noticed a drop in the permeability of a previously unloaded specimen. On the other hand, at this same level of stress, a specimen that had been previously loaded (in their study, up to 40% of ultimate stress), registered a significant increase in the water permeability. Cyclic loading is seen to lower the threshold value of stress. Thus, permeability increases rapidly even at lower levels of stress if the specimen has been previous loaded. Saito and

Ishimori [57] investigated the chloride permeability of concrete under monotonic and cyclic loading whereby the permeability was measured after unloading at each load level as per AASHTO T277 [50]. The specimens were loaded monotonically in compression at 0%, 30%, 50%, 70%, 90% and 100% of the ultimate stress. On the other hand, the cyclic loading involved 300 cycles per minute reaching maximum stress levels of 50%, 60%, 70% and 80% of the ultimate stress. Their study shows that under monotonic compression, even at ultimate stress, the permeability is only marginally different from that in a specimen that is not under load. On the other hand, in cyclically loaded specimens, there was a threshold stress at 50% of ultimate so that beyond this level, there was a significant increase in the chloride permeability of concrete specimens.

2.4.2.3. Effect of Crack Dimension

Cracks, especially interconnected cracks, provide a path through concrete for the migration of water and chlorides. If the cracks are not interconnected they have little or no effect on the transport properties of concrete. Breysse and Gerard [60] classified the role of cracks in fluid transport within concrete based on crack pattern as follows: 1) transport through a single crack or very few cracks 2) transport through a set of cracks with unknown individual parameters. The crack geometry was found to have an important role in the permeability of concrete with the crack width and its tortuosity being the most significant parameters [60, 61].

However, it is expected that due to self sealing of uncracked concrete and the autogenous healing of cracks, the water flow rate through both uncracked and cracked concrete decreases with time.

Permeability in concrete is proportional to the cube of the crack width for cracks greater than 1 mm [62] so, a specimen with several smaller cracks will be less permeable than that with a single large crack [37, 38]. Also, a specimen with distributed cracks will exhibit a much lower permeability than a specimen with a single localized crack having the same total crack area [44].

Clear [63] has discussed the mass transfer properties through a single crack and the effect of distribution of a single crack into a number of smaller cracks. If, instead of one large crack of width *W*, *n* smaller cracks of width *w* form, the proportionality of flow rates would be:

$$\frac{Q_w}{Q_W} = \frac{1}{n^2} \qquad 2.14$$

In this case, it is assumed that cracking is uniformly distributed throughout the matrix so that cumulative damage progressively modifies the characteristics of concrete.

Wang et al. [34] used a feedback controlled splitting test method to generate width controlled cracks in concrete specimens to study the water permeability of cracked concrete with different crack widths. They loaded the specimens to have several crack opening displacement (COD) from 25 μm to 550 μm and then unloaded the specimens. As shown in Figure 2.12, they found similar trends for permeability whether it was measured under load, or after unloading. Their study indicated that at peak stress, the COD was less than 20 microns and further, about 80% of this was recovered after unloading which means it had very little effect on the permeability of concrete. Similar findings were also reported by Aldea et al [35, 48]. However, it is apparent that for the same COD, concrete is less permeable when under load.

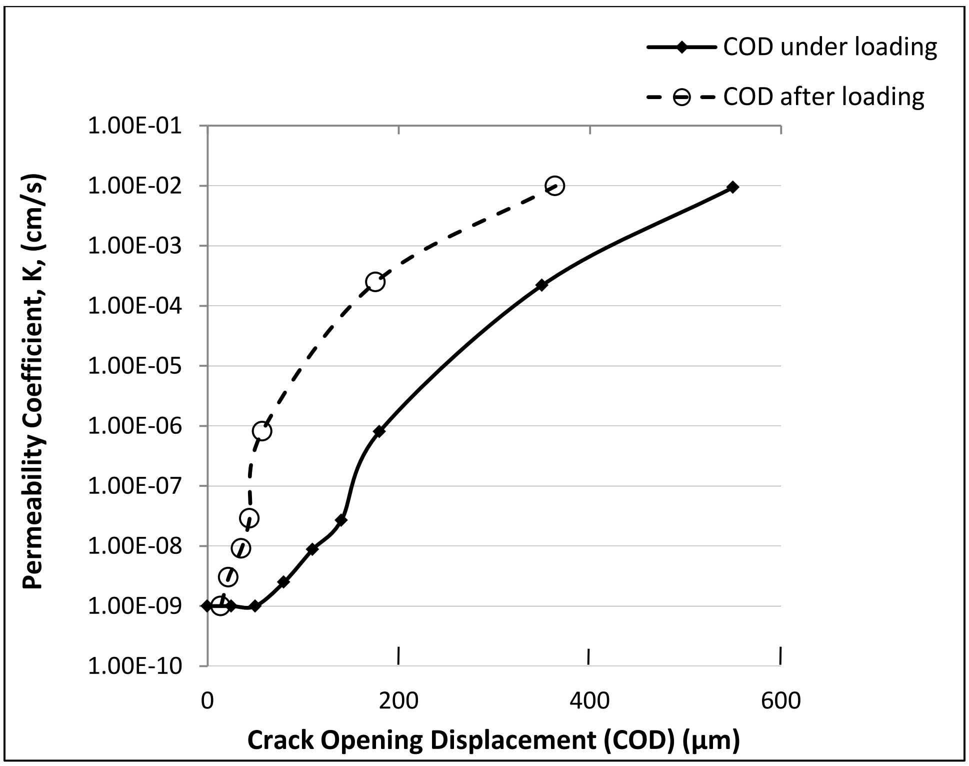

Figure 2.12. Relation between Water Permeability and Crack Width [34]

As with the applied load, it appears that there is a threshold for crack width as well. Wang et al. [34] observed an increase in the permeability of water with an increase in the crack width such that for COD of less than 50 μm, there was little change in concrete permeability but for a COD between 50-200 μm, the permeability increased rapidly. For CODs greater than 200 microns, they observed a continued increase in the rate of water permeability although this was far less rapid than earlier. Similarly, Aldea et al. [35], found a threshold crack width of 100 μm for concrete specimens under load. Incidentally, the threshold value of crack width was twice as much (200 μm) for chloride permeability (measured according to ASTM C1202 [64]) as reported by Aldea et al.[48]. Once again, it appears that the permeability of chlorides is less sensitive to applied stress than that of water. More studies are needed to confirm this and understand the underlying mechanisms.

The cumulative crack length appears to have no effect on the permeability of fluids in concrete. Samaha et al. [6] used Neutron Radiography [65] to analyze cumulative crack length caused by externally applied load and did not observe any variation in permeability. They also did not notice any influence of the electrical charge (according to ASTM C1202); neither on chloride permeability nor on the degree of microcracking.

Aldea et al. [36, 51] measured the flow of water in concrete samples using wedge splitting tensile load. The difference between the splitting tension method [34, 35, 48] and the wedge-splitting tension method [36, 51] is that in the splitting tension method, the width of the crack at mid-span was the only measured crack parameter and the water permeability test was carried out on unloaded specimens. On the other hand, in the wedge-splitting tension method, both the COD and the crack length were monitored throughout the test and the water permeability test was carried out on loaded samples. They concluded that water permeability coefficients increase with an increase in the crack width (Figure 2.13) and further, that this trend was independent of the technique used to induce the cracks. Further, while there was no direct relation between the crack length and water flow, there was a decrease in the permeability coefficient with time. This is believed to be due to the ongoing hydration and consequent healing of cracks and is especially true for crack widths less than 200 microns. However, for wider cracks no such drop in permeability was noticed. According to Aldea et al. [36] a single crack parameter namely, the crack width is sufficient to characterize the relationship between cracking and water flow in concrete.

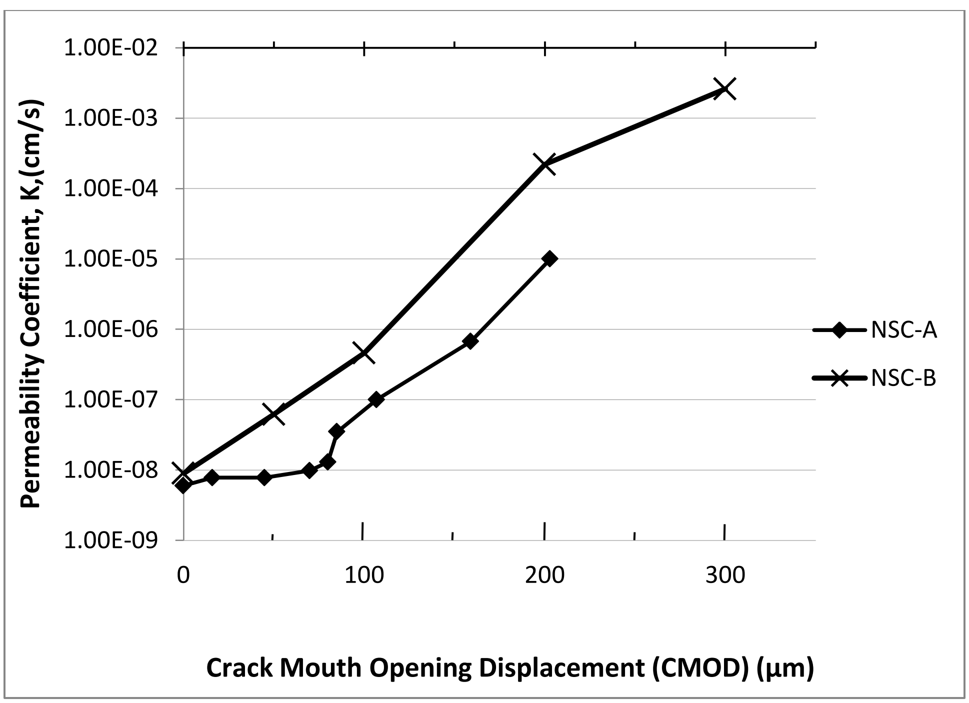

Figure 2.13. Cracking Effect on Permeability of Concrete (NSC-A: Cracked Normal Strength Concrete Tested under Load, NSC-B: Cracked Normal Strength Concrete Tested after Unloading) (From [36])

Recognizing that in cracked concrete, the flow does not occur uniformly through the concrete but in fact through the distributed cracks, Lawler et al. [44] used the flow rate (ml/s) instead of the permeability coefficient to analyze their experimental data and they found nearly the same threshold crack width of 100 μm for tensile load as that obtained by Aldea et al. [35] for compression. Locoge et al. [66] also found that the diffusion coefficient is not influenced by the presence of microcracks. As stated before, the cracking in the mortar is by far more influential in increasing the rate of mass transport in concrete than cracking at the aggregate-paste interface [6]. Microcracking within the mortar is chiefly responsible for the increase in total porosity under load. This is more manifest beyond the threshold stress level.

2.4.3. Effect of Concrete Mix Design

Kermani [33] observed that at low stress levels, regular concrete (with no mineral admixture) had better resistance to the permeation of water than a mix containing fly ash. In all likelihood, this is due to the unhydrated cement particles that tend to block the pores in transit with the pore fluid. However, Samaha et al. [6] observed that the mix containing fly ash recorded a drop in its electrical activity (as measured by the current passing through it in the Rapid Chloride Permeability Test [64]) till 75% of the ultimate stress after which it increased dramatically. They observed that while the cumulative crack volume increased with an increase in the compressive stress, the transport properties were not affected until a continuous network of cracks was formed.

As expected, the permeability of air entrained concrete is known to be higher than that of normal concrete (non air-entrained) at all stress levels [6]. However, the relative rise in permeability under stress appears to be less in the case of air entrained concrete. For instance, the permeability increased more than 100 times between stress levels of 40% to 70% of ultimate strength for a mix with 5% air content. A regular concrete mix (non air entrained) registered a 1000 fold increase for the same stress interval.

Permeability is affected by the matrix strength [35, 48]. It is thought that normal strength concrete (NSC), being significantly non-linear results in a slower crack recovery than for high strength concrete (HSC). Thus, regardless of whether the concrete is cracked or otherwise, HSC was less permeable than NSC. However, for crack widths less than 200 microns, the difference in the permeability coefficient between these two types of concrete was low. Beyond this threshold crack width, the permeability of NSC was seen to increase more rapidly than that of HSC. Sugiyama et al. [41] studied the effect of concrete density on the permeability response of nitrogen. They observed that structural lightweight aggregate concrete (LWC), weighing 25% less than normal weight concrete, had a 10% higher threshold value for compressive stress. An early study by Tsukamoto [49] showed that for a given crack width, the presence of larger mean aggregate size led to a drop in fluid permeability.

The adverse effect of the interfacial transition zone on the permeability of concrete is well known [11]. However, when the specimen is subject to stress, excluding coarse aggregates from the mix is actually detrimental and results in a two-three fold increase in the mass transport within concrete [6]. Once again this underscores the significance of microcracking within the bulk matrix as opposed to the development of interfacial cracks.

2.4.4. Effect of Fibers

Fiber reinforced concrete is expected to improve the durability of concrete under load, due primarily to its ability to control crack widths. However, the benefit to the control of permeability in concrete depends upon the choice of fibers, particularly on the fiber size. Tsukamoto [49] was one of the first to examine permeability in fiber reinforced concrete under stress. While he obtained a drop in the flow of water in the presence of fibers, he observed that the finer the fiber, the better the control on fluid flow in the stressed concrete. Recently, Banthia and Bhargava [22] examined the effect of stress on the permeability of fiber reinforced concrete containing a purified plantation softwood fiber at up to 0.5% fiber volume fraction. They observed that although for both plain and fiber reinforced concrete the threshold value of stress was about 30% of peak stress, for fiber reinforced concrete a rapid increase in the permeability occurred only beyond 50% of peak stress. Moreover, they observed that at a stress level of 50% of peak stress, the permeability of fiber reinforced concrete (regardless of fiber dosage) was lower than that for the unstressed state (Figure 2.14).

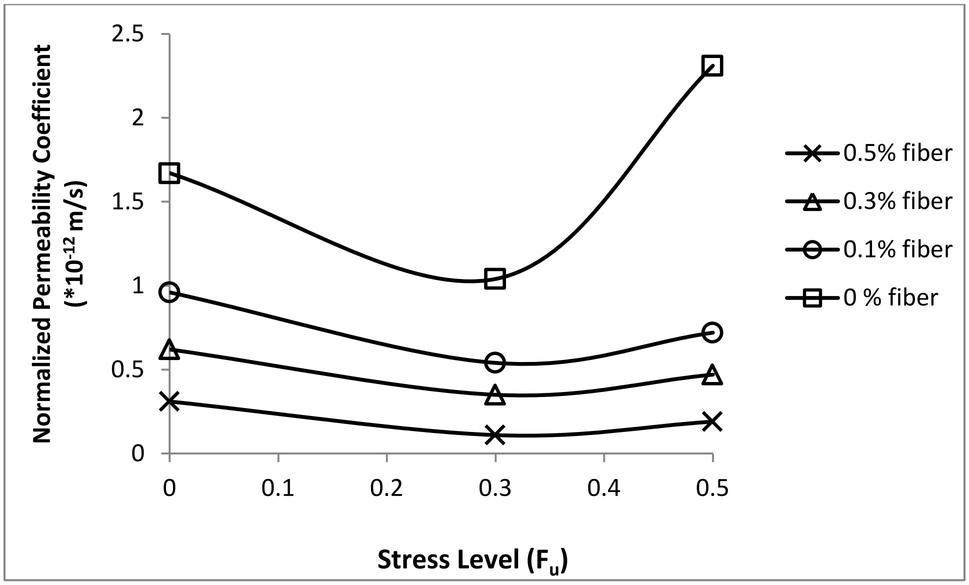

Figure 2.14. Influence of Stress on Relative Permeability of Plain and Fiber Reinforced Concrete (From [22])

Rapoport et al. [37, 38], investigated the influence of steel fibers at up to 1% volume fraction. They noted that although fiber reinforced concrete had a more unrecoverable deformation than plain concrete; the presence of fibers reduced the permeability of cracked concrete. Contrary to the trend seen in Figure 2.14, an increase in the fiber content led to an increase in permeability. However, this increase in the permeability was more obvious for crack widths greater than 100 microns.

Lawler et al. [44] compared three mixes; one with a steel macrofiber, another with microfibers (of PVA or steel) and a third mix with a blend of these fibers. While the mixes containing the blend of steel macrofibers and PVA microfibers showed the best behavior, the mixes containing only macrofibers had very little effect on the permeability of concrete. In all cases the microfibers and the blended fibers reduced the permeability efficiently. Clearly, since permeability is affected by crack widths, bridging the microcracks before they coalesce is far more beneficial to restricting the permeability.

As presented in this chapter, under the action of applied stress, there is a decrease in the permeability up to a certain threshold level followed by a dramatic increase beyond this threshold stress. Since permeability depends largely on the interconnected pore network within the hydrated cement paste, it is important to examine and quantify the change of pore connectivity of cement-based materials during the course of stress application. The application of x-ray tomography in studying the microstructure of cement-based materials (in general) as well as finding the pore connectivity and its relationship to permeability (which is one of the focal points of this study) will be discussed in Chapters 4, 5, 8 and 9.

3. Ultrasonic Pulse Velocity (UPV) in Cracked Concrete

3.1. Introduction

As described in Chapter 2, measuring permeability involves a time-consuming test, with attendant concerns about system equilibrium and load control. Non Destructive Testing (NDT) of concrete makes it possible to obtain many test results from a single specimen and thus gives the opportunity to follow the changes in the properties of the specimen over time and under external influences. The use of ultrasonic waves to evaluate cement-based composites presents a non-destructive and readily repeatable test, and it dates back to the 1940s [67].

In this chapter the concepts of UPV in unstressed concrete are presented and then the effect of stress on UPV is reviewed.

3.2. UPV in Unstressed Concrete

Wave velocity measurements are based on measurement of the propagating pulse velocity, which is the time travel (first arrival) of the wave through a concrete member between two points with known distance. There are three main types of waves depending on the ways of producing of the wave:

3.2.1. Longitudinal Waves

Longitudinal or compression waves are the waves that have the same direction of oscillations parallel to their travel direction. In other words, the oscillation of the particles is in the same or opposite direction of the wave motion (Figure 3.1).

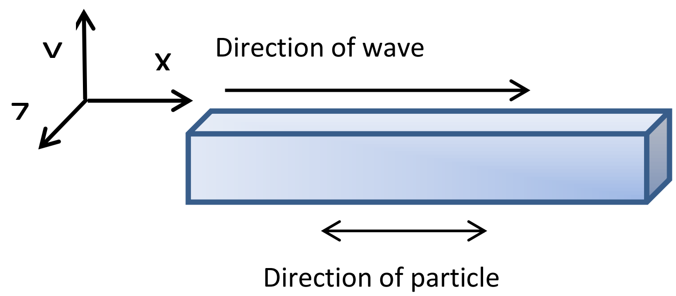

Figure 3.1. Schematic Illustration of Longitudinal Wave

The longitudinal wave velocity in a homogenous, isotropic and elastic medium is calculated by [67]:

$$V_p = \sqrt{\frac{E_d\,(1-\nu)}{\rho(1+\nu)(1-2\nu)}} \qquad 3.1$$

Where:

V_p : longitudinal wave velocity

E_d: Modulus of Elasticity

ν: Poisson’s ratio

ρ: Density

3.2.2. Shear Waves (S-Waves)

Shear waves are the type of waves where the particle movement occurs in a direction perpendicular to the wave direction (Figure 3.2). In other words, if a transverse wave is moving in the x-direction, its oscillations are in the up and down directions in y-z plane.

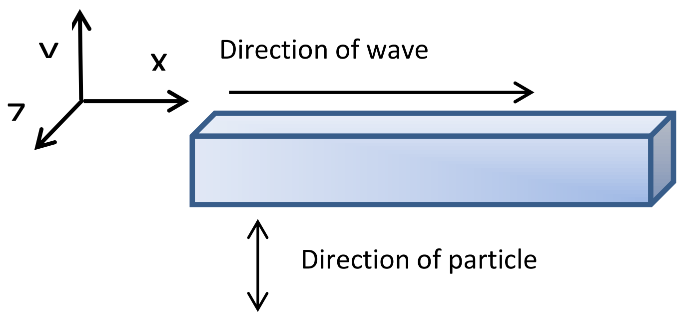

Figure 3.2. Schematic Illustration of Shear Wave

Similar to longitudinal waves, the velocity of a shear wave in a homogenous, isotropic and elastic medium is calculated by [67]:

$$V_s = \sqrt{\frac{E_d}{2\rho(1+\nu)}} \qquad 3.2$$

Where, V_s is the shear wave velocity and other parameters are the same as described in Equation 3.1.

3.2.3. Surface Waves

The longitudinal and shear waves are propagated through the body of material in all directions. There is another type of wave motion which travels along the surface of material and the amplitude typically decays exponentially with depth into substrate (Figure 3.3). This type of wave is called the surface wave.

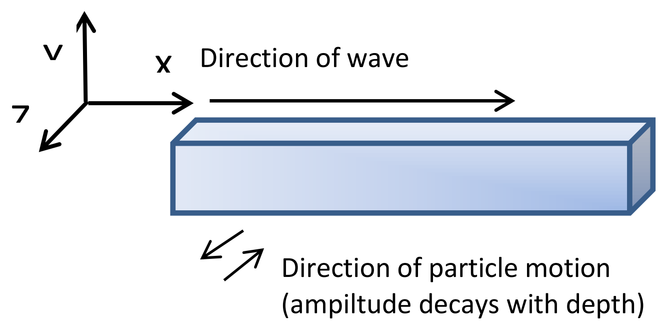

Figure 3.3. Schematic Illustration of Surface Wave

Similar to longitudinal and shear waves, the velocity of a surface wave in a homogenous, isotropic and elastic medium is calculated by [67]:

$$V_p = \frac{0.87 + 1.12\nu}{1 + \nu} \sqrt{\frac{E_d\,(1 - \nu)}{\rho(1 + \nu)(1 - 2\nu)}} \qquad 3.3$$

Since in the permeability measurements, the flow of water is through the bulk of concrete, we will review and examine the longitudinal type of wave for the rest of this chapter.

UPV method is based on the velocity of longitudinal waves which employs the principle of measuring the time of travel of an ultrasonic pulse through a medium. There is an ASTM standard (C597-09) [68] that describes the application of UPV method in concrete. So far, ultrasonic methods have been used for estimating concrete strength [69-72] and detecting internal defects, cracks and voids [73-77]. These studies have shown that ultrasonic pulse velocity in concrete is affected by porosity, extent of connected pores and cracks, as well as crack size, all of which also influence the concrete permeability.

As shown in Equation 3.1, UPV is mainly proportional to the modulus of elasticity. Since the compressive strength and elastic modulus are related, it is expected that UPV can also be correlated to compressive strength. It has been found that this correlation is not unique but rather depends on the mix proportions and aggregate types and has the linear or exponential form, where the higher the compressive strength, the higher the measured UPV [69-72]. However, UPV may be used to estimate compressive strength as long as a calibration curve exists for each assessed material.

Relating permeability with ultrasonic pulse velocity offers tremendous potential, especially in condition assessment of existing structures wherein a rapid and non-destructive test method is needed for durability evaluation of concrete. Few reports exist that correlate fluid permeability with pulse velocity in cement-based materials [78, 79]. Further, none of them considers the effect of sustained compressive stress. Lafhaj et al. [79] used available porosity–pulse velocity and porosity–permeability relationships, based on Yaman et al.[74, 75], to derive a linear expression between gas permeability and ultrasonic pulse velocity in cement-based mortars under no stress:

$$K = \frac{d^2}{32\, b} \frac{\Delta V}{V_0} \qquad 3.4$$

Where:

K= gas permeability;

d= pore diameter;

b= a parameter related to Poisson's ratio at zero porosity;

V_0= ultrasonic pulse velocity at zero porosity; and

ΔV= change in ultrasonic pulse velocity.

For the range of porosity in their study (8% to 13%) [79], the experimental findings were seen to fit well in a linear model. On the other hand, Shkolnik et al. [78] found a non-linear relationship between water permeability and ultrasonic pulse velocity in concrete under no stress, and although they plot a best-fit curve, the nature of this relationship is not elaborated upon.

3.3. UPV in Stressed Concrete

Concrete is a heterogeneous anisotropic material with non-linear behavior. The application of stress will induce more anisotropy in concrete. According to Equation 3.1, since the stress-strain curve of concrete is not linear and its modulus of elasticity depends on the stress level at which the concrete is subjected, UPV is also stress dependent. It can also be seen that the UPV is a function of elastic stiffness and not strength. Since the higher stress levels in concrete will reduce the apparent modulus of elasticity, it is expected that the presence of stress would also reduce the UPV. On the other hand, the effect of cracking on UPV is directional in nature [67], i.e. cracks parallel to the pulse direction have little effect while cracks perpendicular to the direction would have large effects. Popovics [80] measured the UPV under simultaneous effect of stress and found that UPV increases slightly in low stress levels and then with further stress, remains constant and only after 70% of the ultimate strength does it decrease rapidly. He concluded that since micro-cracks developing in concrete during the loading are too narrow to effect the pulse velocity, stress conditions in concrete structures should not be taken into account when UPV is used for the evaluation of concrete. On the other hand, other researchers found that the UPV is sensitive to the level of stress in concrete [81-83]. They found that at low levels of stress, as the stress is increased the measured velocities increase slightly. This behavior was attributed to the closure of micro-cracks with increasing stress (see Figure 3.4). Then, after a certain level of loading, the UPV starts to decrease due to formation of large cracks and reduction in stiffness. Since the sound pulse travels far faster through solid material than it can through air, such cracking simply creates a ‘void’ that the pulse must travel around and hence increases the time required for the pulse to reach the receiving transducer. The level at which the UPV starts to decrease has been reported between 25 to 80 percent of compressive strength [73, 81].

The formation, growth and coalescence of microcracks at different stress levels will introduce anisotropy in UPV measurements. It can be concluded that if the velocity-stress relationship is established, by measuring the UPV, the state of stress in structure can be calculated.

These studies have shown that ultrasonic pulse velocity in concrete is affected by porosity, extent of connected pores and cracks as well as cracks size, the parameters which also influence the concrete permeability.

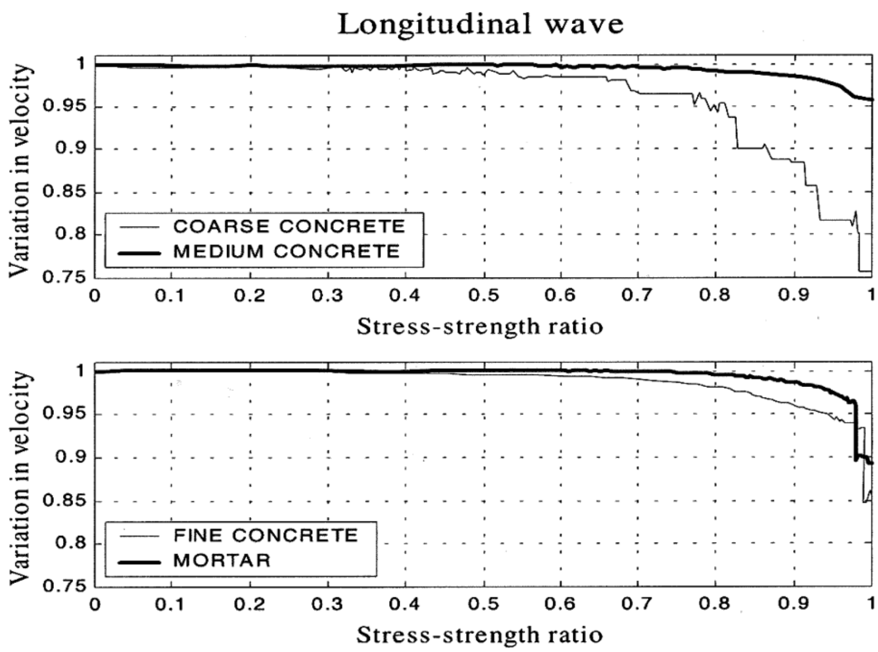

(a) Coarse Concrete: MSA=12.5 mm, Medium Concrete: MSA= 9.5 mm, Fine Concrete: MSA= 4.75 mm, MSA= Maximum Size Aggregate

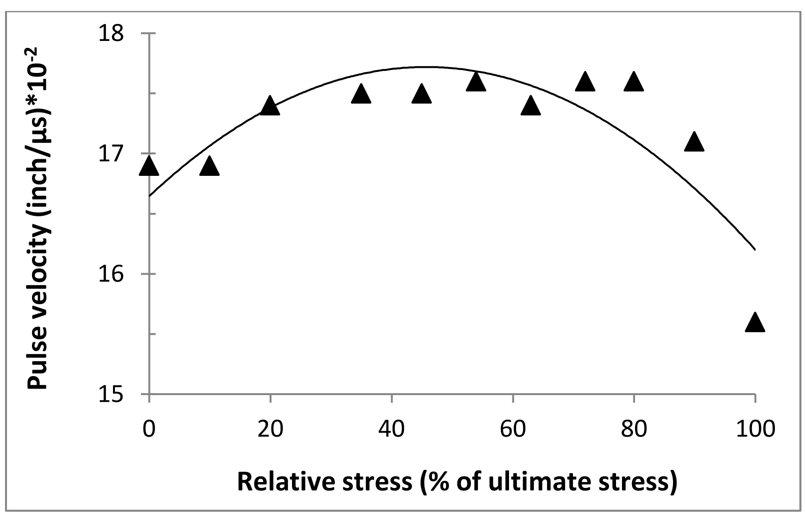

(b) Concrete: The Trend Line is also Shown in Original Reference.

Figure 3.4. Change in UPV by Increase in the Load: (a) Nogueira et al. [81], (b) Popovics et al. [80]

4. Application of X-Ray Tomography (XRT scan) in Studying the Concrete Microstructure

4.1. Introduction

As indicated in Chapter 2, permeability depends largely on the interconnected pore network within the hydrated cement paste and it is important to examine and quantify the change of pore connectivity of cement-based materials during the course of stress application. In this study, the x-ray tomography technique has been employed to determine its suitability for studying the microstructure of cement-based materials as well as finding the pore connectivity and its relationship to permeability.

X-ray tomography (XRT) was first introduced in 1971 as a powerful method for medical x-ray diagnosis which brought the 1979 Noble prize in Medicine for its inventors. It is a technique by which the internal structure of material is determined from maps of its x-ray absorptivity [84]. The principle is based on the 3D computed reconstruction of a sample from 2D projections acquired at different angles around its axis of rotation. An XRT image is also called a Computed Tomography (CT) Scan or Computed Axial Tomography (CAT) Scan. Regardless of the name used, it refers to the computation of tomography from x-ray images. The current indexing of the National Library of Medicine- Medical Subject

Headings (MeSH), explicitly include the “X-ray” in the title of “computed axial tomography” [85].

The mechanism of XRT has been described in detail by Flannery et al. [84]. Tomography is an imaging-by-section technique through the use of any kind of penetrating wave. Briefly, x-ray tomography is an imaging procedure that employs computer processed x-rays to produce tomography images. Image processing methods are used to generate three-dimensional image of inside the object from a large series of two-dimensional x-ray images taken around a single axis of rotation. The x-rays illuminate a shapeless specimen and radiographic images are obtained at a large number of discrete view angles during the rotation of a sample about its axis. The rotation axis is kept perpendicular to the X-ray beam. The resulting image data are saved such that the projections for every succeeding angle are assembled together. The collected data is reconstructed to create a 2D tomography slice. Since the synchrotron beam is highly collimated, a fast direct Fourier inversion algorithm is employed to construct the slices. Finally, 3D objects are constructed from multiple 2D images by stacking the various slices. A schematic illustration of XRT set-up is shown in Figure 4.1.

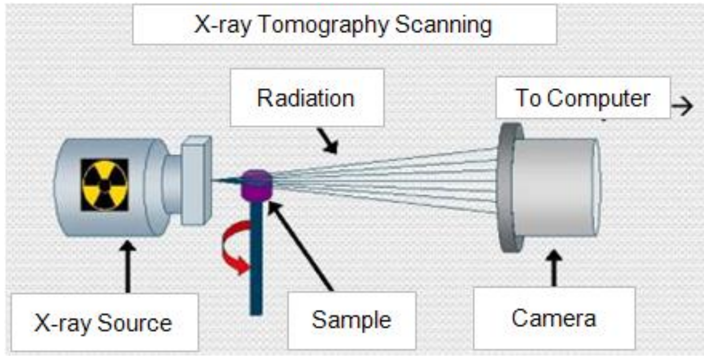

Figure 4.1. Schematic Illustration of X-ray Tomography Scanning

Recent advancements in this method present a non-destructive technique for microstructure characterization and study of engineering materials such as cement-based systems [86-89]. It has been used to capture the 3D images to characterize the internal structure of cement-based materials. In this method the sample remains sound and can be used for further tests.

The primary advantage of XRT compared to other image acquisition techniques such as Scanning Electron Microscopy (SEM) and optical microscopy is that there is no special sample preparation requirement. Moreover, in XRT one can capture 3D images from the whole specimen while other methods can only provide two-dimensional information of the surface of a very small part or just one section at a time.

However, there are also some limitations with this technique including a limit to the specimen size due to the need for high-flux x-ray sources of narrow energy distribution, which increases with increased specimen size.

This chapter presents a brief review of the application of the x-ray tomography technique on cement-based materials in both stressed and unstressed specimens.

4.2. XRT in Unstressed Concrete

X-ray tomography, as applied in the absence of loading to concrete specimens, has been employed to study defects, voids and reinforcing steel location [86-90], sulfate attack [91-93] and cement hydration [94, 95].

Morgan et al. [88] reported one of the first tomography scans of concrete which provided qualitative estimation of concrete properties. Equally pioneering was the report by Martz et al. [87] who used computerized tomography to study reinforced concrete. The main objective of their work was to verify whether this method could detect the size and location of voids and reinforcing bars in concrete. Their results indicated that this method is able to resolve different phases in reinforced concrete. Quantitative data from solid phases and porosity as well as dependence between connectivity and resolution was investigated by Gallucci et al. [96].

Bentz et al. [97] in collaboration with the National Institute of Standards and Technology (NIST), Centre Scientifique et Technique du Batiment (CSTB) and European Synchrotron Radiation Facility (ESRF), obtained three dimensional representations of a material's microstructure with a voxel size of less than one micrometer. They shared all the collection of 3-D data sets obtained using the

ESRF in Grenoble, France in September 2000. Most of the images obtained are for hydrating Portland cement pastes, with a few data sets representing hydrating Plaster of Paris and a common building brick. All of these data sets are being made available on the Visible Cement Data Set website.

Helfen et al. [95] and Chotard et al. [94] applied the XRT method to characterize cement microstructure, its evolution during hydration and early hydration of calcium aluminate cement. They concluded that XRT can be beneficial to describe variations in x-ray absorption in relation to the progression of the hydration process in cement paste. Internal cracks and defects due to chemical attack such as by sulfates are also detected using micro-tomography [91-93].

Lu et al. [98] employed x-ray micro-tomography to link microstructure features to permeability in different concrete systems. They did not measure the permeability directly but measured the chloride penetration based on AASHTO T277 [50]. In this study, they could not find pore space that is connected from the top to the bottom of specimens in any of the resolutions studied (1μm and 4 μm). From tomography images, they defined and measured a parameter called disconnected pore distance (minimum distance between the pore network connected to the top of the sample and the pore network connected to the bottom of the sample). They found that this parameter increases by adding pozzolanic materials and found a correlation between chloride permeability and disconnected pore distance.

4.3. XRT in Stressed Concrete

There are very few studies that apply x-ray tomography for investigating internal damage in stressed concrete. In fact, most of this limited knowledge is from the works of Nagy [99] and by Landis and his associates [100-103] at the University of Maine, who used this technique to study the three-dimensional fracture energy of concrete. They took 3D images from 4 mm diameter by 4 mm height cylindrical mortars which where simultaneously under conditions of repeated loading and unloading (see Figure 4.2). Using stress-strain diagrams, image analysis techniques for calculating the number of connected components (this parameter will be described in Chapter 8), crack surface area of stressed specimens and basic fracture mechanics relationships for calculating strain energy, they found that the number of connected components increases by increasing the load cycle (Figure 4.3). Moreover, they showed that the XRT technique can be used to measure the work of fracture measurements where measured fracture energy is based on measured crack surface area. However, they did not study how the connected components and crack surface area would change under different static stress levels.

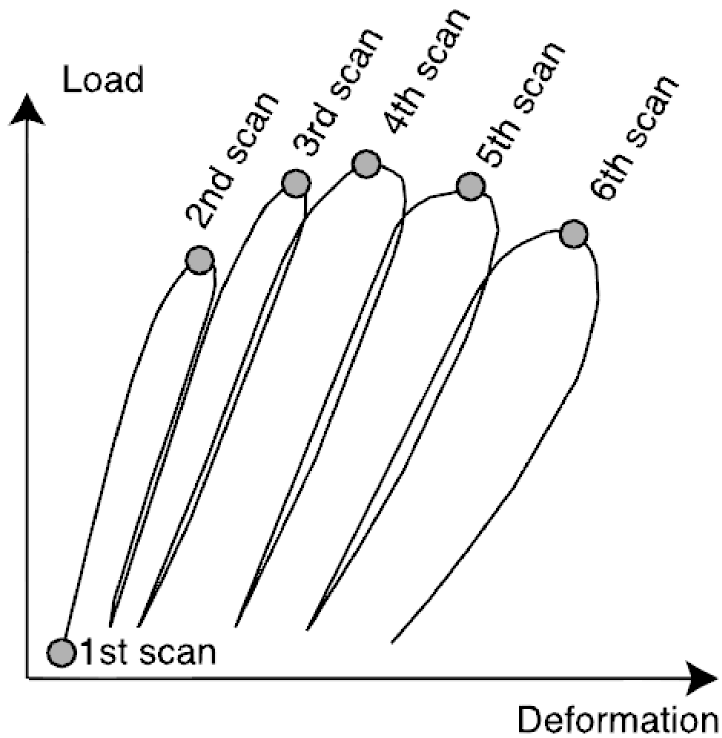

Figure 4.2. Illustration of load–deformation cycles and tomography scans in Landis studies [90, 100-104]

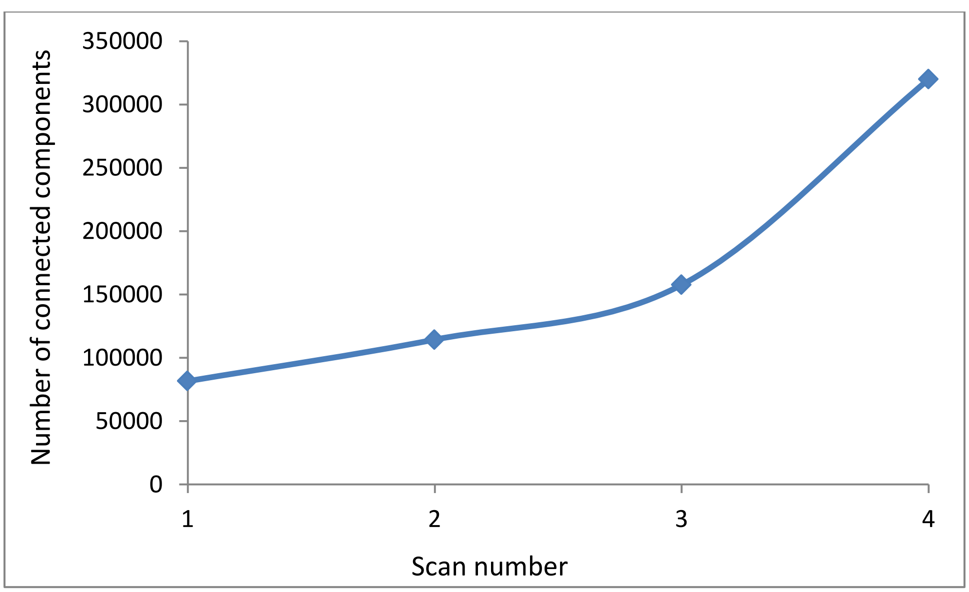

Figure 4.3. Change in number of connected components in different load cycles plotted from Table 1 of [102]

As presented in this chapter, the available literature provides valuable information on the use of the XRT technique in studying the microstructure of cement-based materials such as voids, hydration products and the number of connected components. However, efforts must be made to determine whether this technique is suitable for examining the pore connectivity of cement-based materials and its relationship to permeability. This is accomplished in the present study and is presented in Chapters 6, 8 and 9.

5. Experimental Program

This chapter presents the experimental program for this study. Mix designs, specimen preparation, mechanical property testing, permeability setup, UPV measurement method and the x-ray tomography technique (including image acquisition and analysis method used in the present study) are described in detail.

5.1. Materials and Mix Designs

This study looked at both concrete and mortar. Moreover, the role of fiber reinforcement has been examined by incorporating polypropylene fibers in the mix designs. Four mixes namely, plain Type S mortar, fiber-reinforced Type S mortar (with 0.25% volume fraction of polypropylene fiber), plain Portland cement concrete, and fiber-reinforced concrete (with 0.25% volume fraction of polypropylene fiber), were designed to achieve a 28-day compressive strength of 20 MPa for Type S mortar specimens and 40 MPa for concrete specimens, as summarized in Table 5.1.

The plain mortar mix consisted of a masonry mortar Type S premix (following ASTM C270 [105]), fine aggregates, and potable water. In addition, a High-Range Water-Reducing Admixture (HRWRA) was used to produce a workable Type S mortar mix with a flow of more than 110%, evaluated according to ASTM C1437 [106] (Figure 5.1), and a concrete mix with a slump of 100 mm to enable pouring into narrow regions, since the specimen wall thickness was only 25 mm. Cement Type GU and coarse aggregates, with a maximum size of 8 mm, were used in the concrete mixes. The water-reducing admixture (HRWRA) was suitably adjusted to accommodate for the loss in workability in the presence of the microfibers. Higher dosages of fibre made it difficult to disperse them uniformly in the mix and consolidate the mix in the narrow walls of permeability specimens and hence were not used for permeability studies. An additional fiber-reinforced concrete mix with 0.5% volume fraction of fiber was designed just for UPV measurement tests. The fibres were added to mix slowly and in low volumes to ensure homogeneous distribution. The fiber type used in this study is shown in Figure 5.2 and its physical properties are listed in Table 5.2. The chemical composition of Type S cement binder and Type GU Portland Cement as supplied by the manufacturers are shown in Table 5.3 and Table 5.4, respectively.

Material	**Proportion (kg/m^3)**				
	Plain Mortar (MS)	**Fiber Mortar (FMS)**	**Plain Concrete (PC0)**	**Fiber Concrete with 0.25% fiber (PC0.25)**	**Fiber Concrete with 0.0.5% fiber (PC0.5)**
Mortar Type S	400	400	-----------------	-----------------	-----------------
Portland Cement Type GU	---------------	---------------_	400	400	400
Coarse Aggregate	---------------	---------------	900	900	900
Sand	1200	1200	900	900	900
Water	200	200	200	200	200
HRWRA	4	6	4	6	6
Polypropylene Fiber	0	2.25	0	2.25	4.5

Table 5.1. Mix Composition and Proportions

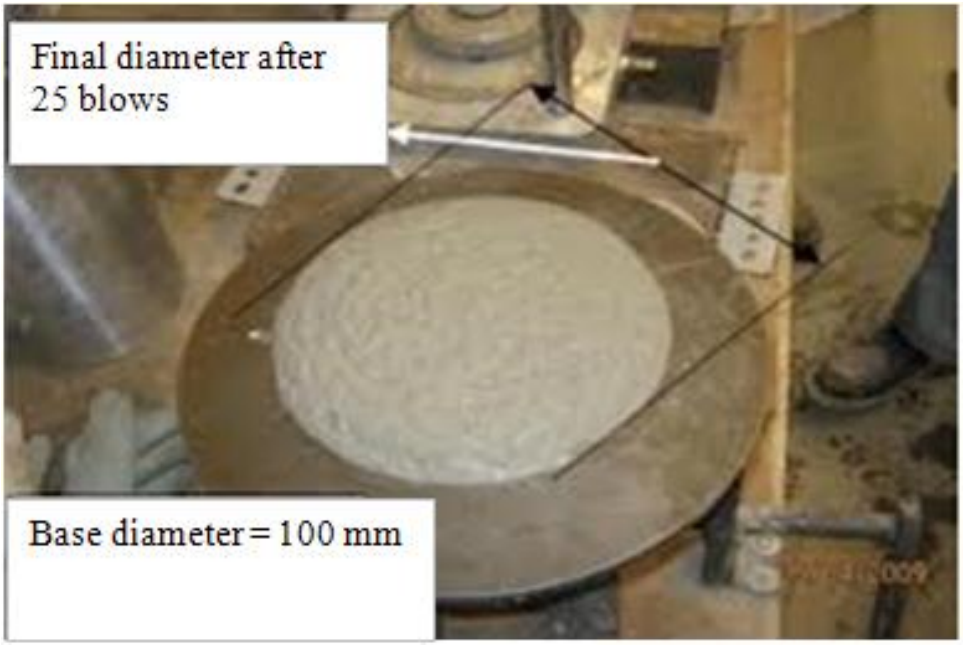

Figure 5.1. Measuring Flow According to ASTM C1437

Figure 5.2. Polypropylene Micro-fiber Used in This Study

Property	**Value**
Specific Gravity	0.91
Fiber Length (mm)	20
Tensile Strength (MPa)	450
Modulus of Elasticity (MPa)	3447
Fibers Diameter(mm)	0.02
Denier*	3

Table 5.2. Properties of the Fibers Used in This Study

*Linear mass density defined as: mass (in grams) per 9,000 m of fibre.

$CaCO_3$	**SiO_2**	**$Ca(OH)_2$**	**$CaSO_4$**	**MgO**	**CaO**	**Portland Cement**
20-25	<10	0-20	5-10	0-4	0-1	30-75

Table 5.3. Chemical Composition of Type S Cement (% of mass)

SiO_2	**Al_2O_3**	**Fe_2O_3**	**CaO**	**MgO**	**SO_3**	**Loss of Ignition (LOI)**
20.9	5.2	2.3	64.4	2.8	2.9	1

Table 5.4. Chemical Composition of Type GU Portland Cement

5.2. Specimen Preparation

5.2.1. Permeability Specimens

For measuring permeability, hollow cylindrical specimens were cast with a 100 mm outside diameter, 50 mm inside diameter, and a height of 200 mm. The hollow core was created using a solid shaft of Teflon inserted at the time of casting. The hollow cylinders were cured in their moulds for 3 days to ensure sufficient strength gain, so as to withstand the removal of the Teflon shaft. The Teflon shafts were removed using an extrusion jack.

a) Specimens after Demolding

b) Removal of the Teflon Shaft

c) Hollow Cylindrical Specimen

Figure 5.3. Different Stages of Specimens Preparation for the Permeability Measurement

The specimens were cured at 95±5% humidity and 23±2°C for a further 32 days. Thereafter, they were left in an ambient laboratory environment until they were tested at an age of 60 days. Figure 5.3 shows the hollow cylindrical specimens at various stages of their preparation.

5.2.2. UPV Specimens

For UPV measurements, four cubes with dimensions of 150 mm x 150 mm were cast to the same composition and proportions as the specimens evaluated for permeability. These cubes were cured for 35 days in 95±5% humidity at 23±2 °C. Prior to testing, two of the specimens were transferred to an oven at 110 °C and dried for 48 hours (oven-dried condition) to eliminate the effect of the specimens' moisture condition on UPV. The specimens were tested at 60 days of age.

5.2.3. Compressive Strength Specimens

For each mix design, three 100 mm*200 mm solid cylinders were cast for testing the strain-stress diagrams and compression tests. The cylinders were cured for 28 days in 95±5% humidity at 23±2 °C at which they were tested.

5.2.4. XRT Specimens

Because of limitations of the machine that was used for XRT studies, which only allows the scanning of objects with maximum dimensions of 20 mm, only small Type S plain and fiber reinforced mortar cubes (20 mm * 20 mm * 20 mm) were cast from the same mix that was used to prepare specimens for permeability and UPV measurement. These cubes were cured for 35 days in 95±5% humidity at 23±2 °C. Thereafter, they were left in an ambient laboratory environment until they were tested at an age of 60 days.

5.3. Test Set-up

5.3.1. Permeability Measurements

The permeability test setup used in this study was adapted from the apparatus developed by Biparva [39]. It was modified here to monitor the onset of the steady state condition in fluid flow. A schematic view of the permeability apparatus developed for the present study and a photo of the test setup at the graduate concrete research laboratory at the University of Alberta, are shown in Figure 5.4 and Figure 5.5, respectively. The apparatus originally consisted of five major sections: a cylindrical concrete specimen with a hollow core; a permeability cell that houses the concrete specimen; a pressurized water supply unit; an outflow measurement device (with an accuracy of 0.01g); and a Materials Testing System (MTS) with capacity of 1000 kN, which is capable of applying stress in compression under load control. In addition, this permeability cell was further instrumented with a computer and programmed to measure and record the mass of water flow in real time, thereby enabling detection of the onset of equilibrium in flow. The flask used to collect the water was completely sealed to significantly minimize the water evaporation during the test and thus negligible evaporation was assumed.

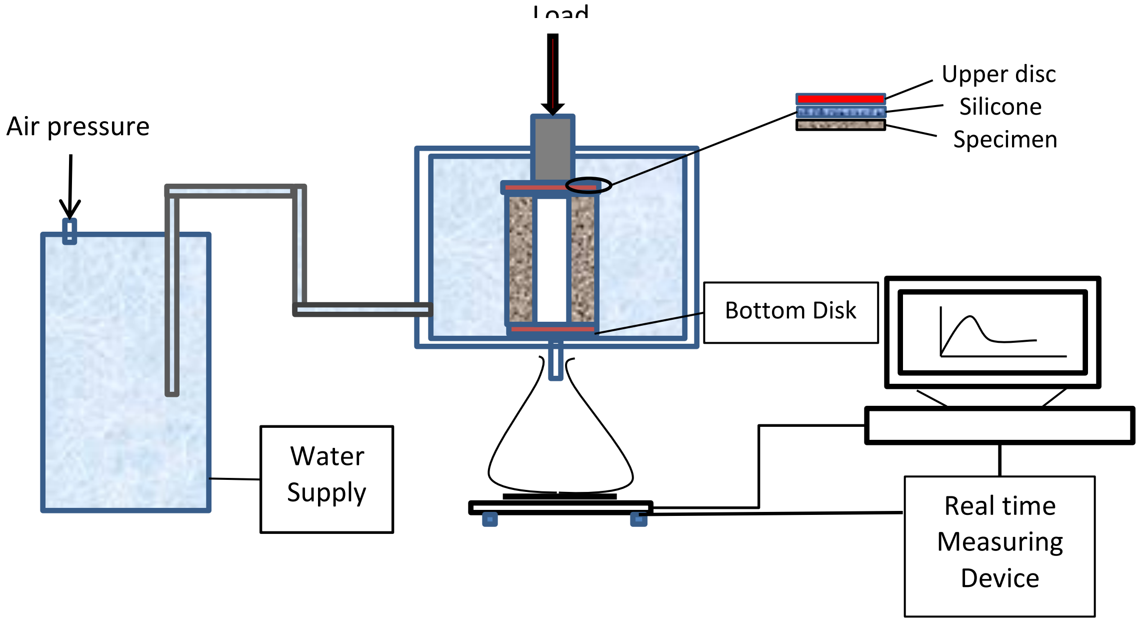

Figure 5.4. Schematic View of the Test Setup for Permeability Measurement under Compressive Stress (Adapted from Biparva [39])

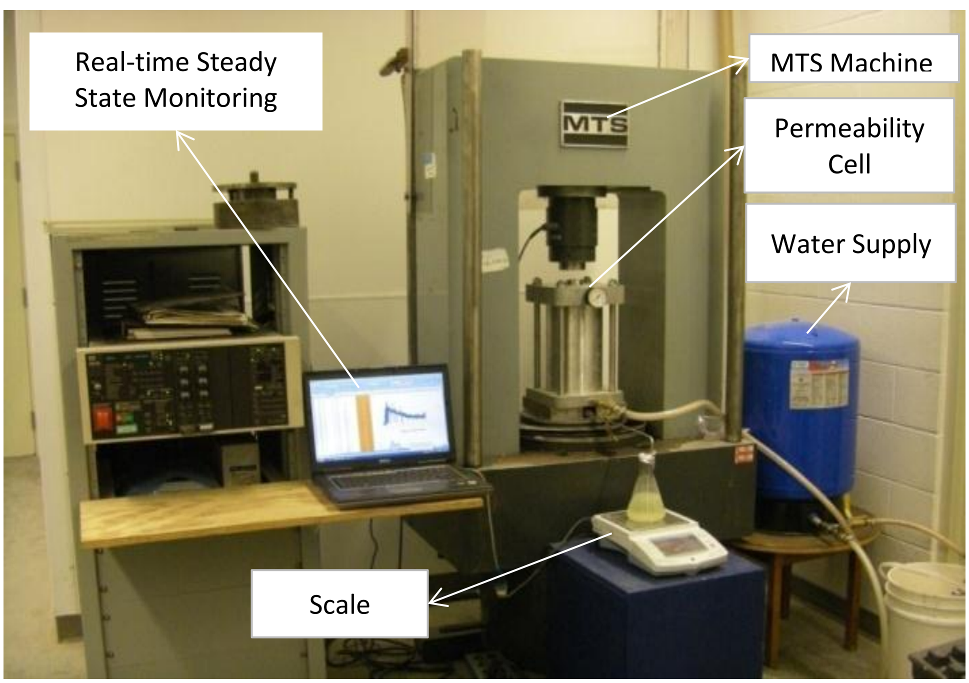

Figure 5.5. Measuring the Water Permeability under Stress

The plain and fiber-reinforced mortar and concrete specimens were subjected to five stress levels equal to 0%, 25%, 50%, 75% and 90% of the compressive strength. For each load level, at least two hollow cylindrical specimens were examined within the permeability cell per mix, while three solid cylinders were tested to determine the compressive strength and stress- strain diagram of the specimen. Pressurized water (at 100 psi = 0.70 MPa) was introduced around the outer wall of the hollow cylinder inside the permeability cell and allowed to permeate through to the inner core of each specimen. This constant water pressure was expected to have similar effect on all tested specimens. The mass of outflow was collected in a flask and measured on a highly sensitive weighing scale (precision = 0.01 g) to be displayed on a computer screen associated with the setup. In this manner, the flow was monitored until it reached a steady-state condition (as described below). At this point, the water permeability of the specimen was evaluated according to Darcy's law for laminar flow as follows [107]:

$$K = \frac{Q}{2\pi h \Delta P} ln \frac{r_2}{r_1} \qquad 5.1$$

Where,

K= the coefficient of water permeability (m/s);

Q= the rate of water flow (m^3/s);

h= the specimen's length (m);

ΔP= the pressure head (m);

r_2 and $r_{1=}$ the outer and inner diameter of the hollow cylinder (m).

Establishing the Steady State Condition of Flow

As mentioned earlier, a crucial parameter for a steady-state flow system is the system constant mass flow rate. This parameter was used to define the steady-state condition in the present study as follows: the test was carried out until such time that the weight of the collected water in the flask was the same at any two consecutive time intervals. The time history of a sample flow that has reached equilibrium is shown in Figure 5.6, wherein a tolerance in successive records of 5% or less, with respect to the previously recorded value, was considered acceptable. A typical test was seen to take anywhere from a few hours to two weeks for the flow to reach a steady-state condition. The duration was seen to depend largely on the mix proportion and the level of applied stress, with larger load levels resulting in shorter durations.

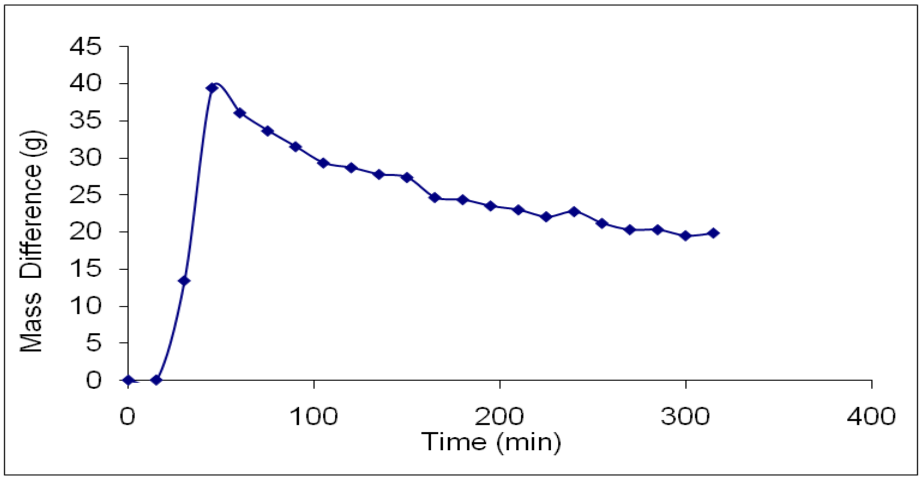

Figure 5.6. Time History of Water Flow Describing the Onset of Steady State

5.3.2. UPV Measurements

The Ultrasonic Pulse Velocity (UPV) in mortar specimens was determined with a commercially available meter and its accompanying 54 kHz transducers. The stress was applied by a uniaxial compression machine, and the UPV was determined at different stress levels (varying from 0% to 95% of compressive strength) for each specimen. These stress levels were intended to coincide with those at which water permeability was measured. Three sets of readings were taken at each stress level and averaged to represent the data point. The UPV was measured in the direction perpendicular to the application of compressive stress with the load held constant at each stress level for the duration of measurement, similar to that for the permeability evaluation. This meant that while the load was applied in the direction of casting, the UPV was evaluated in the direction perpendicular to casting or loading. Recall that the permeability was evaluated in a similar manner, so that whereas the loading was along the casting direction and axially applied, the direction of flow was in the radial direction being through the thickness of the hollow cylinders. Figure 5.7 shows a schematic of the set up for the UPV test as well as an illustration of an evaluation in progress.

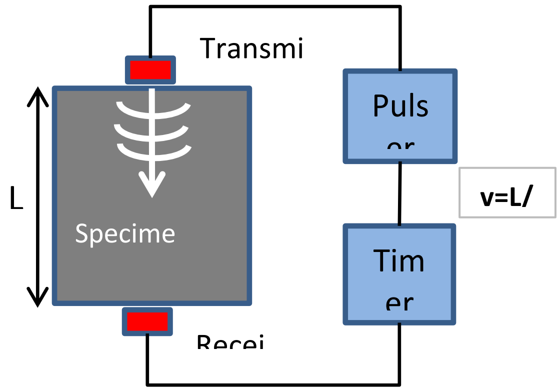

a) Schematic of the UPV Test Setup

b) UPV Measurement in Progress

Figure 5.7. Measuring the Ultrasonic Pulse Velocity through Cubes

5.3.3. Compressive Stress-Strain Test

The mortar and concrete cylinders were first capped with sulfur according to ASTM C617 [108] and then tested in a universal testing machine with a built-in load cell of 1000 kN capacity (MTS 1000). Three replicates were tested in each case. The cylinders were instrumented to derive the compressive stress-strain response as per ASTM C469 [109]. The loading surface was kept plane and parallel through sulfur capping.

Three linear variable displacement transducers (LVDTs) were arranged at 120^{o} about the longitudinal axis. The data acquisition system obtained load, stroke, and LVDT measurements at 5 Hz. The test was conducted using a fixed rate of displacement at 1.25 mm/min as per ASTM C469 [109].

Figure 5.8. Compressive Strength Test According to ASM C469

5.3.4. Image Acquisition and Analysis

As mentioned earlier, a major advantage of this technique is the absence of any special requirement for sample preparation. The X-ray Skyscan 1076 machine located at the micro-tomography laboratory in the Department of Pharmacy, University of Alberta was used for this study. The specimens were placed in the bed of the X-ray machine and were restrained using masking tape to control movement. Figure 5.9 shows the XRT device and a sample fixed in the bed. An X-ray source set to 70 kV and 139 μA was used to take 2D projections through a 1.0 mm (0.039 in) aluminum filter. Images were taken at intervals of 0.5 degrees through a 180 degree rotation. This machine was capable of detecting pixels with dimensions as small as 18 μm.

Each sample was first scanned under the condition of no stress. Then the same sample was loaded to different load levels between 0 to 100 percent of ultimate and then scanned again after unloading the specimen.

Figure 5.9. XRT Device Used in This Study

The *raw images* obtained from the micro tomography machine require reconstruction, which was performed by utilizing a modified Feldkamp back-projection algorithm. In this study, the Skyscan CT-Analyser Software (version

2.6) was implemented for reconstructing and analyzing the voids and pores within the mortar specimens. A total of 1050 reconstructed images from the bottom to the top of the specimens were taken and are referred to as the image-dataset.

After reconstruction, the images were processed by first *selecting a fixed region of interest* on the database images. The selected region of interest across all the selected image levels was integrated to define the sub-volume of the database within which the analysis was to be performed. Since in this study the main focus was on the changes in the specimen's microstructural parameters under different levels of stress, a constant region of interest was required in order to allow for comparison across these changes within a specified delineated region. The images were then converted to a binary format using a *thresholding* technique. Thresholding is one of the simplest methods of image segmentation that converts grey scale images (wherein each image pixel has a value between 0 to 256) into binary (where only two values of 0 or 1 are possible for each pixel) [110]. In thresholding, each pixel value is read; then replaced by either 1 or 0, depending on whether it was above or below a certain threshold value. In general, this separates air from the solid material. Although this could be done either way, in this study, the pixels representing air (voids and cracks) were thresholded to have a value of 1 (black) and the solid (non-air) pixels became white with a value of 0. After thresholding, the software performs the analysis and the *processed image* is then finalized. Figure 5.10 illustrates the different stages of the image processing described above.

The most important factor in this process is defining a threshold value. In this research, the selection of threshold value was done manually by comparing binary images produced from several threshold values against the original grayscale image.

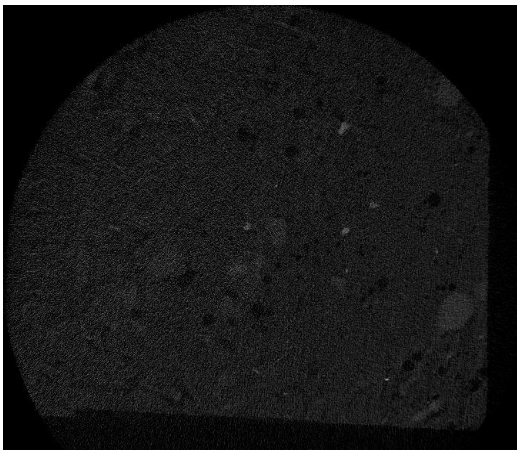
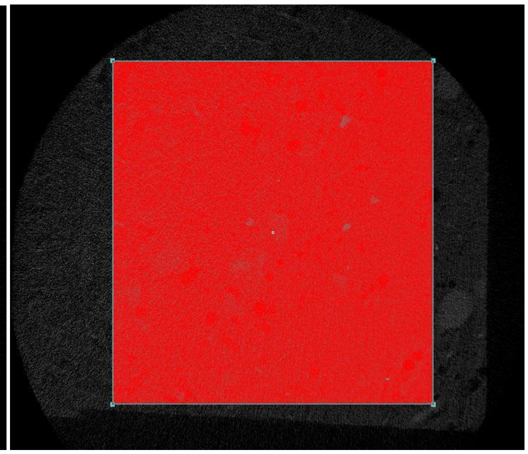

(a) (b)

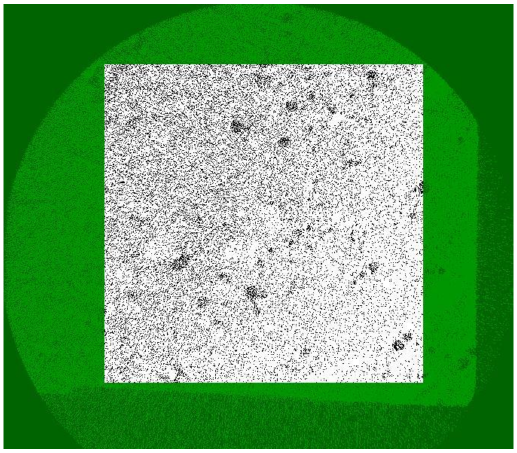
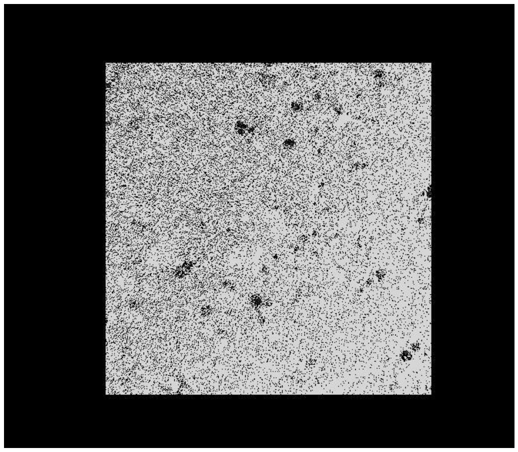

(c) (d)

Figure 5.10. Different Stages of Image Analysis: a) Raw Image b) Selection of Region of Interest c) Thresholding d) Processed Image

Figure 5.11 illustrates an example of the binary images from a section of a specimen under different loading conditions. This figure shows an example of a change in microstructure and the creation of large cracks in a mortar section under different loading levels varying from 0 to 100% of ultimate stress. This figure shows that at lower levels of loading (Figure 5.11 (a) to (c)), application of compression stress mainly affects the number and distribution of the pores while at higher levels of stress, large cracks initiate and propagate (Figure 5.11 (d) to (f)).

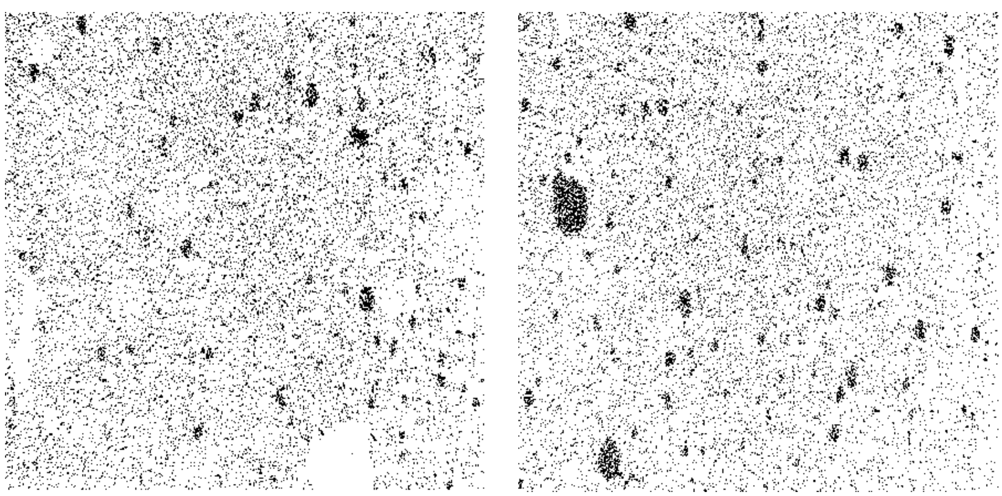

(a) (b)

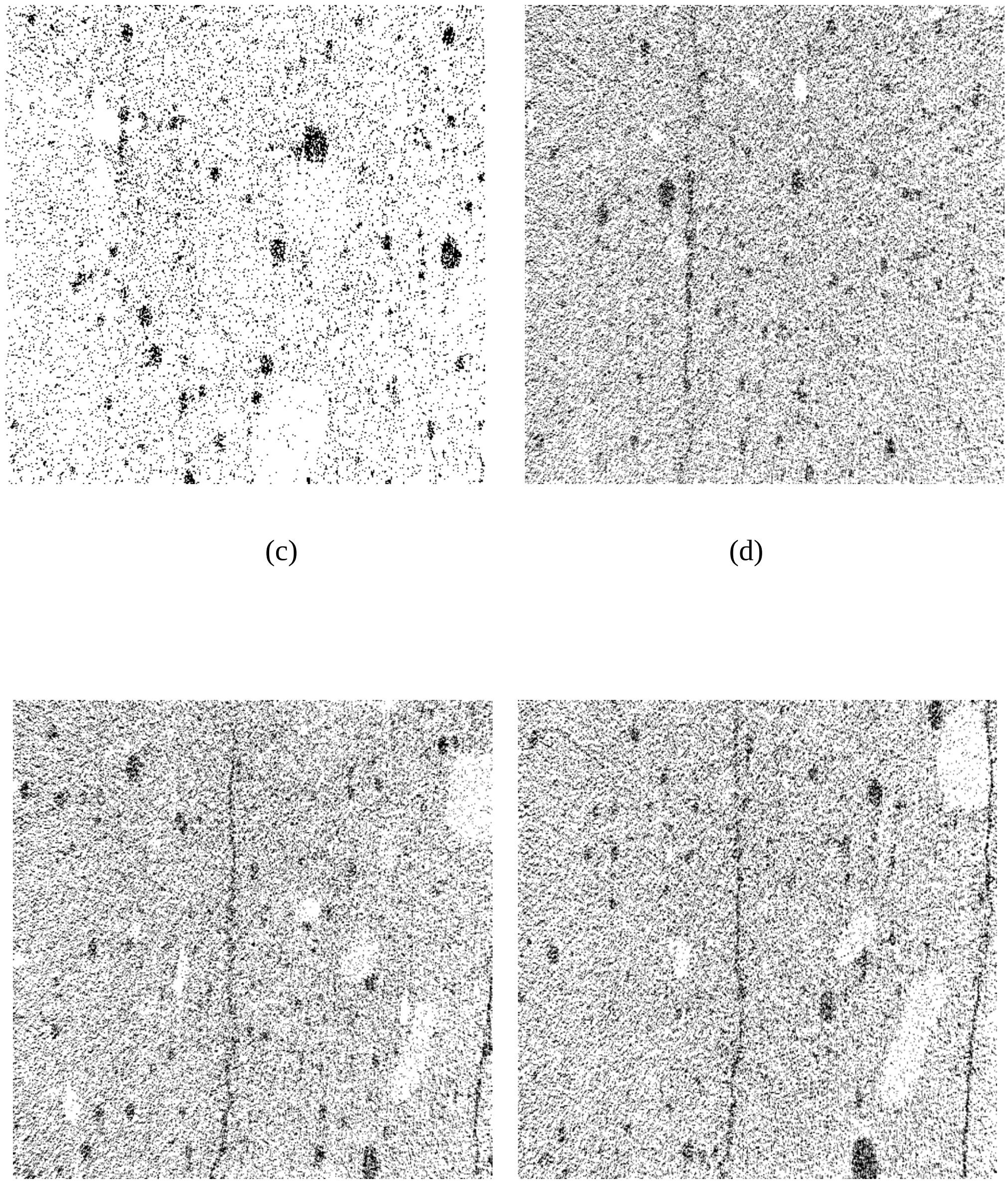

(c) (d)

(e) (f)

Figure 5.11. An Example of Change in Microstructure of a Mortar Section under Different Loading Levels (a=0%, b=24%, c=44%, d=64%, e=85% and f=100% of Ultimate)

As described earlier in this chapter, the space limit within the machine used for the XRT study allowed scanning of objects up to a maximum dimension of 20 mm. Thus, small Type S plain and fiber reinforced mortar cubes (20 mm x 20 mm x 20 mm) were cast from the same mix used to prepare specimens for permeability and UPV measurement.

The binary 2D and 3D images from mortar Type S samples as represented by Figure 5.10 were analyzed to quantify the pore parameters. Both 2D and 3D images were used to calculate the total porosity (φ) of each sample and 2D image sections were further analyzed to evaluate additional parameters including: void size distribution, specific surface area (α) of the pores, void spacing factor (L), void shape factor (S) and number of connected pores (NCC). Both air voids and cracks were classified as void compared to the solid part of the cement-based material. With the exception of the number of connected pores, which is evaluated later in Chapter 8, the other afore-mentioned parameters were calculated using Equations 5.1 to 5.5 as given by Zhang et al., 2005 [111].

$$\varphi = \frac{\text{Area (Volume) of pores}}{\text{Total Area (Volume)}} \qquad 5.2$$

$$\alpha = \frac{16}{\pi}\frac{\sum n_i d_i}{\sum n_i d_i^2} \qquad 5.3$$

$$L = \frac{3}{\alpha} * [1.4 * \left(\frac{P}{A} + 1\right)^{0.33} - 1] \qquad \text{If } \frac{P}{A} >= 4.33 \qquad 5.4$$

$$L = \frac{P}{\alpha A} \qquad \text{If } \frac{P}{A} < 4.33 \qquad 5.5$$

$$S = \frac{4\pi R}{T^2} \qquad 5.6$$

Where:

n_i= number of voids with a particular diameter

d_i= void diameter

P= volume of paste in the cement-based material

A= air content

R= area of the void

T= perimeter of the void

6. Test Results and Discussions

6.1. Mechanical Properties

As described in Chapter 5, cylinders of size 100 mm diameter and 200 mm height were tested as per ASTM C469 [109] by using an MTS 1000 material testing system, LVDTs, and an electronic data acquisition system. The representative stress-strain responses in compression for mortar (MS: Plain Mortar and FMS: Fiber Reinforced Mortar) and concrete (PC: Plain Concrete and FRC: Fiber Reinforced Concrete) are shown in Figure 6.1 and Figure 6.2 and the corresponding material properties have been listed in Table 6.1 .

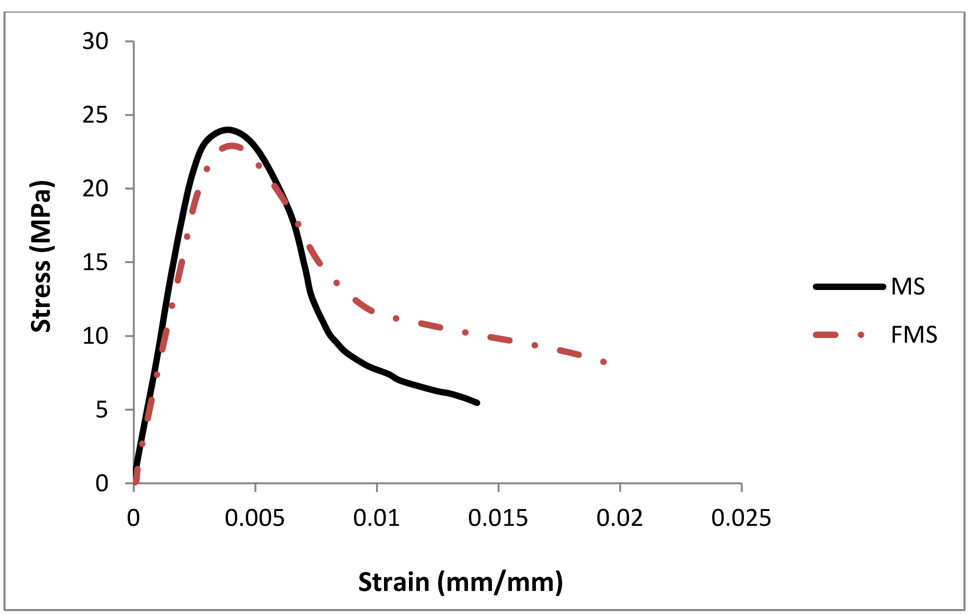

Figure 6.1. Representative Compressive Response of Plain and Fiber Type S Mortar

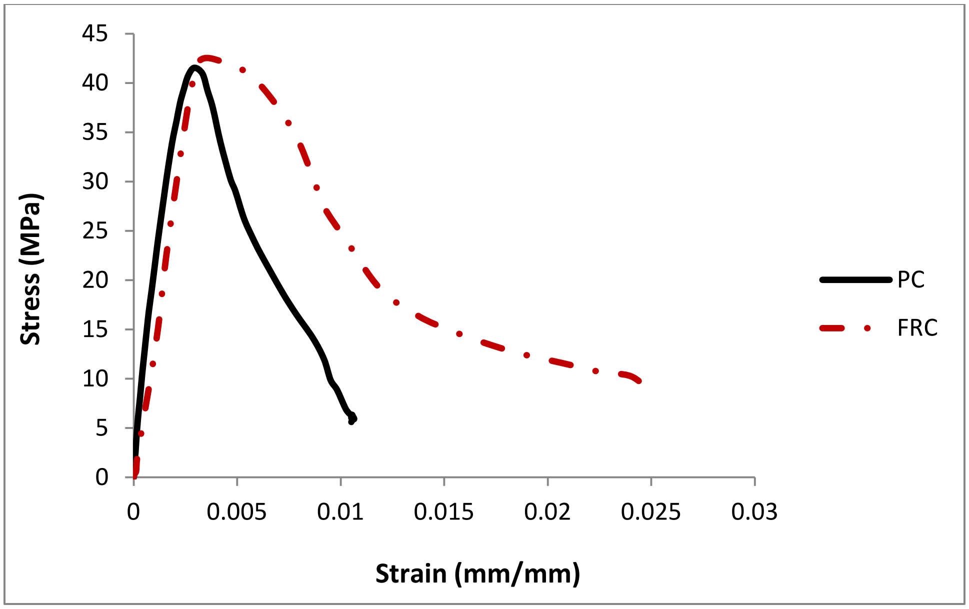

Figure 6.2. Representative Compressive Response of Plain and Fiber Reinforced Concrete

Mix	**Compressive Strength (f'c)(MPa)**		**Modulus of Elasticity (E_c) (MPa)**	
	Value	**STDEV**	**Value**	**STDEV**
Plain Mortar (MS)	23.9	0.51	9285	582
Fiber Reinforced Mortar (FMS)	22.8	1.3	7671	973
Plain Concrete (PC)	41.5	1.5	33754	1258
Fiber Reinforced Concrete (FRC)	42.3	1.1	32512	1926

Table 6.1. Mechanical Properties of Mixes Used in This Study

As expected from the mix design, two ranges of compressive strength were obtained (about 20 MPa for mortar specimens and about 40 MPa for concrete specimens) though they exhibited a wider range of variation in modulus of elasticity (about 8500 MPa for mortar specimens and 33100 MPa for concrete specimens).

6.2. Effect of Stress on Water Permeability Coefficient

The effect of compressive stress on permeability of both plain and fiber-reinforced mortar Type S has been presented in Figure 6.3. Moreover, Figure 6.4 shows the variation in water permeability due to the applied stress in plain and fiber-reinforced concrete, which is expressed here as a percentage of the compressive strength. The lines in both figures represent the average of the two measured permeability data on a logarithmic scale shown on the figure at each stress level.

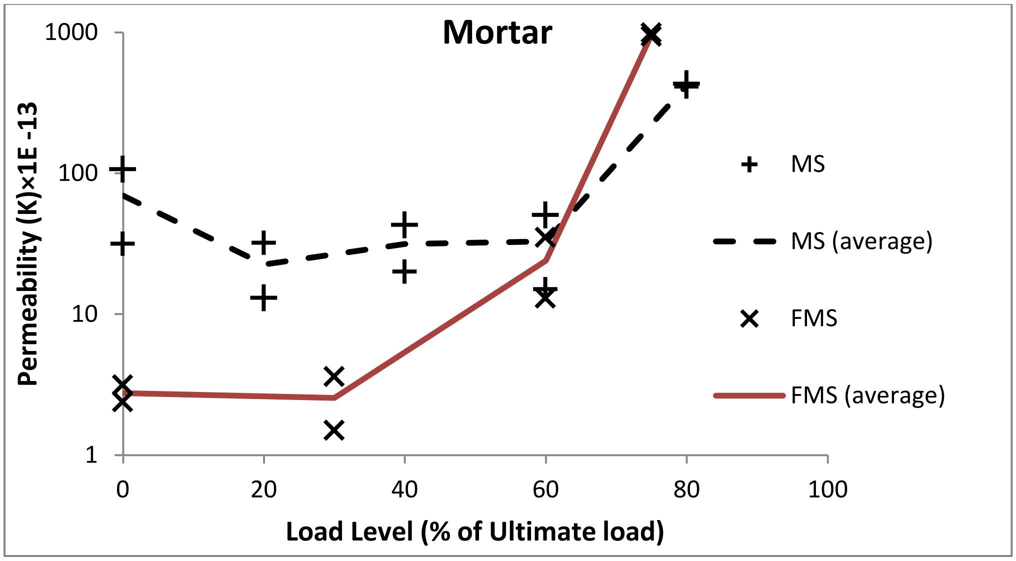

Figure 6.3. Effect of Compressive Stress on the Water Permeability in Plain and Fiber-reinforced Mortars, MS: Plain Mortar, FMS: Fiber Reinforced Mortar (0.25%) Fiber

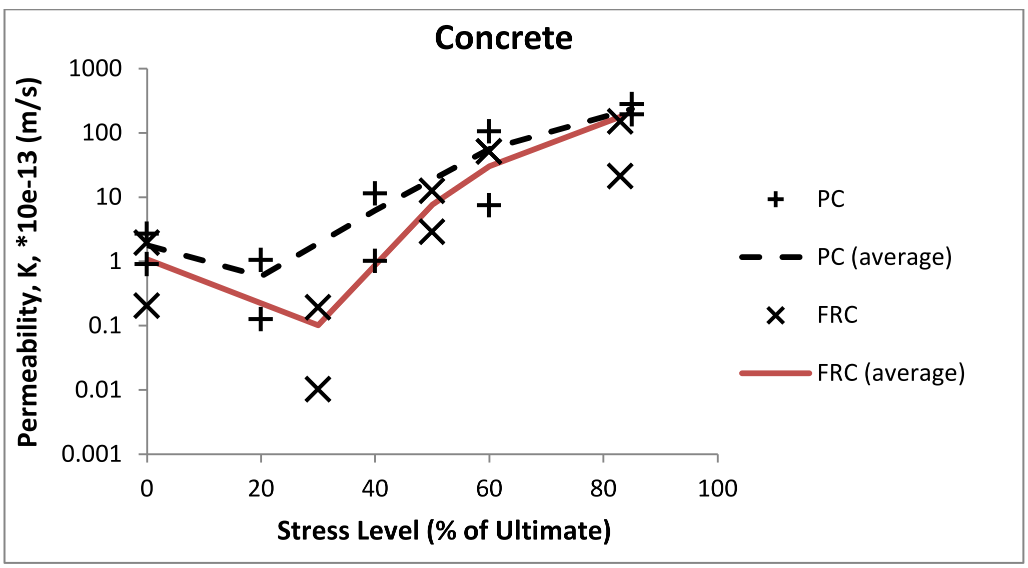

Figure 6.4. Effect of Compressive Stress on the Water Permeability in Plain and Fiber-reinforced Concrete, PC: Plain Concrete, FRC: Fiber Reinforced Concrete (0.25% Fiber)

It can be seen that up to 70% of the compressive strength, the permeability in fiber reinforced mortars was lower than in the reference plain specimens. Note that in unstressed specimens, the water permeability of the fiber reinforced mortar was nearly 1/50 of that of plain mortar. This observation is in agreement with the findings of Banthia and Bhargava [22] or Vondran and Webster [23] but was contrary to the results of Al-Tayyib [25] and Toutanji et al. [112]. The reduction in permeability due to the presence of fiber reinforcement is likely due to a decrease in bleeding and internal shrinkage cracking associated with fiber reinforced mortars. This has been attributed to the micro-polypropylene fibers, which are known to reduce the bleed channels and thus decrease the available flow paths [29]. However, beyond a stress level equal to 70% of the compressive strength of the mortar, the fibers were no longer as effective in reducing the permeability coefficient. This was likely due to the formation of a dominant single crack through crack coalescence at higher loads. In other words, permeability transforms from being a bulk phenomenon at lower loads to a local one at loads closer to failure.

In Figure 6.3 and Figure 6.4 one may identify the so called ‘threshold stress’, which is defined as the stress level below which the permeability coefficient shows no increase (and may in fact display a significant drop). On the other hand, at load levels beyond the threshold stress, the coefficient of permeability increases and is highly sensitive to the applied stress. The perceived drop in the plain mortar samples may be attributed to the consolidation and subsequent closure of voids and micro-cracks in the mortar when it is subjected to compression. The occurrence of the threshold stress may be explained further based on the findings of Samaha et al. [6] who concluded that mortar cracking was far more influential in increasing the rate of mass transport in concrete than cracking at the aggregate-paste interface. This implies that below the threshold stress level, the cracks are predominantly along the aggregate-paste interface, with the bulk cement paste itself staying mostly intact. However, at higher loads, the cracks extend into the bulk cement paste, and hence one notes a rapid increase in the permeability coefficient. It is seen from Figure 6.3 and Figure 6.4 that the threshold stress was 20% of the compressive strength for plain specimens, whereas it was about 30% of the compressive strength in fiber-reinforced specimens. The latter value of threshold stress at about 30% of ultimate is in agreement with the findings of Banthia and Bhargava [22].

Notice in Figure 6.3 and Figure 6.4 that fibers have been very useful in reducing the permeability, so that up to even about 60% of compressive strength, the permeability of fiber reinforced specimens were lower than that of unstressed specimens in all mixes designed. This result shows that while the primary purpose of fiber reinforcement was to improve the toughness and energy absorption of concrete, the other significant benefit lies in improving the durability properties of concrete through reduced water transport. However, these results do not confirm the findings of Rapoport et al. [37] and Banthia and Bhargava [22] who found that fiber-reinforced concrete maintains its permeability close to its unstressed state even beyond the cracking stage.

All the data presented in Figure 6.3 and Figure 6.4 have been displayed on a single graph in Figure 6.5 to compare mortar and concrete permeability as it changes during loading. In unstressed specimens and up to about 40% of ultimate strength, Portland cement concrete (both plain and fiber-reinforced) has lower permeability than Type S mortar specimens. One may explain the difference as follows. Since the Portland cement has more silicates than Type S mortar (see Table 5.3 and Table 5.4), the resulting hydrated product has more CSH gel and thus fewer capillary pores, which results in lower porosity and higher strength. Note that the strength of concrete specimens is almost twice that of mortar specimens. Moreover, incorporating the coarse aggregates is also shown to be effective in reducing the permeability [6]. However, the results of this study do not provide evidence that incorporating the aggregates changes the threshold stress level of concrete as compared to mortar.

According to Figure 6.5, although at ultimate stress, the concrete specimens still have lower permeability than the mortar specimens, beyond 50% of compressive strength, due to formation of a dominant single crack through crack coalescence at higher loads, no clear trend in measured permeability of the specimens is observed.

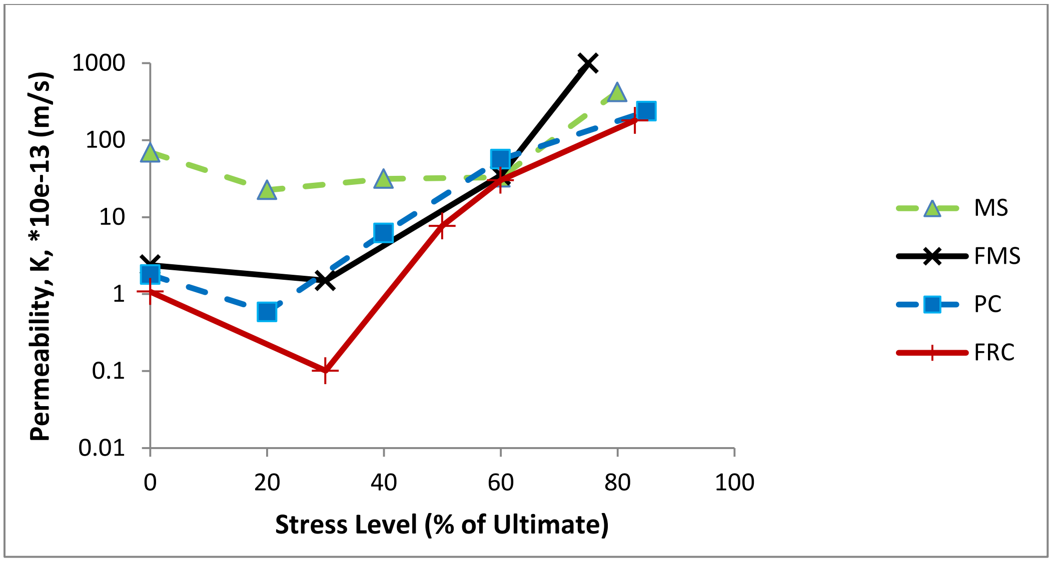

Figure 6.5. Effect of Compressive Stress on the Water Permeability (All Mixes). MS: Plain Mortar, FMS: Fiber Reinforced Mortar (0.25%) Fiber, PC: Plain Concrete, FRC: Fiber Reinforced Concrete (0.25% Fiber)

Figure 6.6 presents the same results as Figure 6.3 and Figure 6.4, but on an arithmetic scale. As seen in this figure, although a threshold stress value of between 20% and 30% of ultimate load still can be observed, it is obvious that the big jump in permeability values occurs at stress level of about 60% of ultimate load for all mix designs. It means that stress levels more than 60% of compressive strength are likely to generate microcracks through the paste that can reduce the durability of the structure. This value denotes the onset of cracks opening through the paste, which results in a network that includes the cracks at the paste-aggregate interface under compression. It corresponds to the onset of the post-elastic range in the stress-strain curve of regular concrete under compression as seen in Section 6.1. As discussed later, these observations support a design approach that limits service load stresses to 60% of peak capacity.

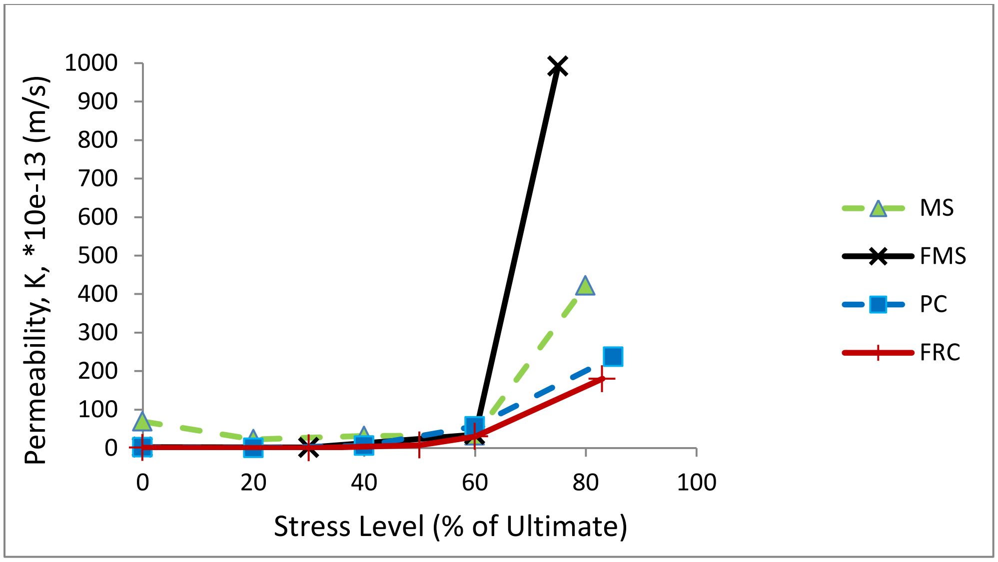

Figure 6.6. Effect of Compressive Stress on the Water Permeability in Plain and Fiber-reinforced Specimens. MS: Plain Mortar, FMS: Fiber Reinforced Mortar (0.25%) Fiber, PC: Plain Concrete, FRC: Fiber Reinforced Concrete (0.25% Fiber)

6.3. Effect of Compressive Stress on Ultrasonic Pulse Velocity (UPV)

The results of UPV measurements on the mortar and concrete specimens are presented in Figure 6.7 and Figure 6.8, respectively.

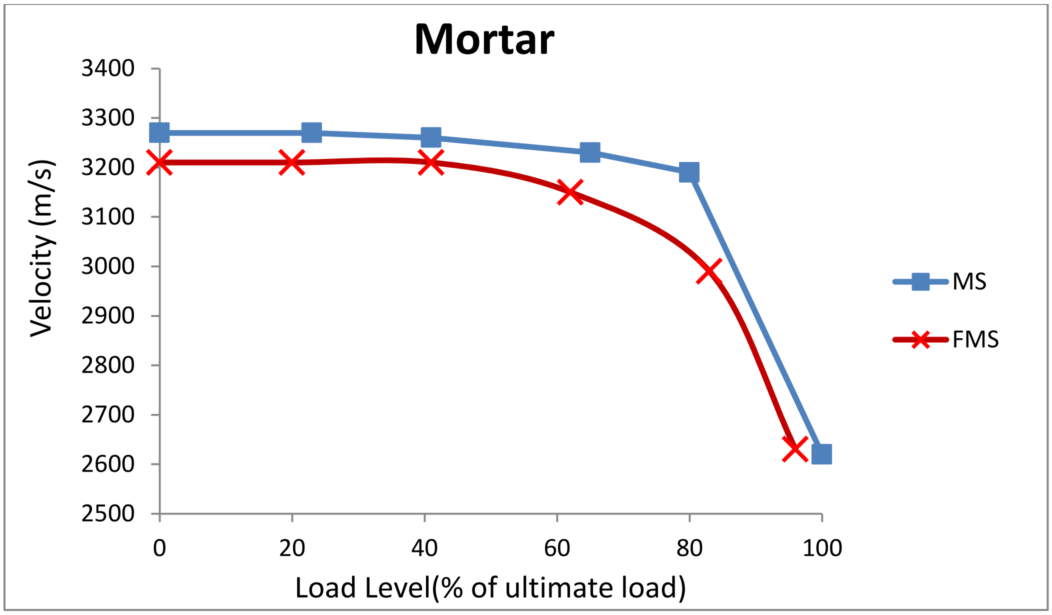

Figure 6.7. Effect of Compressive Stress on the UPV in Mortar Specimens. MS: Plain Mortar, FMS: Fiber Reinforced Mortar (0.25% Fiber)

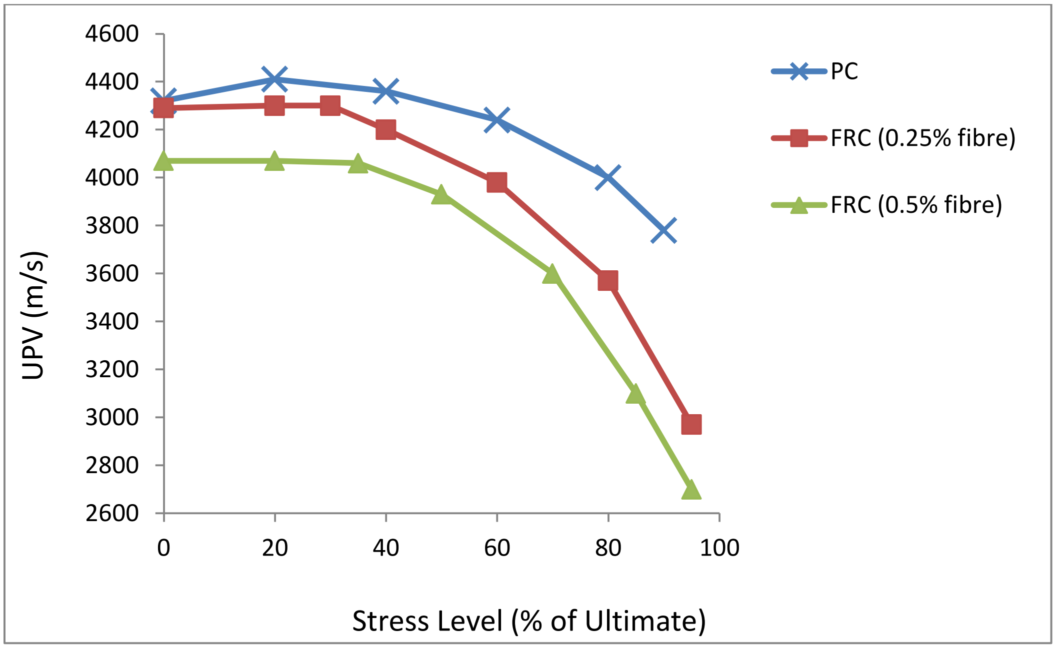

Figure 6.8. Effect of Compressive Stress on the UPV in Concrete Specimens. PC: Plain Concrete, FRC: Fiber Reinforced Concrete

As with the permeability measurement, a threshold stress may be defined on the basis of the data in these figures, such that below this stress, the UPV exhibits little or no change, while beyond this level, the pulse velocity starts to increase. As shown in these figures, both plain specimens (mortar and concrete) have the threshold stress value of about 20% compared to the threshold stress value of about 40% and 30% in mortar and concrete specimens containing 0.25% fiber, respectively. These values are in good agreement with the corresponding value in permeability tests. The existence of this threshold stress level for UPV may be attributed to the consolidation and closure of the voids and shrinkage-induced microcracks when previously unstressed mortar is subjected to compression. The closure of the voids reduces the travel distance and hence travel time of UPV which results in increase in calculated velocity. On the other hand, in higher stress levels, stress-induced cracking increases the distance traveled by the pulse, which is measured as an increase in the time required for the pulse to reach the receiving transducer, and results in a lower calculated velocity. Popovics [80] also noticed the existence of a threshold stress in a wide range of plain mortars and concrete mix designs. Figure 6.8 also shows that by incorporating 0.5% of fiber in a concrete mix design, the threshold stress value in compression in UPV test increases to about 40%. The higher threshold stress in fiber-reinforced mortar and concrete is likely due to the improved integrity through crack-bridging by the fibers.

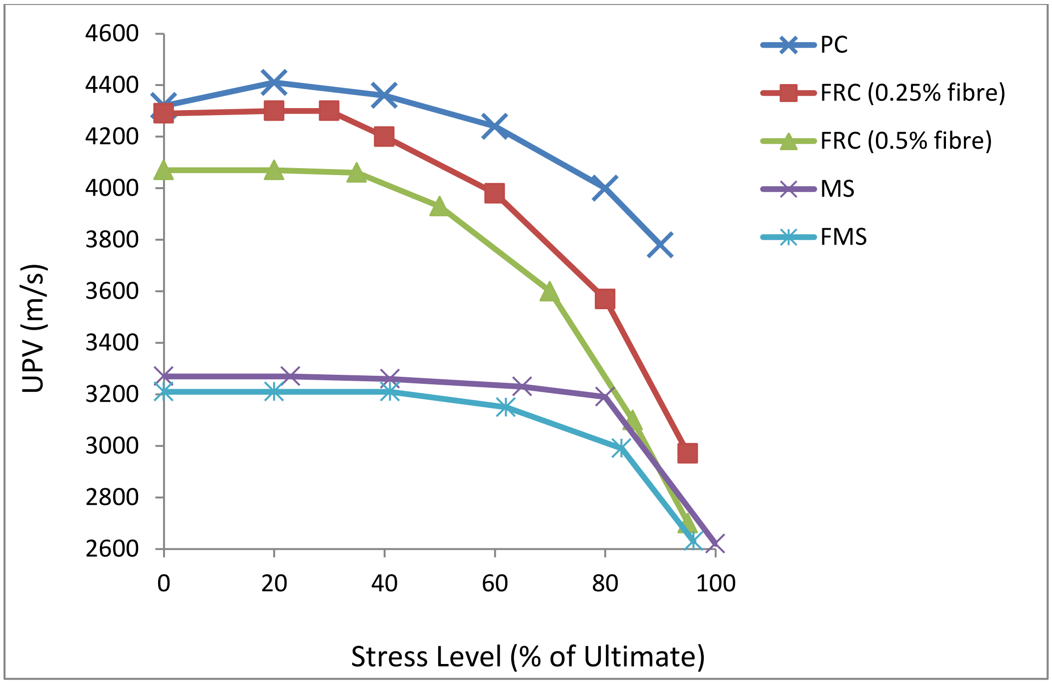

Figure 6.9. Effect of Compressive Stress on the UPV in Mortar and Concrete Specimens. MS: Plain Mortar, FMS: Fiber Reinforced Mortar (0.25% Fiber) , PC: Plain Concrete, FRC: Fiber Reinforced Concrete

Figure 6.9 presents the data of Figure 6.7 and Figure 6.8 in one graph. The figure shows that UPV is higher in concrete specimens compared to mortar specimens probably due to higher modulus of elasticity and incorporation of aggregates in concrete as described in Section 3.2. The figure also shows that in each case (mortar or concrete), the UPV for both fiber-reinforced and plain specimens does not change significantly. This is in agreement with the findings of Nagabhushanam et al. [113], who reported that in concrete specimens with fiber content ranging between 0.1 to 2 % by volume, there was minimal change in the pulse velocity compared to the plain reference concrete. However, as seen from

Figure 6.9, the UPV did change significantly by increasing the compressive strength from 20 MPa in Type S mortar specimens to about 40 MPa in concrete specimens. This is probably due to the lower porosity of Portland cement concrete due to a higher amount of CSH gel in concrete compared to Type S mortar, as well as the existence of coarse aggregates in concrete mixes resulting in a higher modulus of elasticity compared to the Type S mortar specimens. As seen in Figure 6.9, after about 75% of ultimate stress, the UPVs for all specimens approach each other. This is likely due to the creation of very large cracks and a sharp increase in the number of cracks.

6.4. Effect of Stress on Microstructure and Crack Parameters

As described in Chapter 5, because of the limitation of the machine that was used for XRT studies, which allows for scanning objects up to a maximum dimension of 20 mm only, small Type S plain and fiber reinforced mortar cubes (20 mm side) were cast from the same mix as used to prepare specimens for the permeability and UPV measurements. The XRT technique was used to examine the change in microstructure and crack parameters of specimens including total porosity, the air void size distribution, the specific surface area, void spacing factor and the void shape factor. These parameters are discussed in the following sections.

6.4.1. Total Porosity

Both 2D and 3D images were analyzed to calculate the porosity of specimens. In 2D cases, the middle section of each specimen was selected for image analysis, while in 3D measurements all sections were analyzed, and the corresponding porosities were calculated. For each mix at any load level, four specimens were analyzed and the average and standard deviation of the results were calculated and presented in Table 6.2 and Table 6.3, for the plain and fiber reinforced mixes, respectively.

The results show that the porosity calculated from both 2D and 3D images were close (with a maximum difference of about 14%) with 2D images yielding higher values than the 3D ones.

Plain Mortar (average of four specimens)					
Load Level	0.00	0.18	0.39	0.62	0.88
2D Porosity (%)	18.87	19.51	21.28	22.61	25.33
Standard Deviation	2.07	1.80	2.11	2.38	2.33
3D porosity (%)	17.76	18.78	19.25	20.01	22.57
Standard Deviation	1.92	2.00	1.71	1.83	1.92
2D & 3D difference (%)	5.9	3.7	9.5	11.5	10.9

Table 6.2. Values of 2D (Middle Section) and 3D Porosity of Plain Mortar Specimens

Fiber Mortar (average of four specimens)						
Load Level	0.00	0.24	0.44	0.64	0.85	1.00
2D Porosity (%)	18.02	19.35	20.98	20.83	22.32	23.39
Standard Deviation	2.58	1.80	2.65	2.19	2.99	2.56
3D porosity (%)	16.22	16.66	18.08	18.21	19.38	24.47
Standard Deviation	1.98	2.31	1.00	1.62	1.58	2.56
2D & 3D difference (%)	10.0	13.9	13.9	12.6	13.2	-4.6

Table 6.3. Values of 2D (Middle Section) and 3D Porosity of Fiber Reinforced Mortar Specimens

For comparing the change of porosity with increasing load level in plain and fiber reinforced mortars, the data presented in Table 6.2 and Table 6.3 are plotted in Figure 6.12 and Figure 6.13. According to these figures, in both 2D and 3D analysis and for plain and fiber reinforced mortar specimens, the total porosity increases for an increase in the stress levels, and the porosity of fiber reinforced specimens is less than that of plain specimens. From the results presented in Table 6.2, Table 6.3 and Figure 6.11, it can be seen that the difference between total porosities (3D) at load levels close to ultimate (i.e. 90 percent of compressive strength) and unstressed porosities in plain and fiber reinforced mortars are about 3.2 percent and 4.8 percent, respectively. For the range of porosities calculated here, this is equal to an increase of about 20% to 30% of unstressed porosities while we approach the ultimate load levels. In other words, loading the specimens up to about 90% of ultimate increased the porosity by less than 30 percent.

It should be noted that although Figure 6.10 and Figure 6.11 show a gradual increase in total porosity of mortar specimens, they do not provide any information about the nature of this increase. In other words, from these figures it is not clear whether the porosity increase is due to the creation of new discrete pores or the propagation of existing pores and cracks under stress elevation.

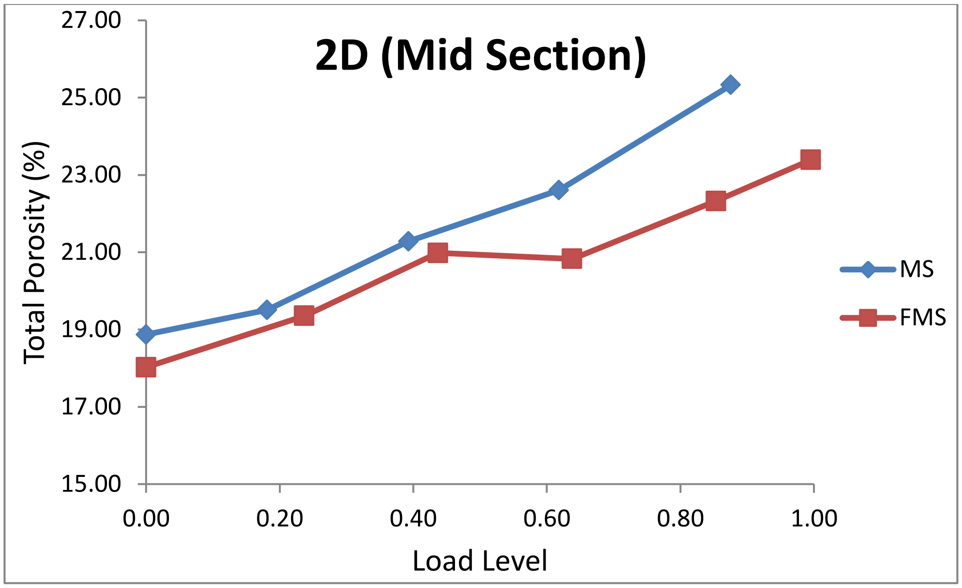

Figure 6.10. Change in 2D Total Porosity of Plain and Fiber Mortar Measured at the Middle Section of Specimen (Average of Four Samples). MS: Plain Mortar, FMS: Fiber Reinforced Mortar (0.25% Fiber)

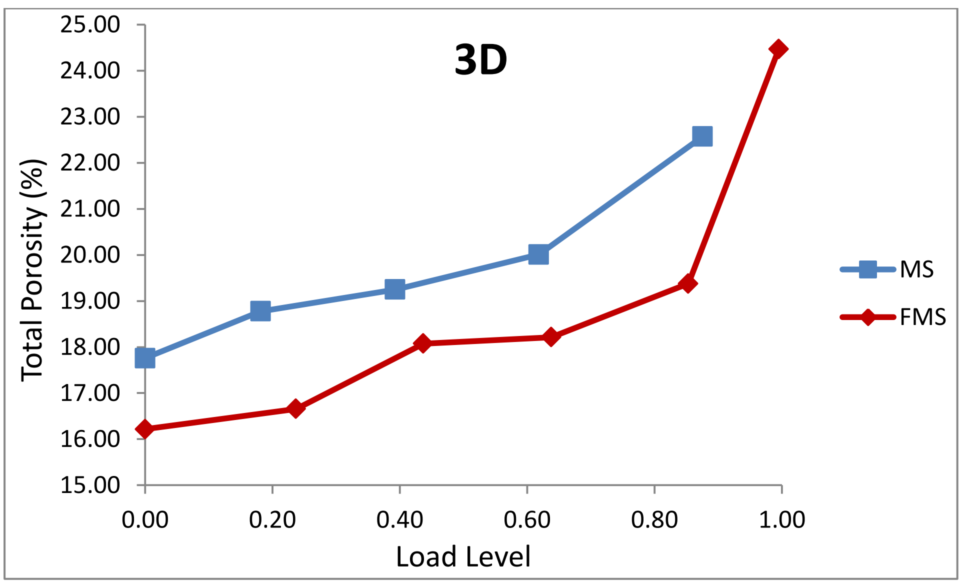

Figure 6.11. Change in 3D Total Porosity of Plain and Fiber Mortar (Average of Four Samples). MS: Plain Mortar, FMS: Fiber Reinforced Mortar (0.25% Fiber)

6.4.2. Air Void Size Distribution

Figure 6.12 and Figure 6.13 show the frequency histogram of air voids for a representative specimen of the two mixes examined under different stress levels. These two figures show that about 60 percent or more of the voids in all loading levels have an equivalent circle diameter of 18μm (minimum void size measured by XRT) or less and increasing the load does not have a significant effect on this value.

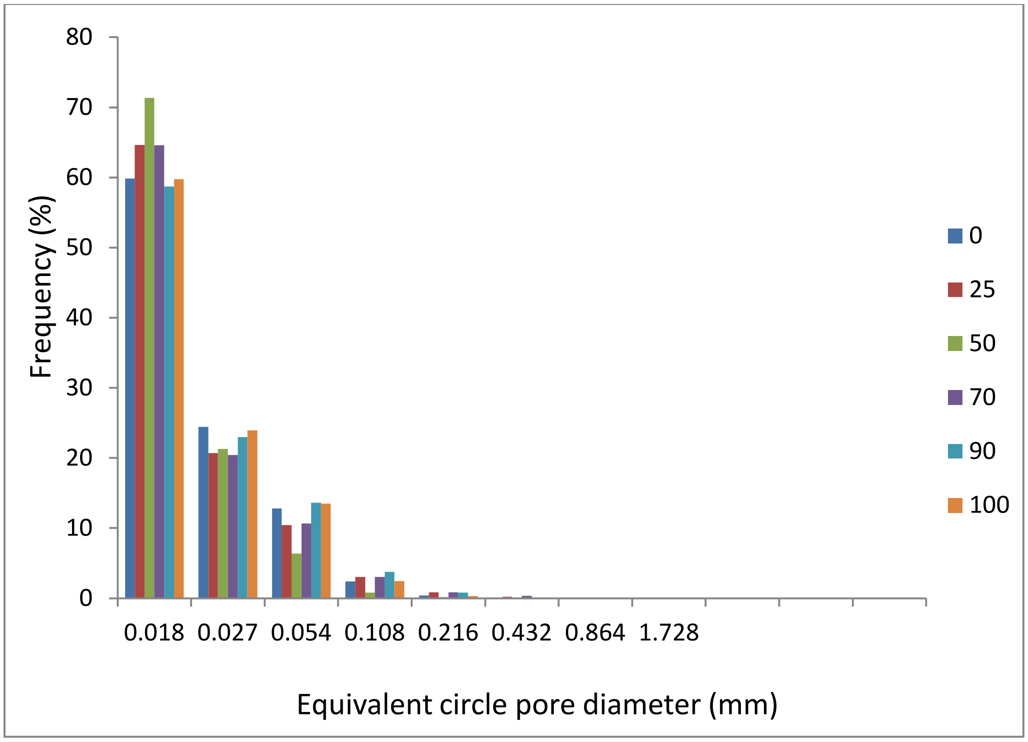

Figure 6.12. Air Void Size Distribution for Plain Mortar Specimen

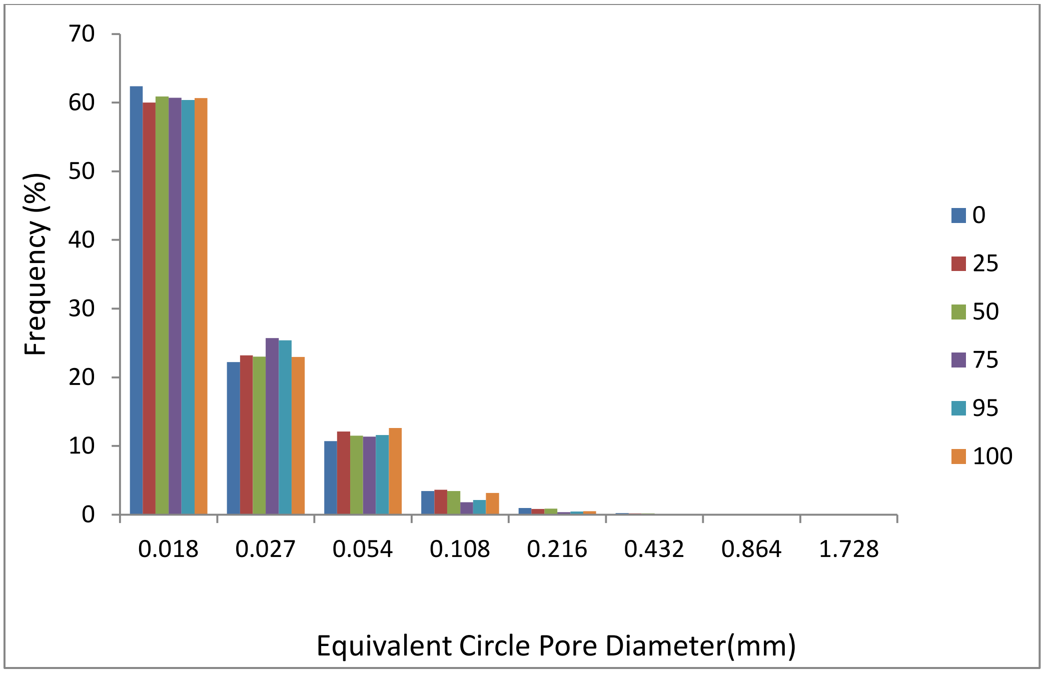

Figure 6.13. Air Void Size Distribution for Fiber Reinforced Mortar Specimen at Different Load Levels

In Figure 6.14, only the values corresponding to the first series of the bars showed in Figure 6.10 and Figure 6.11 have been plotted. This figure presents the percentage of the pores with equivalent circle diameter of 18 µm (the precision of the XRT machine) or less at different loading levels. According to this figure, despite the author's expectation for a reduction in the frequency of small sized pores (i.e. less than 18 µm) by increasing the stress level, no such trend is observed in the measured data and, at load levels close to ultimate, the ratio of pores with diameter of 18 µm and less is almost the same as in unstressed specimens. Overall, the plots of Figure 6.14 show an inverse U shape trend (∩) which is comprised of two different stages: in the first stage, by increasing the load up to 50% of ultimate, the percentage of pores with 18 µm diameter or less increases which could be due to the creation of microcracks and pores as well as closure of larger voids at low levels of stress. After 50% of compressive stress, although some very small microcracks still form due to propagation of existing microcracks and pores, the percentage of pores less than 18 µm decreased again. Moreover, a higher rise in the percentage of pores with 18 µm diameter or less in the first stage of this figure is seen for plain specimens. This is likely due to the existence of more initial larger shrinkage cracks which will be fully/partially closed during earlier stages of loadings and/or creation of more micro-cracks at lower stress levels in plain mortars compared to the fiber reinforced specimens.

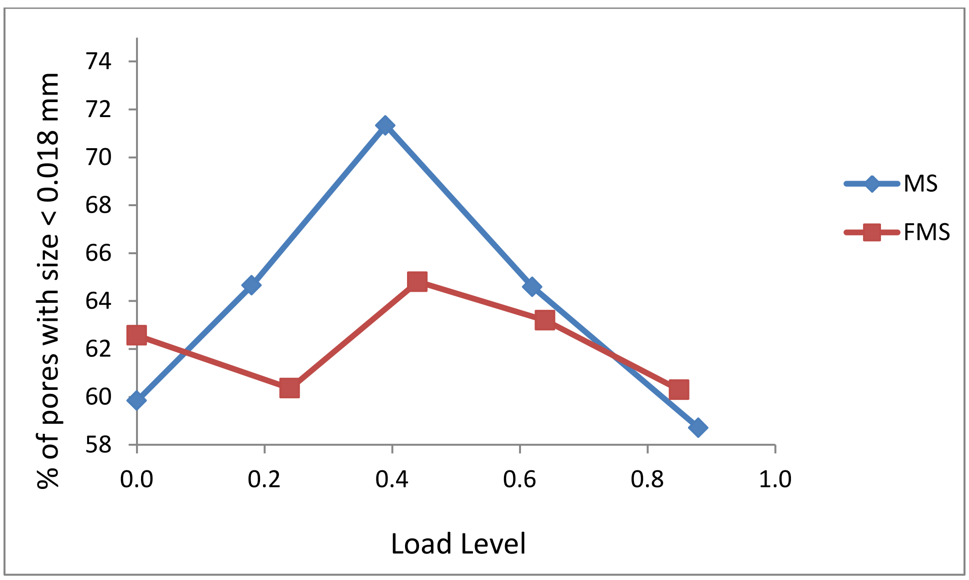

Figure 6.14. Comparison between Changes in the Percentages of the Pores less than 0.018 mm to the Total Pores in Different Load Levels. MS: Plain Mortar, FMS: Fiber Reinforced Mortar (0.25% fiber)

It should be noted that although the *percentage* of these very small pores at the ultimate load levels has not changed compared to unstressed condition, since the total porosity has increased (see Figure 6.10 and Figure 6.11), their corresponding *numbers* in the specimen do indeed increase. This has been calculated and illustrated in Figure 6.15. The numbers plotted in this figure are calculated by multiplying the values in Figure 6.14 by the numbers from Figure 6.11. According to Figure 6.15, by increasing the stress level, up to about 50% of ultimate, the percentage of the pores less than 18 μm increases while after this level, although new microcraks with this size are created, this ratio does not change with increasing load. This is probably due to the propagation of existing voids and previously created microcracks rather than the formation of new small voids for load levels beyond 50% of ultimate stress.

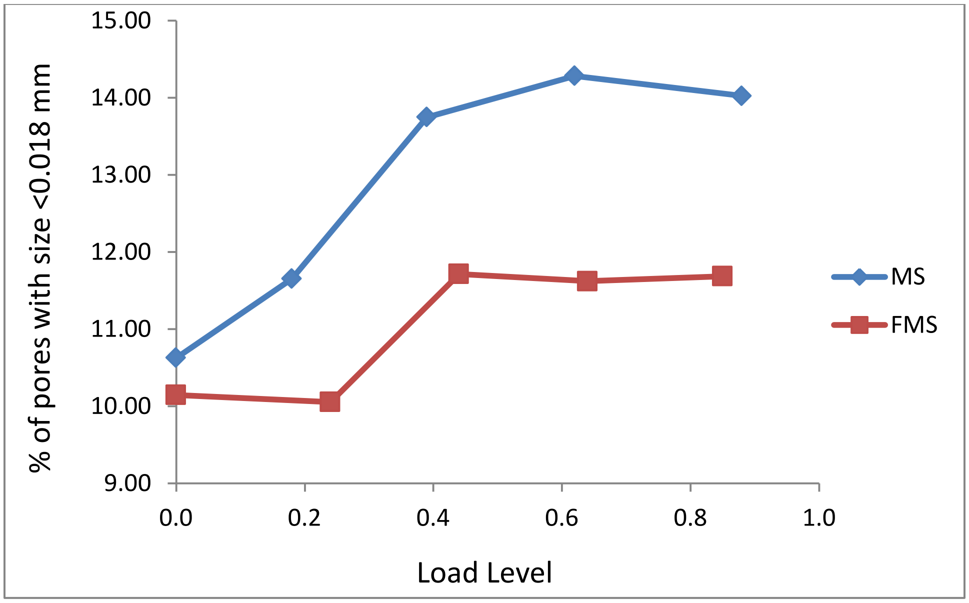

Figure 6.15. Comparison between Changes in the Percentages of the Pores less than 0.018 mm to the Total Volume in Different Load Levels. MS: Plain Mortar, FMS: Fiber Reinforced Mortar (0.25% fiber)

6.4.3. Specific Surface Area

Void specific surface area is a measure of the total surface area of voids, pores and cracks in the air void volume of a specimen under study. According to this definition, for a given total volume of air a greater number of smaller air voids results in a higher specific surface area value. This parameter was calculated for a representative sample for each studied mix using Equation 5.3 [111] and the results are presented in Figure 6.16.

According to this figure, in the unstressed condition the void specific surface area of fiber reinforced mortar is less than that of plain mortar which represents the existence of coarser voids and pores in fiber reinforced mortars along with the lower porosity of these specimens (see Figure 6.11). The coarser air-voids in fiber reinforced mortars is probably due to the lower slump and workability of fiber mixes at the time of casting which results in less specific surface area of voids in unloaded specimens.

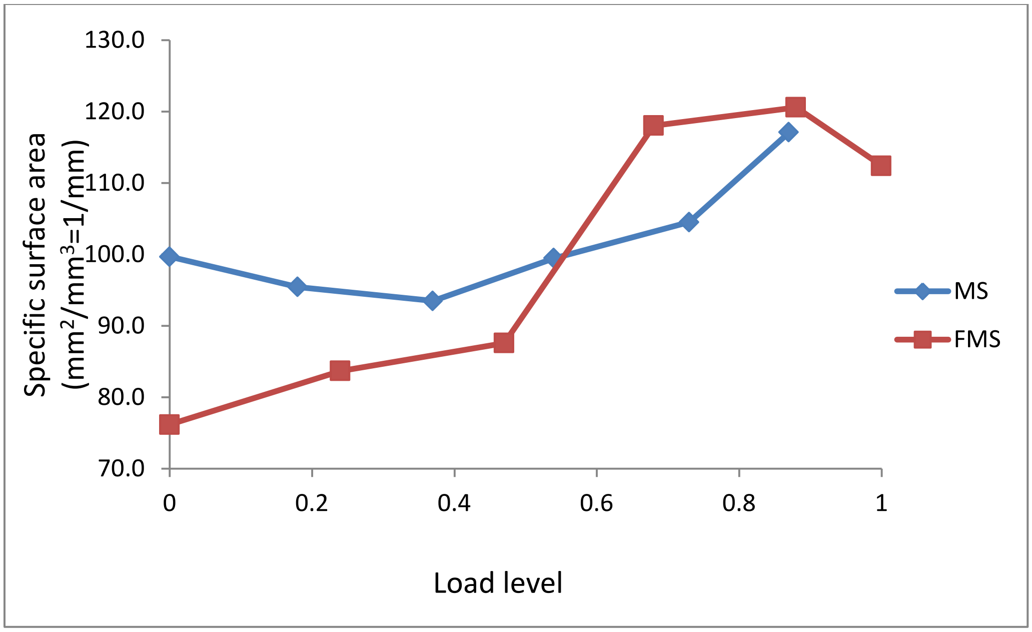

Figure 6.16. Change in Specific Surface Area with Stress. MS: Plain Mortar, FMS: Fiber Reinforced Mortar (0.25% fiber)

By introducing the load, according to Figure 6.16, the plain and fiber reinforced specimens show different behavior in the variation of the specific surface area. While for the plain mortar this parameter decreases slightly at the lower stress levels and later registers a gradual increase, the void specific surface area of fiber reinforced mortars increases under all levels of stress. The initial reduction and then slower rate of increase in the pore specific surface area of plain specimens compared to the change in their porosity, is attributed to the formation of coarser pores in plain specimens which is not in favor of the permeability and UPV test results presented earlier in this chapter. Theoretically, the decrease in the specific surface area by increasing the porosity will happen with the formation of new coarser voids or increasing the size of existing pores while the decrease in permeability or increase in UPV in low stress levels are related to the closure of existing pores and cracks under low levels of stress. On the other hand, increasing the specific surface area of the fiber reinforced mortars with increasing porosity (Figure 6.11) is the result of multiple cracking and creation of small size pores in fiber reinforced mortars under stress.

Figure 6.16 also shows that after about 60% of ultimate stress, the void specific surface area in fiber reinforced mortars becomes higher than that of plain specimens which is due to the creation of the greater amount of smaller voids and bridging of the cracks in the presence of fibers in spite of lower porosity of these specimens as presented in Figure 6.11. It should be noted that by creation and propagation of large cracks, the specific surface area has been reduced in the fiber mortar specimen examined at the ultimate stress level.

6.4.4. Void Spacing Factor

The most widely used paste-void spacing equation is the Powers spacing factor as calculated using Equations 5.4 and 5.5. According to ACI Concrete Terminology [114], void spacing factor is an index related to the maximum distance of any point in a cement paste or in the cement paste fraction of mortar or concrete from the periphery of an air void. This parameter calculates the fraction of paste within some distance of an air void (paste-void proximity). The Powers equation approximates the distance from the surface of all the air void surfaces which would encompass some large fraction of the paste. However, the value of this fraction is not quantified by this equation.

Figure 6.17 presents the calculated void spacing factor value according to Equations 5.4 and 5.5. Each number is the average of three void spacing factor values, calculated for three different sections in each specimen. The figure shows that although both plain and fiber reinforced mortar specimens have almost the same initial value of void spacing factor while they are not under stress; they show two different behaviors under load: increasing the stress level causes the void spacing factor for plain mortar to slightly increase from 440 μm to 490 μm. The change of void spacing factor of plain specimen from unstressed condition to ultimate load shows only about a 10% increase. This slight increase of void spacing factor in plain specimens is probably due to the formation of large cracks from only a single or few cracks which expand and open up. On the other hand, the void spacing factor of fiber reinforced mortar shows a different trend. In overall, up to about 50 percent of loading the void spacing factor does not change while after that, probably because of the formation of multiple cracking in mortar specimens due to the presence of fibers, the parameter drops. After about 75 percent of ultimate stress by creating the large cracks and propagation of a single large crack, similar to the plain mortar behavior, the change in void spacing factor found to be not significant.

Figure 6.17 also depicts that the void spacing factor of fiber reinforced mortars are below the corresponding value of plain mortar under loading. This is due to the creation of multiple micro-cracks in specimens containing fibers under stress which reduces the crack spacing of these materials. At about 75 percent of maximum load, the void spacing factor of fiber reinforced mortar is about 40 percent of the corresponding value of plain mortar where after this stress level the difference between the two diminishes. This stress level is probably the onset of creating large single cracks in fiber reinforced mortars.

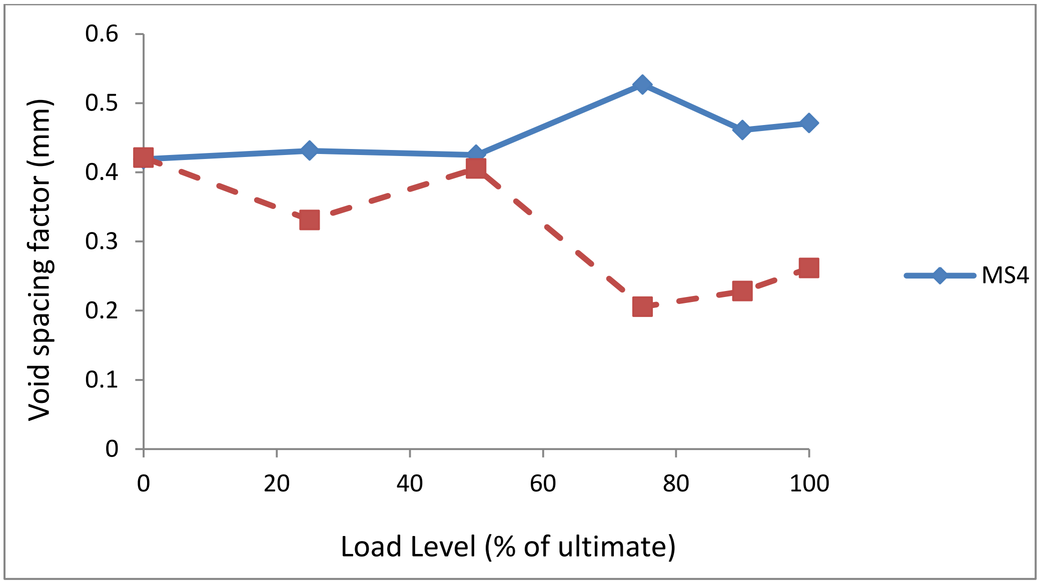

Figure 6.17. Change in Void Spacing Factor with Increase in Stress Level. MS: Plain Mortar, FMS: Fiber Reinforced Mortar (0.25% fiber)

6.4.5. Void Shape Factor

Shape Factor (SF) denotes the ratio of a void's major dimension to its minor dimension. From this definition, the shape factor is a dimensionless value which is affected by void's shape. It describes the void's aspect ratio regardless of its size. Shape factor varies from numbers close to zero for a very elongated object (such as cracks) to near unity for a circular void.

Figure 6.18 compares the amount of voids (expressed as percentage of total voids) with different shape factor values, averaged for different loading levels for plain and fiber reinforced mortars. According to this diagram, there is no significant difference between the average of percentage of voids corresponding to a specific shape factor in both plain and fiber mortars. In other words, inclusion of fibers in mix design does not affect the distribution of shape of voids in cement-based materials.

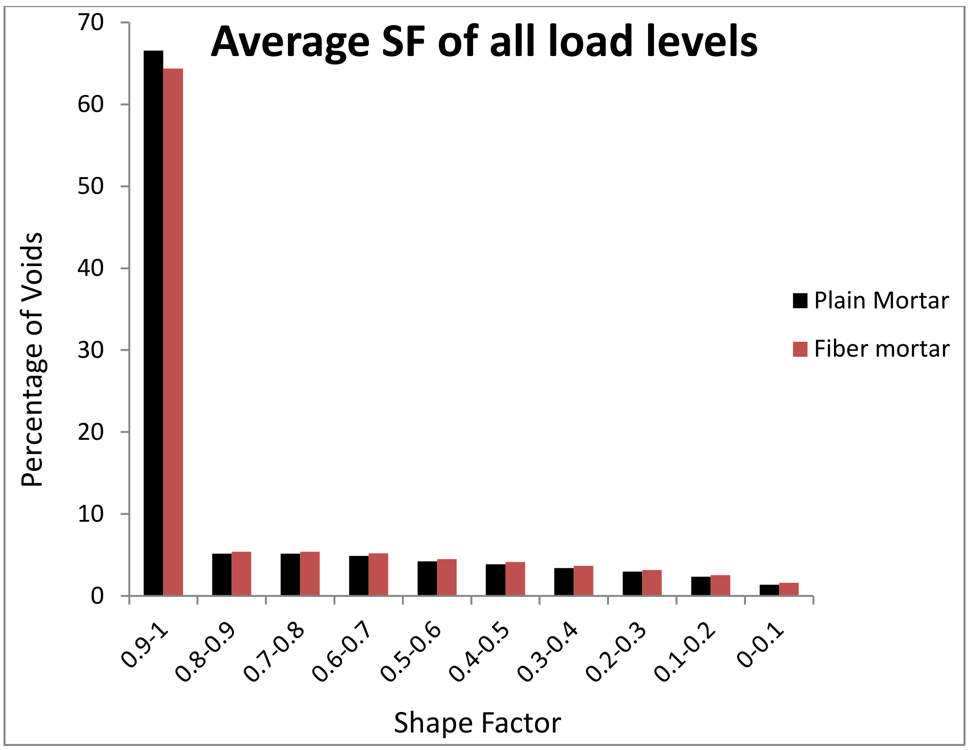

Figure 6.18. Shape Factor Values as the Percentages of Total Voids, Averaged for All Loading Levels

In Figure 6.19, the change in the percentage of the voids with shape factors between 0.9 and 1 at different stress levels for both plain and fiber reinforced mortars have been presented. The figure shows that although the percentage of voids with the shape factor larger than 0.9 at load levels close to ultimate is less than that of corresponding unstressed values, no clear trend in the change of this value is visible neither by increasing the stress nor by incorporating the fibers is observed. Further study is needed to examine the change of shape factor by application of the stress and suitability of X-ray tomography scan method for studying this parameter.

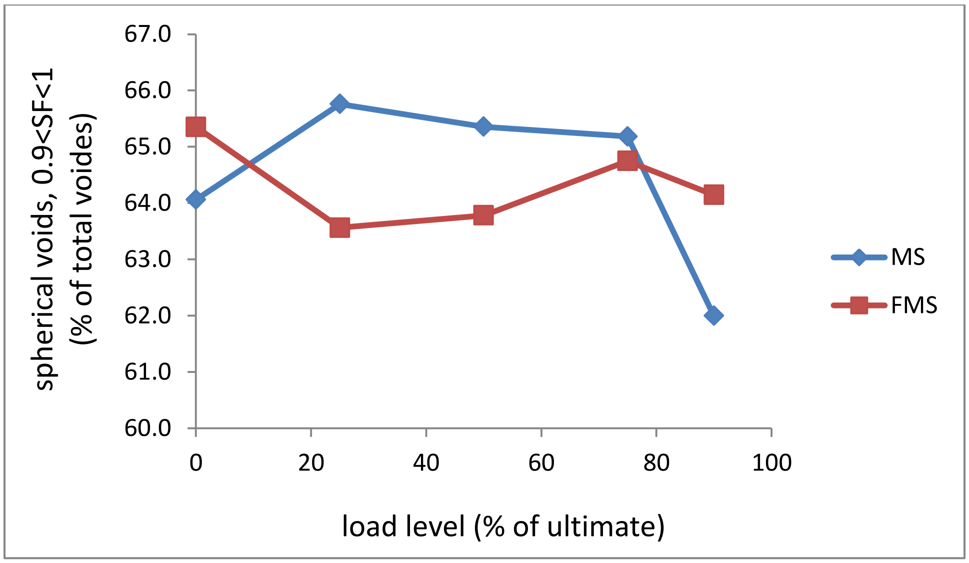

Figure 6.19. Change in Percentage of Spherical Voids (Shape Factor > 0.9) with Increase in Stress

7. Damage Evaluations

7.1. Change of Modulus of Elasticity with Stress

Degradation of the material stiffness properties under loading (i.e. damage) is a complex phenomenon. In the case of scalar damage, the uniaxial stress-strain law for elastic damage may be written in the form of the secant relationship as:

$$\sigma = E_S \, \varepsilon \qquad 7.1$$

Where σ and ε are the nominal values of stress and strain and E_s is the secant stiffness modulus of a damaged material. If damage is defined as the degradation in stiffness properties, the σ/ε ratio will provide a simple damage indicator. Figure 7.1 and Figure 7.2 present how the secant modulus of elasticity of the specimens in this study changes due to the application of stress. The data from compressive stress-strain tests have been used for calculating E at different loading levels.

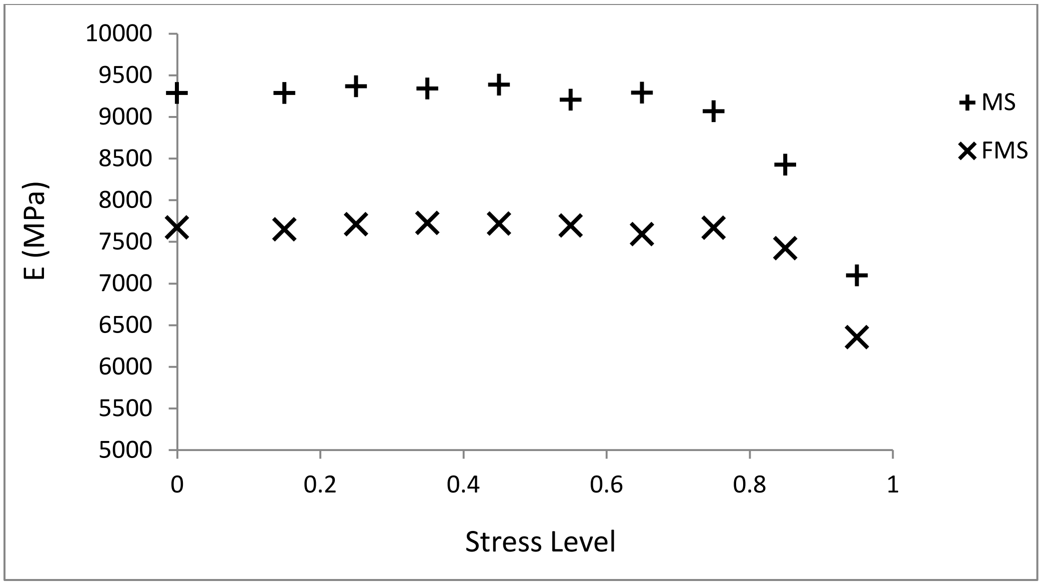

Figure 7.1. Change of Secant Modulus of Elasticity with Stress (Mortar)

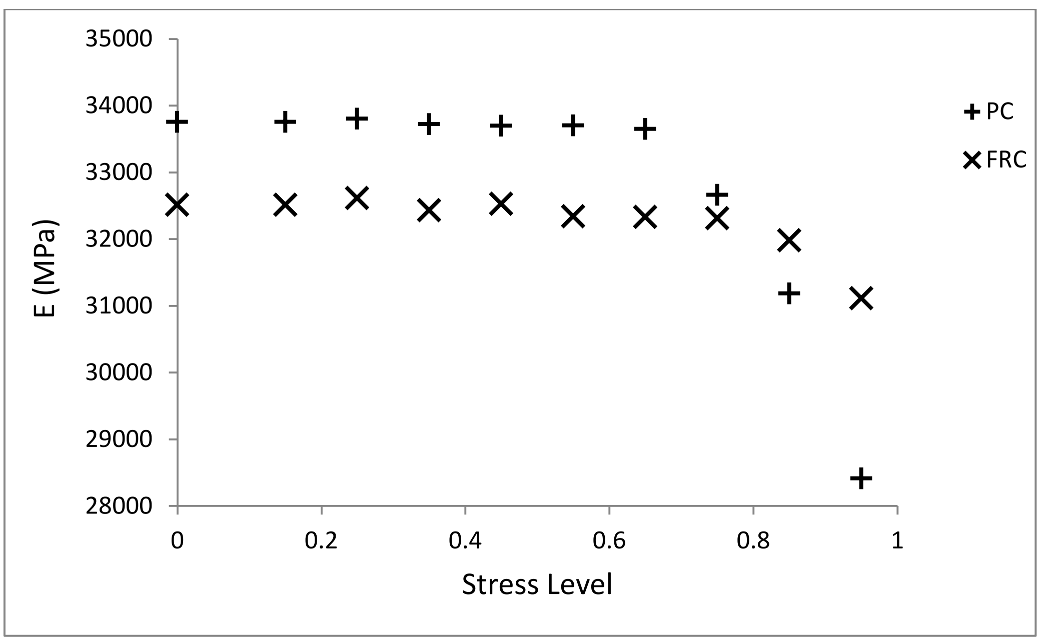

Figure 7.2. Change of Secant Modulus of Elasticity with Stress (Concrete)

7.2. Damage Evaluations Using Secant Modulus of Elasticity

For the isotropic case of damage, the mechanical behavior of microcracks and voids is independent of their orientation and depends only on a scalar variable [115] which can be defined in terms of the ratio between the damaged and undamaged stiffness of a material as:

$$d_E = 1 - \frac{E}{E_0} \qquad 7.2$$

Where:

d_E= Damage value calculated using secant modulus of elasticity;

E: Secant modulus of elasticity in damaged specimen at different loading levels

E_0: Initial modulus of elasticity (undamaged specimen)

In order to calculate d_E, the stress-strain response from the compression test has been used to calculate the damaged and un-damaged moduli of elasticity at different stress levels.

In Figure 7.3 and Figure 7.4, the calculated damage values at each stress level for the mortars and concrete samples are presented.

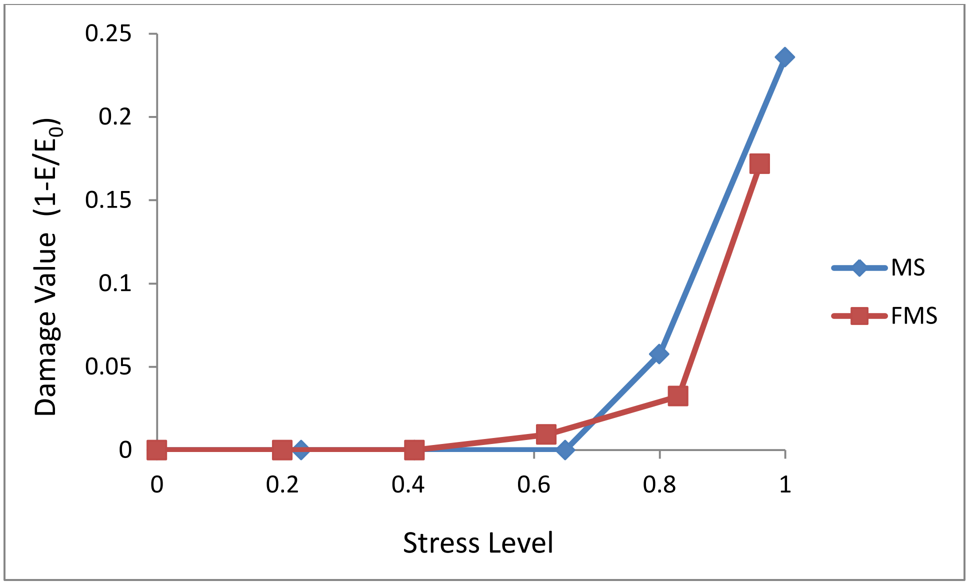

Figure 7.3. Relationship between Increase in Stress Level and Damage Value for Mortar Specimens

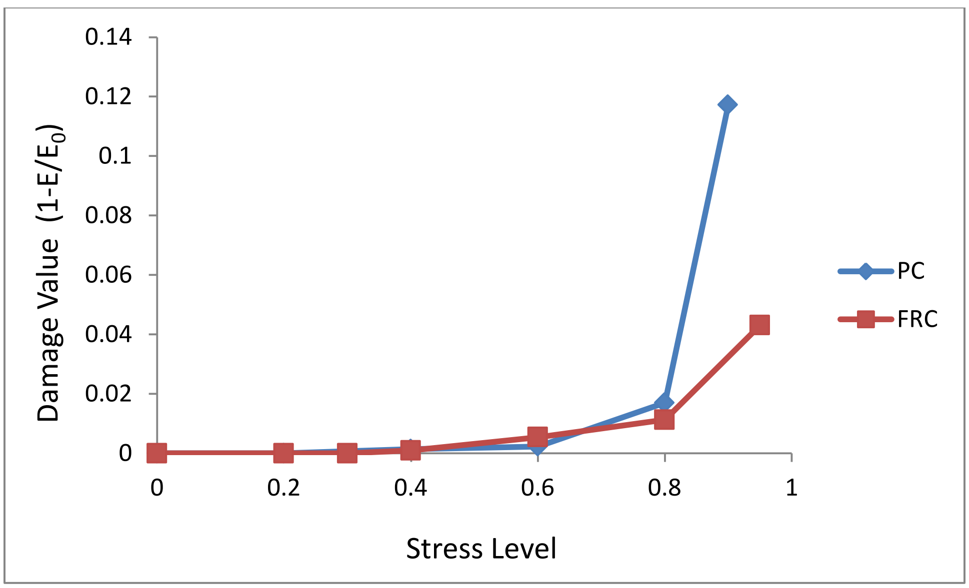

Figure 7.4. Relationship between Increase in Stress Level and Damage Value for Concrete Specimens

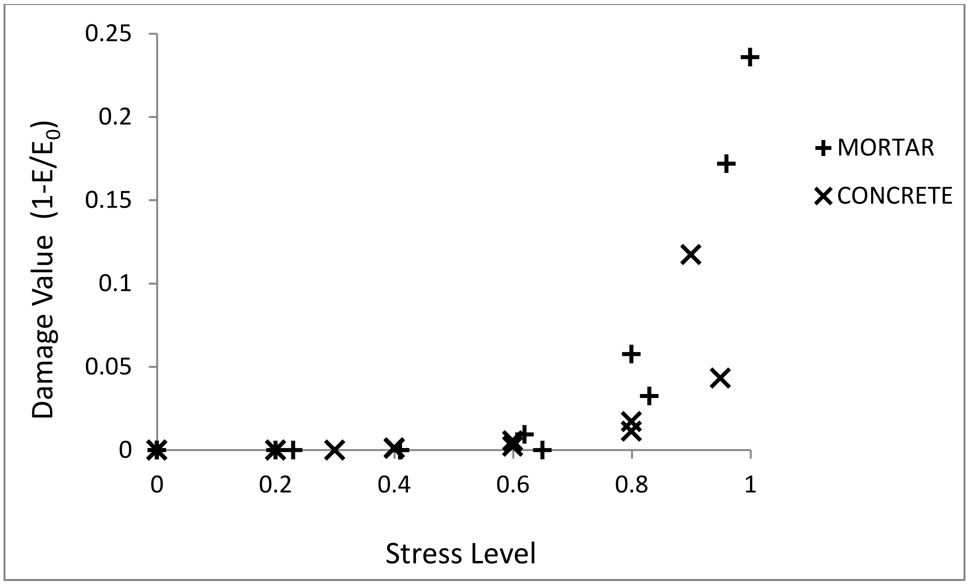

Figure 7.5. Relationship between Increase in Stress Level and Damage Value for all Specimens

According to Figure 7.3 and Figure 7.4, the damage value in specimens containing fiber is less than that of plain specimens at the same level of stress up to about 80% of ultimate. Close to ultimate stress levels, this value in fiber reinforced specimens is about 70% for mortars and 25% of that of plain specimens for concrete. This deviation of calculated damage value of plain and fiber reinforced materials beyond 80% of ultimate stress shows the effectiveness of the fibers in controlling the mechanical induced damage in cement-based materials at high stress levels.

The data presented in Figure 7.3 and Figure 7.4 are plotted together in Figure 7.5. This figure shows that the damage in cement-based materials has two stages. The first stage shows that by increasing the load levels, no damage will occur until a certain level of stress while, in the second stage, an increase in the load level results in an increase in the damage. According to the results presented in Figure 7.5, the stress level at which the damage starts is somewhere approximately at 60 percent of ultimate load.

7.3. Damage Evaluations Using UPV

As seen in Chapter 6, a general trend between an increase in stress level and decrease in UPV exists. A decrease in the UPV was explained through the creation of microcracks and increase in the porosity, while damaging the specimens in higher stress levels. As per Equations 3.1 to 3.3, the modulus of elasticity (E) is proportional to the square of the wave velocity (V), we define another damage value d_V as below to quantify the occurred damage during loading by decreasing the UPV:

$$d_v = 1 - \frac{V^2}{V_0^2} \qquad 7.3$$

Where,

d_v= damage value calculated using UPV;

V= UPV of specimen at each stress level; and

V_0= UPV of each specimen at zero stress.

This expression provides a very simple estimate of damage by means of UPV measurements.

In Figure 7.6, the calculated damage value at each stress level (up to 100% of ultimate) for each mix has been presented. From this figure, it can be seen that there is no clear trend in the variation of the damage value either between mortar and concrete specimens or by incorporating the fibers.

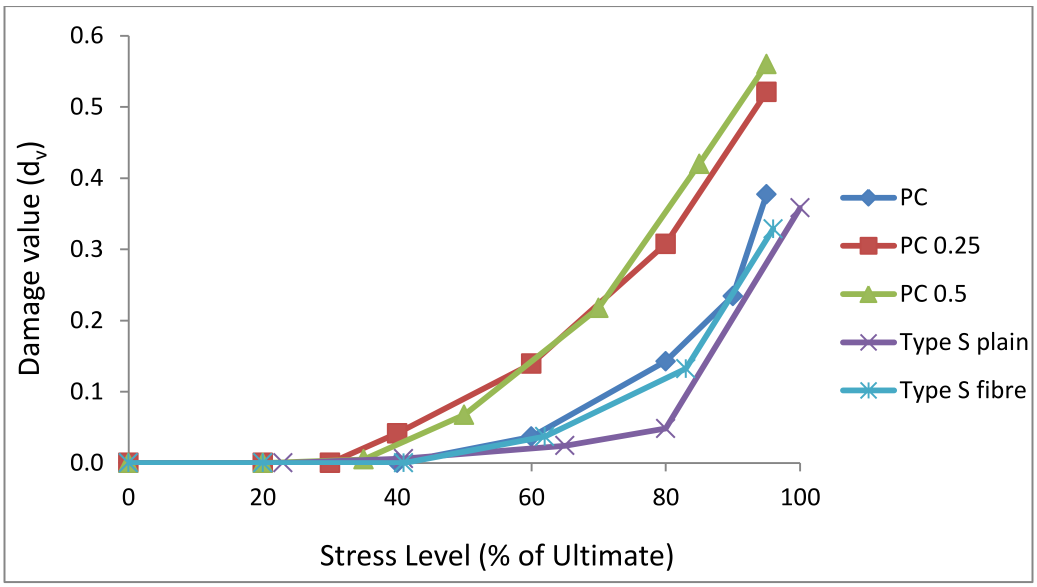

Figure 7.6. Relationship between Increase in Stress Level and Damage Value

Similar to previous section, the damage value presented in Figure 7.6 has two stages. The first stage shows that by increasing the load there is no change in the damage value, and the second stage shows that increasing the load level results in increasing the damage value, as shown in Figure 7.7. This trend is clearly presented in Figure 7.7 by linear regressing on data points of each stage. This behavior is similar to that shown in Figure 6.6. The onset point of damage, which corresponds to a stress level of about 60% of ultimate stress, is also in good agreement with the point of sharp increase in the permeability coefficient found to be at about 60% of ultimate stress in Figure 6.6. This observation lends more support to suggesting a design approach which limits service load stresses to 60% of peak capacity.

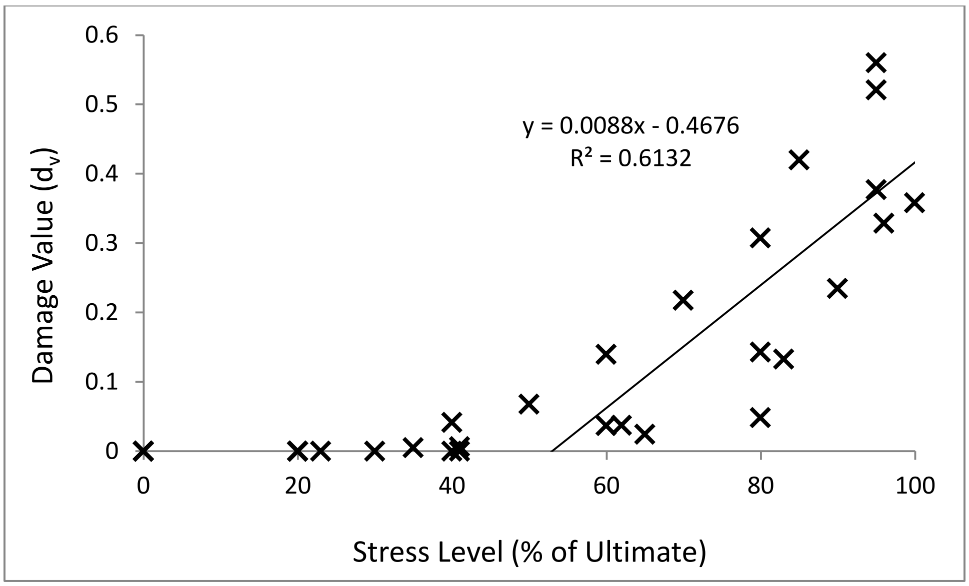

Figure 7.7. Relationship between Stress Level and Damage Value

7.4. Damage-Permeability Relationship

Evolution of permeability with damage in the pre-peak phase of concrete has been shown in Figure 7.8. The damage values presented in this figure are corresponding to calculated values for stresses up to 80% of ultimate stress which permeability measurements has been carried out. This explains lower damage values in this figure compared to the values presented in Figure 7.7. As seen in this figure, an exponential regression was carried out on the data points for all types of mortars and concrete that were studied here. This relationship is similar to the damage-permeability curves found by Choinska et al. [5] and Picandet et al. [42] who also found an exponential trend between damage and gas permeability by defining a damage value from the variation of stiffness (E) of the concrete specimens in loading (see Figure 7.9). However, the range of damage and permeability values and consequently regression equation found in the present study is different from the two mentioned studies. This is likely due to different permeating fluids (water in the present study vs. gas in their study) and loading history (under load in the present study vs. after unloading in their study) employed as indicated in Table 2.1.

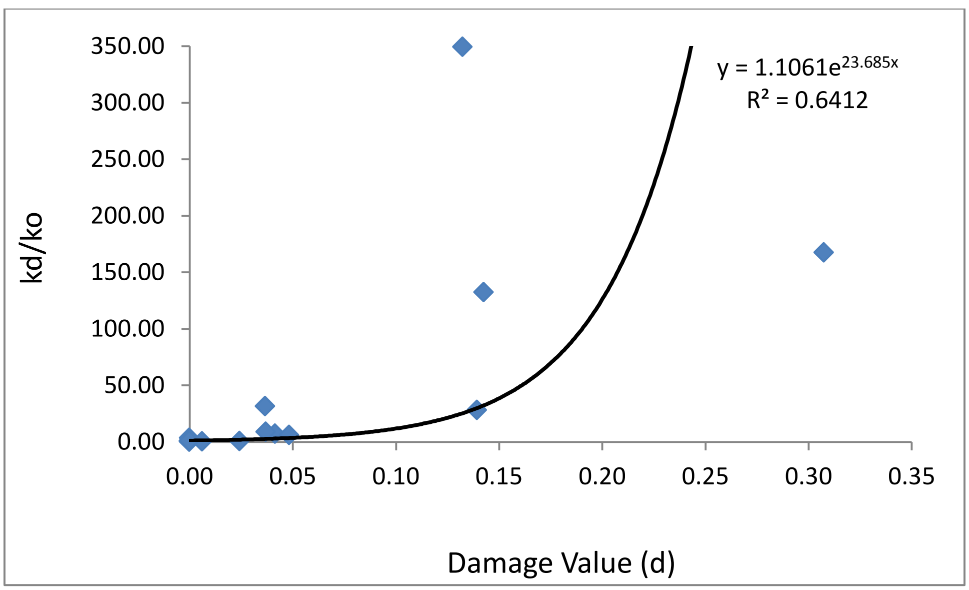

Figure 7.8. Relating Damage to Increase in Permeability (k_0: Permeability at Zero Stress, k_d: Permeability at Different Stress Levels)

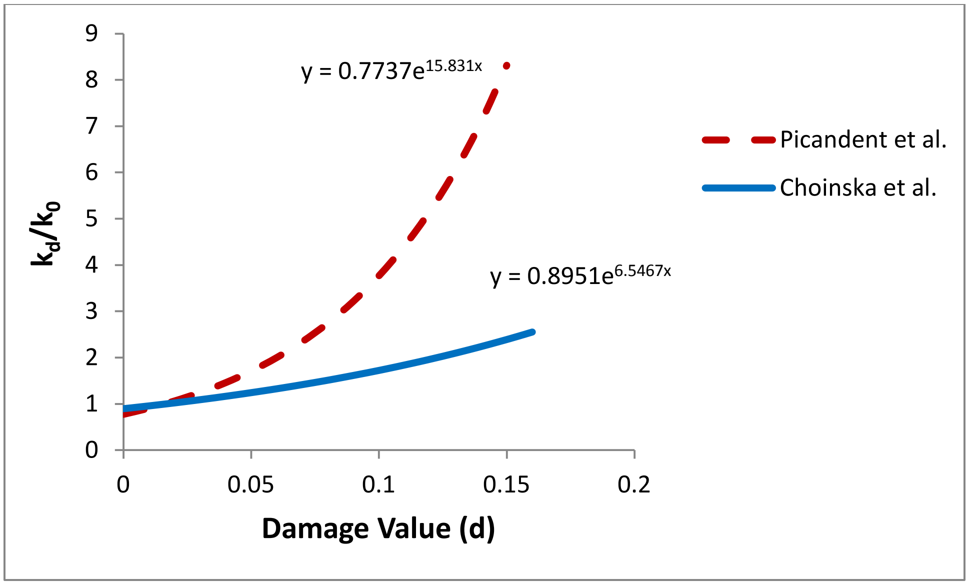

Figure 7.9. Damage-Permeability Relationships Produced from Choinska et al. [5] and Picandet et al. [42]

8. Finding the Number of Connected Pores in Cement-based Materials Using X-Ray Tomography

8.1. Introduction

It is well known that the transport properties of cement-based materials depend mainly on the number, size and connectivity of their pore structure [11, 12]. Progressive cracking during loading also provides a path for water and chlorides to transport through the concrete and reach the reinforcement. Therefore, it is very important to find out how the connectivity of the voids and pores changes with increase in stress.

As stated in Chapter 4, x-ray tomography (XRT) is a very useful tool for microstructure characterization and the study of engineering materials such as cement-based systems. This technique has been applied to unstressed concrete specimens to study defects, voids and reinforcing steels [86-90], effect of sulfate attack [91-93] and cement hydration [94, 95]. In addition, it has been employed to investigate the internal damage in stressed concrete by Landis and associates [90, 101-104].

The latter examined the change in concrete microstructure under stress using the XRT technique. They used the 3D connected component algorithm developed by Franklin [116] to obtain the number of connected components and crack surface area in mortar specimens under a cyclic loading condition. In the next section, the definition for connected components (which they measured in their study) will be described and the difference between this parameter and connected pores (a parameter which is introduced, defined and measured in this study) will be illustrated.

8.2. Connected Components vs. Connected Pores

A connected component is defined as any two vertices that are connected to each other by a path or at least at one point. Figure 8.1 shows a schematic view of an example that contains four connected components.

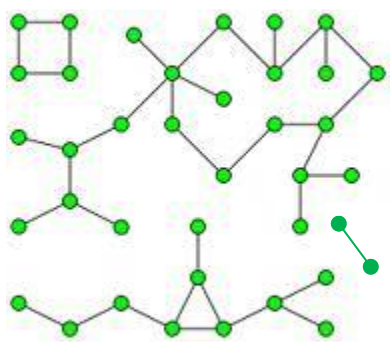

Figure 8.1. Schematic View of an Example of Four Connected Components with 38 Connected Points

The properties and parameters based on the idea of connectedness often involve the word connectivity. For example, in graph theory, a connected graph is one from which we must remove at least one vertex to create a disconnected graph. In other words, the connectivity of a graph is the minimum number of vertices that must be removed to disconnect it. Likewise, 2-dimensional connectivity can be illustrated in regular tiling which is described as the number of accessible neighbors from a single tile. There are two types of connectivity in image processing namely, 4-connectivity and 8-connectivity. In the former, 4-connected pixels are neighbor pixels that share an edge. These pixels may be connected vertically or horizontally. With the latter, 8-connected pixels are neighbor pixels that share one of their edges or corners. These pixels may be connected vertically, horizontally and diagonally. Figure 8.2 illustrates the 4-connectivity and 8-connectivity as defined here.

(a) (b)

Figure 8.2. (a) 4-connectivity and (b) 8-connectivity Definition

On the other hand, connected pores considers the total number of pores which are connected within different components. For example in Figure 8.1, there are 36 pores which are connected together.

As mentioned earlier, Landis et al. [104] used a connected component algorithm to study the change in number of connected cracks and crack surface area using XRT images. This algorithm scans a binary image, pixel-by-pixel, and groups its pixels into components based on the pixel connectivity. In other words, all pixels in a connected component are assigned a unique label and are in some way connected to each other. Finally, the number of these unique labels are counted and returned as the number of connected components. Although Landis and his colleagues [100-103] used XRT images to calculate the change in number of connected components and crack surface area under cyclic loading to study fracture parameters of concrete such as work of loading, strain energy and fracture energy, neither number of connected components nor crack surface area, as illustrated in the following case, can capture the relevant change in pore connectivity under stress and, instead, the number of connected pores should be considered. Moreover, they did not study the effect of different levels of static loading on the aforementioned parameters (i.e. number of connected components and crack surface area).

Consider the illustration in Figure 8.3, wherein the number of connected components and surface area do not increase with an increase in the number of connected pores. This figure illustrates a 12×12=144 pixel binary image in which the white and black pixels represent the solid and void phases, respectively. In this figure, one can easily count the number of total pores (surface area), connected components and connected pores by counting the black pixels. It should be mentioned that in counting the connected components, the 8-connectivity presented in Figure 8.2 has been considered. The results of this calculation have been tabulated and presented in Table 8.1 for all five cases. For example, if Figure 8.3 (a) is assumed as a section of an unstressed concrete specimen, there are a total of 23 pores (black pixel) in which 18 of them are connected. Moreover, 11 components, including discrete pores (black pixels with no connectivity), can be found in this figure. If it is assumed that by increasing the load, the number of connected pores increases, see Figure 8.3 (b, c and d) and the corresponding values in Table 8.1, the number of connected components do not necessarily obey this trend. The extreme case would be that eventually as shown in Figure 8.3 (e), all pores are connected resulting in the number of connected pores to be 144 (total number of pixels) and the number of connected components would be only one.

On the other hand, as illustrated in Figure 8.3 (c and d), there are examples that the connectivity (number of connected pores) may increase without necessarily increasing the total number of pores. This case happens when the existing discrete pores close under effect of stress while simultaneously the new connected pores create.

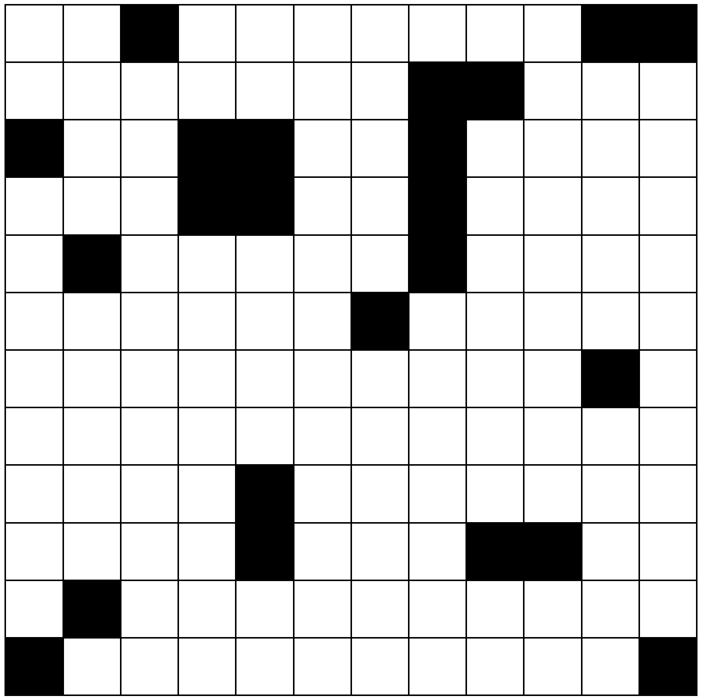

(a)

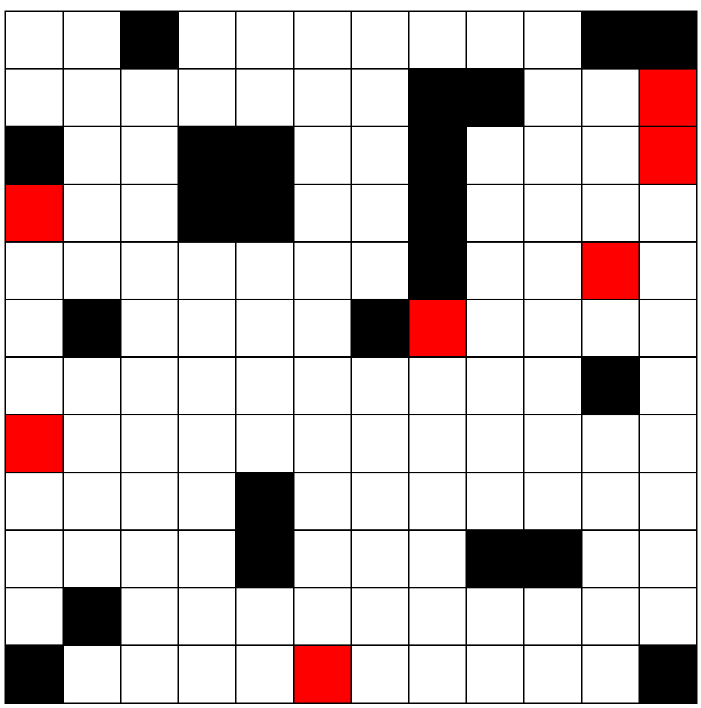

(b)

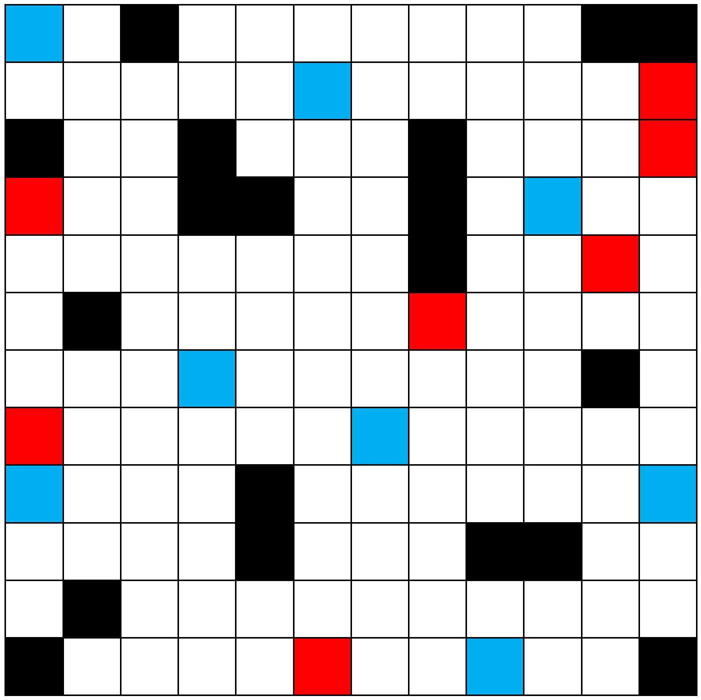

(c)

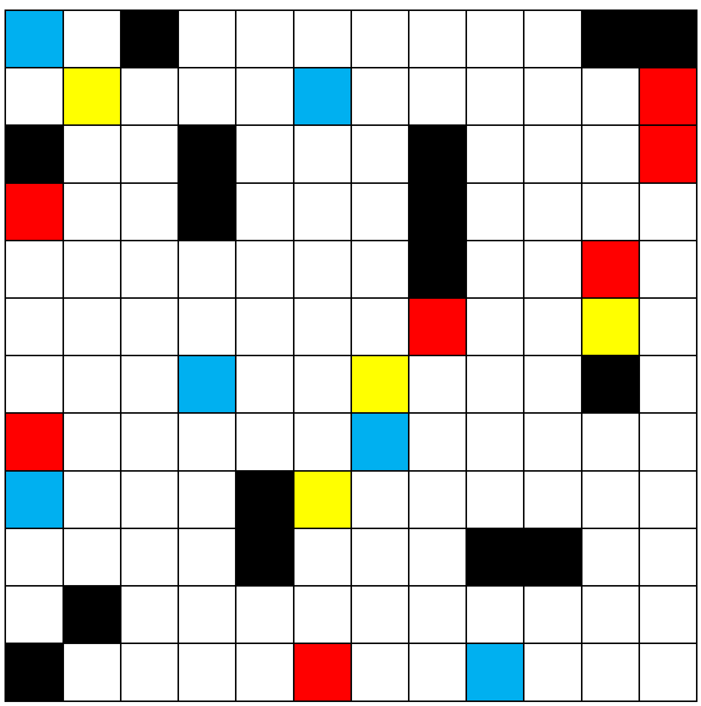

(d)

(e)

Figure 8.3. Illustration of Change in Connected Components and Void Surface Area Compared to Connected Pores

Case (From Figure 8.3)	No. of solid pixels	No. of pores	No. of Components	No. of Connected Components	No. of Connected pores	No. of Discrete pores
a	121	23	11	6	18	5
b	114	30	14	7	23	7
c	110	34	20	9	23	11
d	111	33	12	8	29	4
e	0	144	1	1	144	0

Table 8.1. Number of Total Pores, Components, Connected Components and Connected Pores Illustrated in Figure 8.3 (a,b,c,d,e)

8.3. A Method for Finding the Number of Connected Pores Using XRT Images

As explained before, transport properties of cement-based materials mostly depend on the connectivity of the voids and pores. In this section, a new method to quantify the number of connected pores using XRT images will be presented.

After taking, reconstructing, assigning the threshold value and finally making binary images from XRT images, a Fast Linear-time Connected Component Labeling (FLCCL) algorithm by He et al. [117] was employed for labeling connected components in binary images. This algorithm is a raster-scan type (line-by-line scanning) [118] which has the great advantage that the running time is less dependent on the number of components in an image or their complexity (i.e. shape complexity without being decomposable into meaningful simple parts). The algorithm completes labeling by two raster scans, which is the theoretical lower bond of scans. By the first scan, object pixels are assigned provisional labels, and provisional label dependencies are resolved by a unique set-based analysis together with an efficient equivalent-label-table registration scheme. By the second scan, all provisional labels assigned to each connected component are replaced with a unique label by use of the completed label equivalence table. In this algorithm, the running time is linear against the size of a given image (that is why it is called linear-time). According to He et al. [117] this algorithm is the fastest connected-labeling algorithm available to date (2009). More details about this algorithm can be found in [119] and [117]. In Appendix A, the C++ program developed using this algorithm, which was employed in this study for labeling the connected components, is presented.

This program returns the number of connected components in each image as well as a binary file containing all the labels assigned to each black pixel. By filtering the objects with just one unique label, the number of discrete components (containing only one pixel) can be calculated. By subtracting the number of discrete black pixels from the total number of black pixels, one can calculate the number of connected black pixels (connected pores) in which each object contains at least two connected pores.

As an exercise, this process has been illustrated in Figure 8.4 and Table 8.2. Figure 8.4 shows simple labeled connected components of the case (a) in Figure 8.3. In this figure, the components (pixels) of each object and each discrete pixel have been assigned a unique label (A to K). If the number of labels with only one occurrence in Table 8.2 (5 labels: A, C, F, G and K) are subtracted from the total number of black pixels (23), the result (23-5=18) would be the number of connected pores.

The above example is a very simple case which does not require much calculation but in the case of XRT images analyzed in this study, an excel program was developed to automatically perform all the required filtrations and calculations.

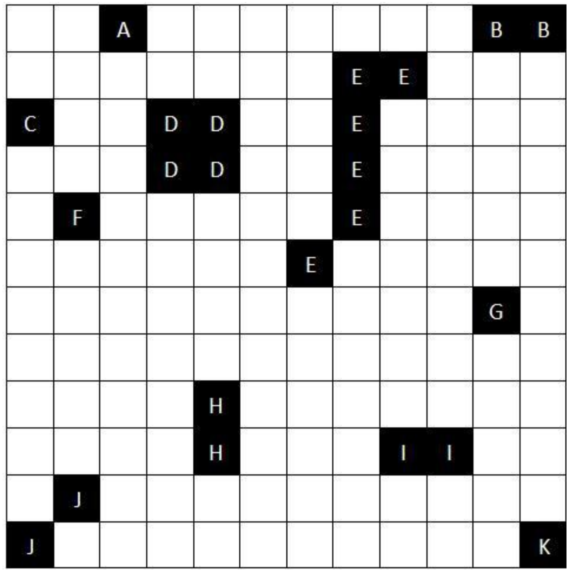

Figure 8.4. Example of Connected Components Final Labeling for Case (a) in Figure 8.3

Black Pixel #	**Label**
1	A
2	B
3	B
4	E
5	E
6	C
7	D
8	D
9	E
10	D
11	D
12	E
13	F
14	E
15	E
16	G
17	H
18	H
19	I
20	I
21	J
22	J
23	K

Table 8.2. Example of Assigned Labels to Each Black Pixel in Figure 8.4

8.4. Results

8.4.1. Number of Connected Components

Table 8.3 and Figure 8.5 present the change in the number of connected components under different load levels for both plain and fiber reinforced mortars. Each data point is the average of three different sections in the height of the specimen. The presented data has been normalized for an 18 mm × 18 mm cross section area.

Number of Connected Components			
Load Level	**Plain Mortar**	**Load Level**	**Fiber Mortar**
0	134895	0	117199
0.18	129115	0.24	133387
0.37	133020	0.47	118455
0.54	128191	0.68	89422
0.73	117949	0.88	68594
0.87	133559	1	90631

Table 8.3. Number of Connected Components in Plain and Fiber Reinforced Mortar under Different Loading Levels

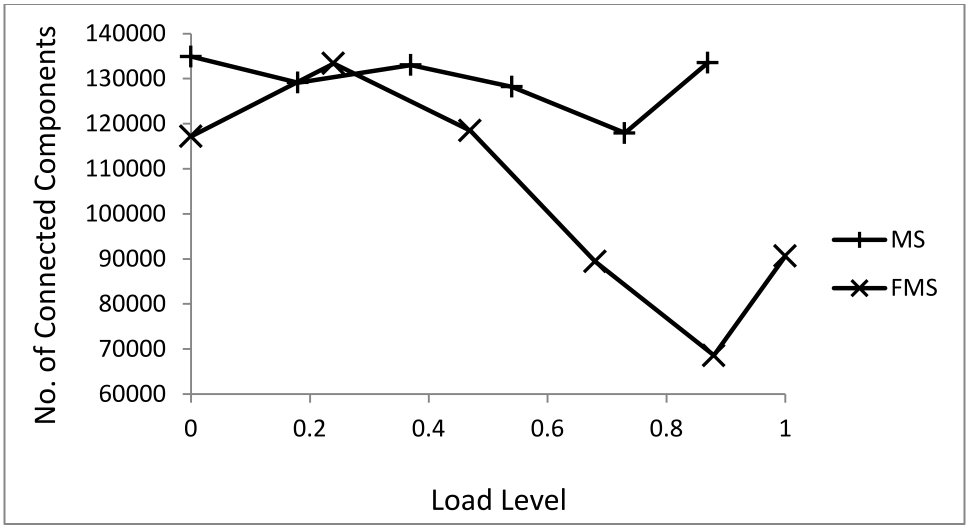

Figure 8.5. Change in Number of Connected Components by Increasing the Load Level

As can be seen in Figure 8.5, there is no clear trend for change in the number of connected components by increasing the load, and this was true for both plain and fiber reinforced mortars.

8.4.2. Number of Connected Pores

Table 8.4 and Table 8.5 present the calculated number of connected pores for plain and fiber reinforced mortar specimens. Each data point is the average of five different sections in the height of each specimen with the corresponding standard deviation (STDEV) shown alongside. The presented data has been normalized for an 18 mm × 18 mm cross section area. In Appendix B, the images in which were processed for the purpose of calculating the change in the number of connected pores have been presented.

Load Level	Plain Mortar (MS)	
	No. of Connected Pores	STDEV (%)
0	351293	1.9
0.18	370342	1.8
0.39	416142	2.2
0.62	489044	1.9
0.88	783110	2.6

Table 8.4. Number of Connected Pores and Relative Standard Deviation Calculated for two Plain Mortar Type S Samples (Each Data is the Average of Five Sections in the Specimen)

Load Level	Fiber Reinforced Mortar (FMS)	
	No. of Connected Pores	STDEV (%)
0	280887	1.7
0.24	286176	2.3
0.44	338034	2.1
0.64	435643	2.9
0.85	601839	3.2
1	871456	4.1

Table 8.5. Number of Connected Pores and Relative Standard Deviation Calculated for two Fiber Mortar Type S Samples (Each Data is the Average of Five Sections in the Specimen)

The average values corresponding to the ratio of the number of connected pores to the number of total pores (in percent) for each mix have been calculated and plotted in Figure 8.6 (a). The figure shows that by increasing the stress, the ratio of connected pores also increases. While at the unstressed condition only about 45 percent of the pores are connected to at least one neighborhood pore and about 55 percent of the pores are discrete, at about 90 percent of ultimate stress, more than 80 percent of the pores have at least one connectivity. It is interesting to note how the percentage of connected pores varies through the course of test.

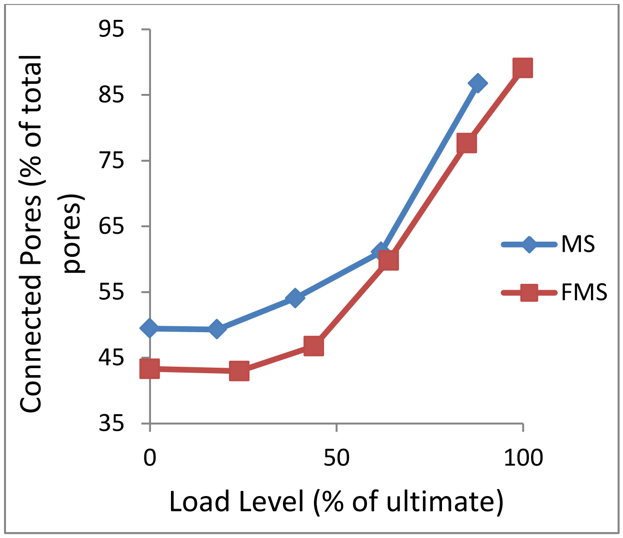

(a)

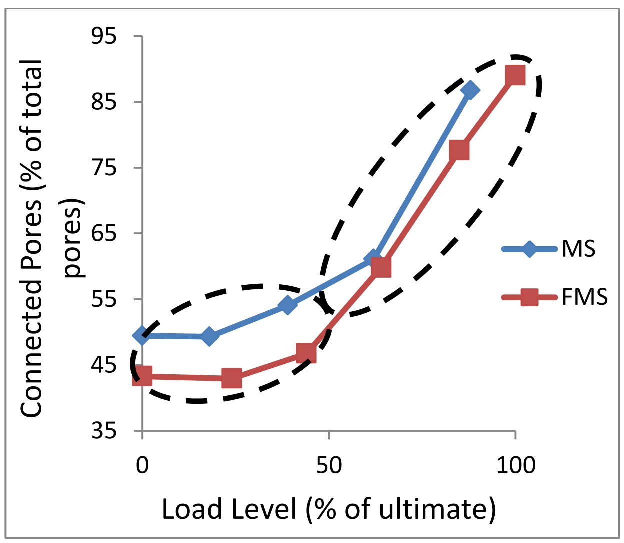

(b)

Figure 8.6. (a) Change in Connectivity Level by Increasing Stress Level (b) Two-stage Representation

For both mixes, as shown in Figure 8.6 (b), we can recognize two stages of connectivity level (number of connected pores) change: the initial stage in which there is a small change in connectivity level and the second stage in which the connectivity level increases at a sharper rate. It is likely that the first stage is due to formation of new microcracks (mainly in aggregate-paste interface) and the second stage is due to crack propagation (mainly in the bulk of cement paste), which causes a more rapid increase in connectivity. This observed behavior in changing the connectivity level supports the permeability results obtained through experimental programs in Chapter 6. Figure 8.6 also illustrates that the connectivity level in fiber reinforced mortars is always less than that of plain mortars under the same stress level. This finding again confirms the positive effects of using fibers in improving the durability of concrete in service conditions which were presented in previous chapters and reported by [22, 37].

8.4.3. Connected Porosity

For quantifying the pore connectivity in a specimen, a new parameter called "Connected Porosity" has been introduced. We define this parameter as the percentage of the pores which are connected to at least one neighborhood pore and it is calculated as:

$$\phi_c = \text{Total Porosity} \times \text{Connected Pores} \qquad 8.1$$

Where, the total porosity (%) and connected pores (%) values have been presented in Figure 6.11 and Figure 8.6, respectively. One should notice that in calculating the connected porosity at different stress levels using the above definition, the total porosity is constantly updated with the increase in applied compressive stress. Therefore, the updated values of total porosity and connected pores (as the percentage of the total pores) should be used for calculating connected porosity at each stress level.

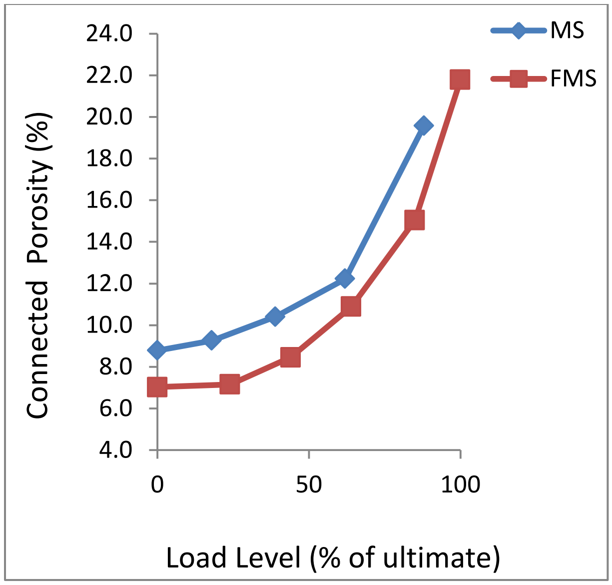

(a)

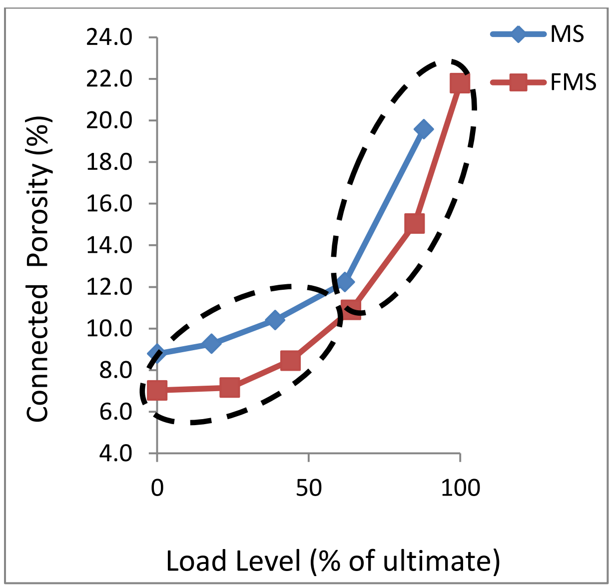

(b)

Figure 8.7. (a) Change of Connected Porosity with Stress (b) Two-stage Representation

The values of connected porosity have been calculated and illustrated in Figure 8.7. According to this figure, the connected porosity increases due to the application of stress. The figure also shows that fiber reinforced mortars always have a lower connected porosity at all stress levels compared to the plain mortars. Further, as the load increased from 0 to 90 percent of ultimate, the connected porosity changed from 8.8% to 19.6%, and from 7% to about 15% for the plain and fiber reinforced mortars. These changes correspond to a 114-122% increase in connected porosity of the studied specimens. Compare this number with the less-than-30-percent increase in total porosity when elevating the load from 0 to 90 percent of ultimate (as presented in Figure 6.11). It can thus be concluded that the application of stress increases the *connected* porosity at a much faster rate compared to its effect on the *total* porosity. In other words, the processes of propagation and interconnectivity of the existing pores are more dominant than the creation of new discrete voids, especially under stress.

The connected porosity values presented in Figure 8.7 show that even at stress levels close to ultimate and in the worst case, only less than 20 percent of the specimen is occupied by the connected voids while the rest is occupied by either discrete pores or solids. This quantified result, indirectly showcases the significance of creating a single (or at most, very few) large crack(s) leading up to failure of the specimen under compression.

9. Relating Connectivity to Transport Properties in Mortar Specimens

In Chapters 6 and 8, the change in a variety of different microstructural parameters such as total porosity, void specific surface area, void spacing factor, shape factor and connected porosity, as a result of applied stress were presented and discussed in details. Moreover, in Chapters 6 and 7, along with illustrating the variation of permeability, the UPV and the modulus of elasticity, it was demonstrated how the mechanical stress induced damage is related to a change in these three parameters under the simultaneous effect of compressive strength. Although the results of the tests presented in Chapters 6 through 8 provide valuable information about the changes in mortar properties under stress at the macro level, they do not show how these changes are related to the microstructure of the mortar specimens. In this chapter it is attempted to show how permeability, UPV and damage are linked to both total and connected porosity measured by the application of x-ray tomography technique.

9.1. Permeability- Porosity Relationship

Figure 9.1 and Figure 9.2 illustrate the relationship between permeability of plain and fiber reinforced mortars with the total and connected porosity, respectively. These figures show almost similar exponential trends of changing the permeability by changing the corresponding porosity values. This means that at low porosities (total or connected), increasing the porosity does not change the permeability very much but at higher porosity value (corresponding to higher stress values), small increases in porosity values result in a very sharp increase in the corresponding permeability value.

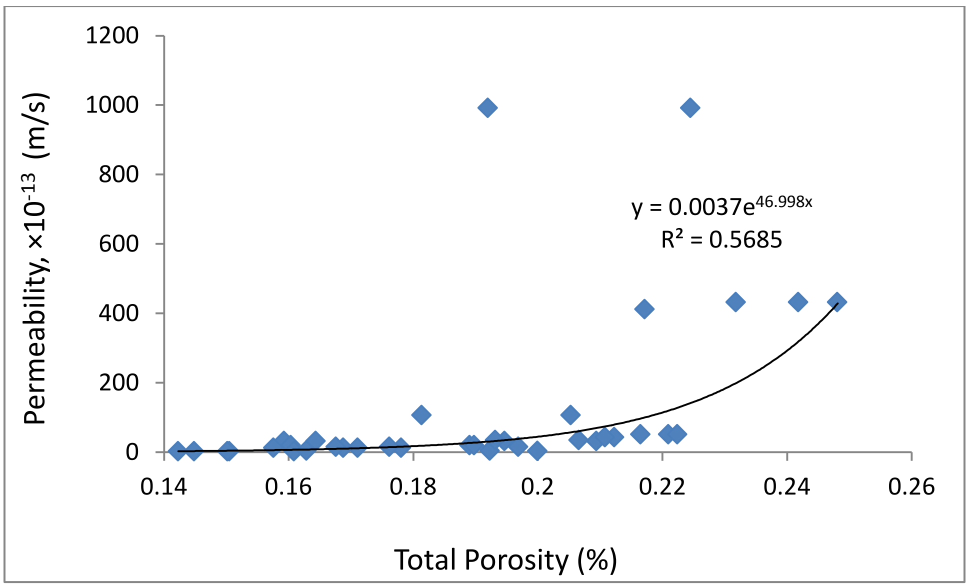

Figure 9.1. Variation of Permeability of Mortar (Plain and Fiber Reinforced) with Total Porosity

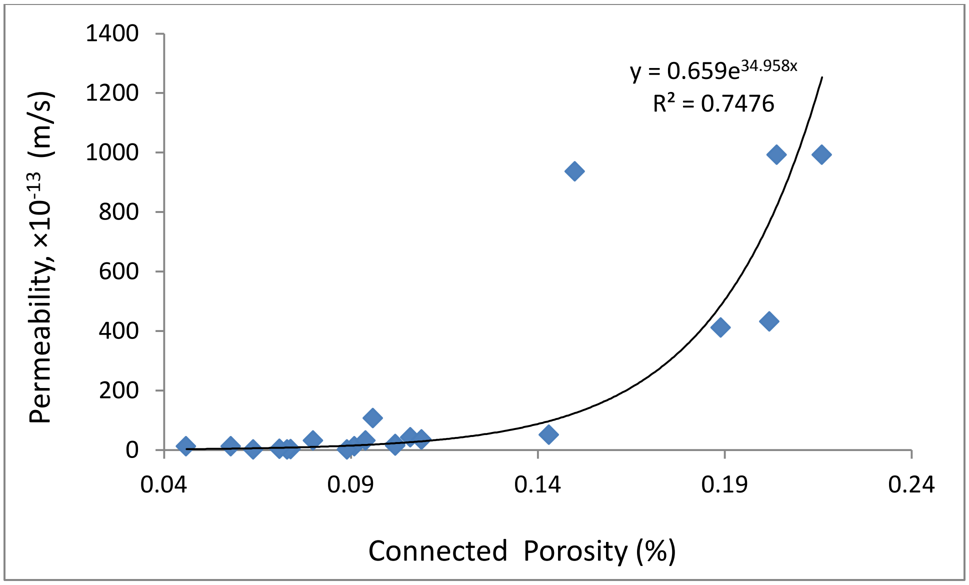

Figure 9.2. Variation of Permeability of Mortars (Plain and Fiber Reinforced) with Connected Porosity

From Figure 9.1 and Figure 9.2, it can be seen that the permeability coefficients have a better correlation with connected porosity rather than the total porosity as this parameter deals with the percentages of connected voids which directly affect the permeability. It should be noted that in defining connected porosity (in Section 8.4.3), the voids with as low as two connected pores have been considered in the connectivity calculations which may not necessarily represent the connectivity from one side to the other side of the specimen. Nevertheless, connected porosity is able to predict the permeability of the mortars with a higher coefficient of determination than the total porosity.

The effect of using the connected porosity in increasing the accuracy of the prediction of the water permeability is more pronounced in Figure 9.3 and Figure 9.4 which show the change of normalized permeability values versus normalized total and connected porosity, respectively. In these figures, the parameters K_0, ϕ_{t0} and ϕ_{c0} represent in order, the permeability, total porosity and connected porosity of specimens in unloaded conditions. The figures clearly show that the change of connected porosity has a better correlation with the change of permeability with the coefficients of determination of 60% more compared to the total porosity.

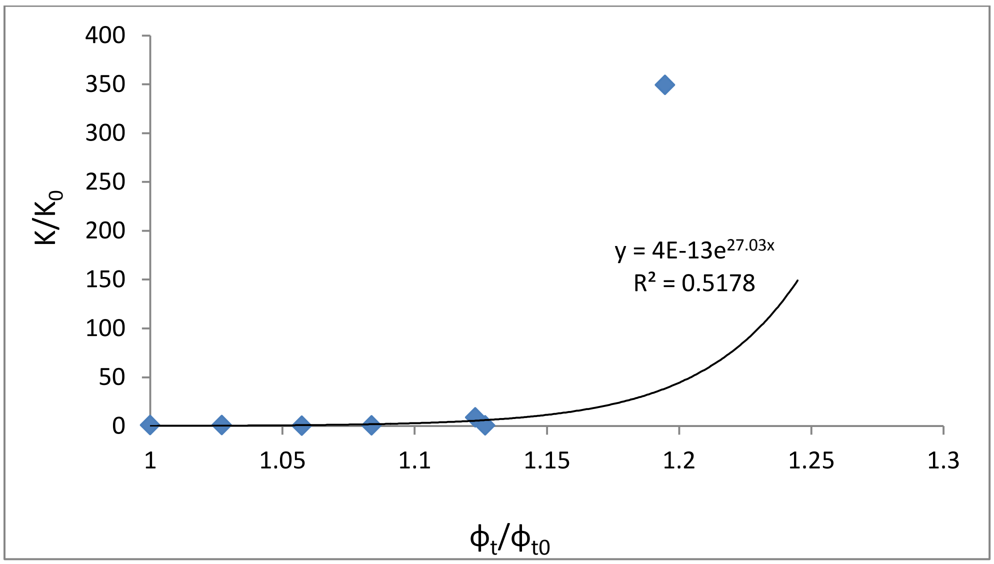

Figure 9.3. Normalized Permeability vs. Normalized Total Porosity of Mortar Specimens (Average Values for Plain and Fiber Reinforced Mortar)

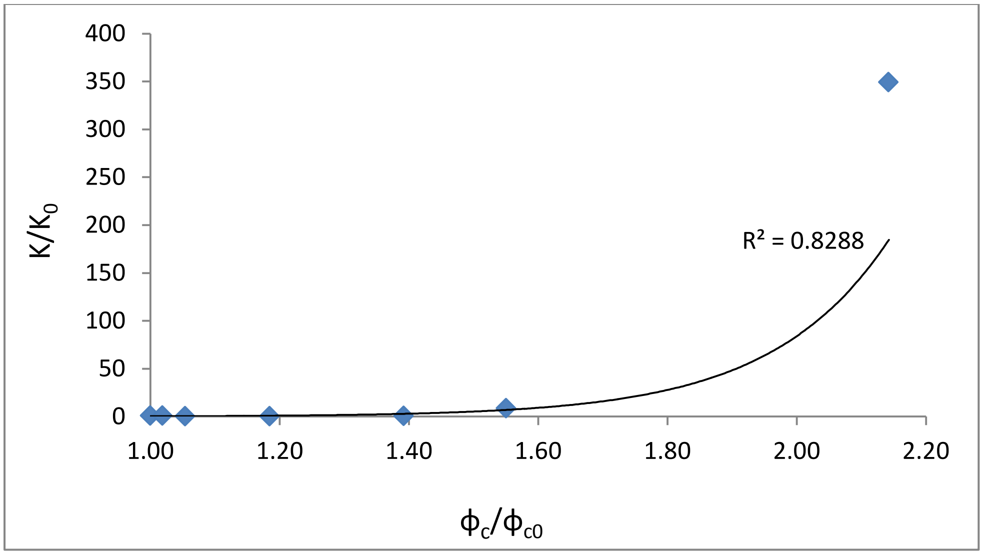

Figure 9.4. Normalized Permeability vs. Normalized Connected Porosity of Mortar Specimens (Average Values for Plain and Fiber Reinforced Mortar)

9.2. UPV-Porosity Relationship

Figure 9.5 and Figure 9.6 illustrate the relationship between Ultrasonic Pulse Velocity (UPV) of plain and fiber reinforced mortars and the total and connected porosity, respectively.

From these figures it can be seen that the UPV values have a slightly better correlation with connected porosity than the total porosity. Although the results show that the UPV depends not only on the amount of the pores and voids in cement-based materials but also on their interconnectivity, the connectivity is not as much effective on UPV as it is on permeability predictions.

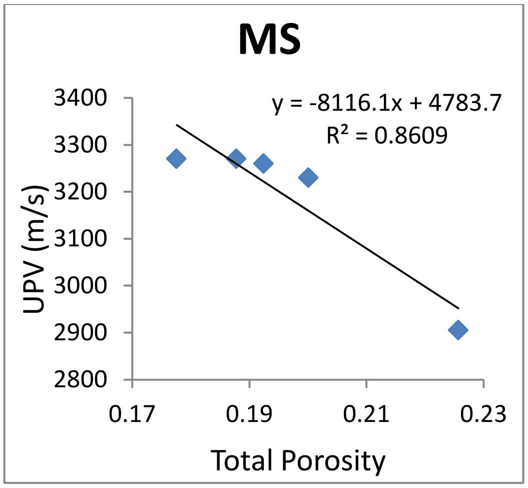

(a)

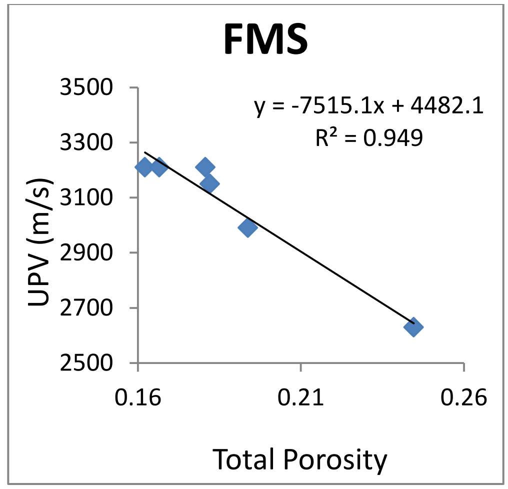

(b)

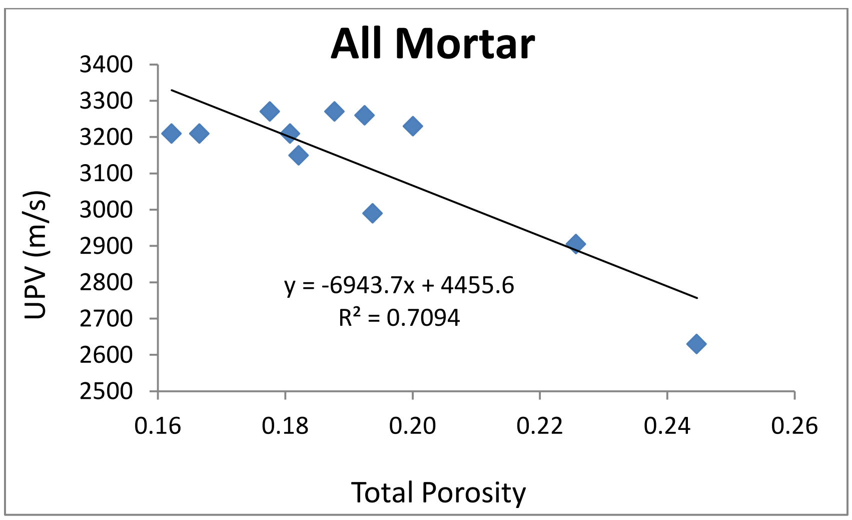

(c)

Figure 9.5. Variation of UPV of Mortars with Total Porosity (a) Plain Mortar, (b) Fiber Reinforced Mortar, (c) All the Mortar Data

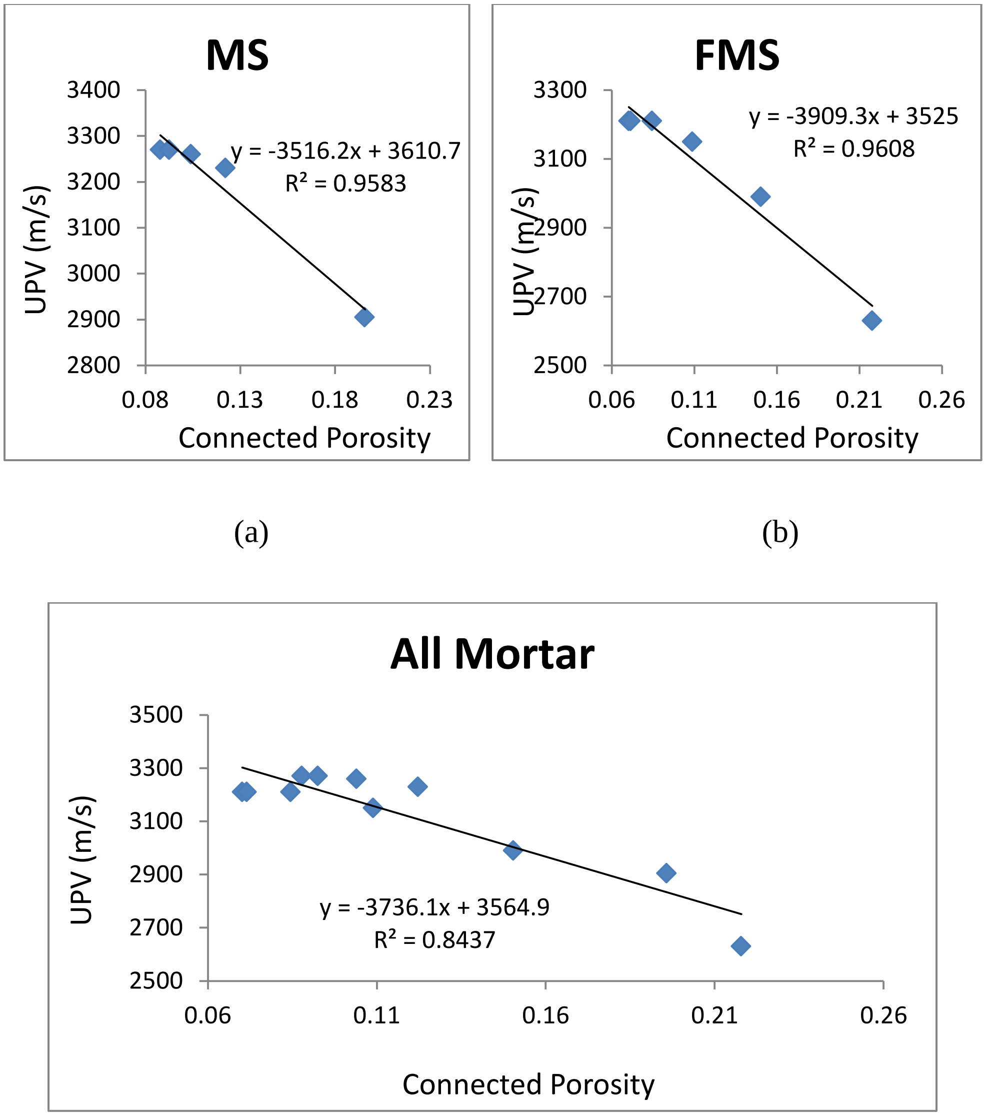

(a) (b)

(c)

Figure 9.6. Variation of UPV of Mortars with Connected Porosity (a) Plain Mortar, (b) Fiber Reinforced Mortar, (c) All the Mortar Data

The sensitivity of the accuracy of expressing the change of UPV with connected porosity compared to total porosity is better illustrated in Figure 9.7 and Figure 9.8. In these figures ϕ_0, ϕ_{c0} and V_0 are the total porosity, connected porosity, and UPV in unloaded specimens, respectively. The figures clearly show that by plotting the change of UPV versus connected porosity, the correlations' coefficients of determination almost remain the same. In other words, the ultrasonic wave velocities in materials depend mainly on the amount of the total voids which affect the density and modulus of elasticity of the material and are independent of the void connectivity.

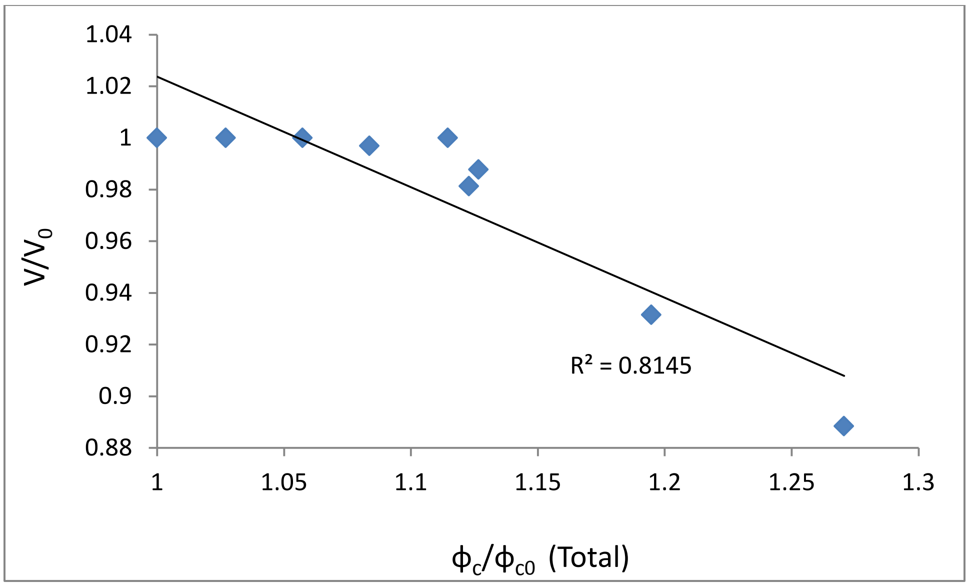

Figure 9.7. Normalized UPV vs. Normalized Total Porosity of Mortar Specimens

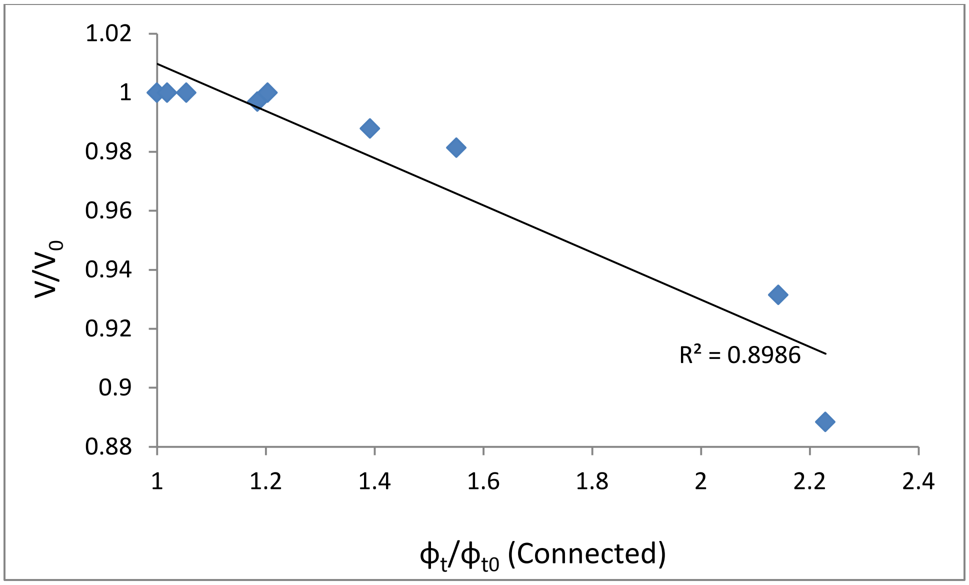

Figure 9.8. Normalized UPV vs. Normalized Total Porosity of Mortar Specimens

9.3. Damage-Porosity Relationship

As seen in Chapter 6 the decrease in UPV was explained through the creation of microcracks and an increase in porosity while damaging the specimens in higher stress levels. Moreover, in Chapter 7, a general trend between an increase in stress level and the defined damage value was found. For a cement-based material under compression, the damage starts with the creation of microcracks at lower loading levels and increases with the creation of larger cracks from the propagation and interconnecting of the small cracks at higher stress values.

In this section, the change of damage value calculated using UPV values as defined in Chapter 7 by Equation 7.3, with total and connected porosity will be examined to see how the interconnectivity affects the measured damage values.

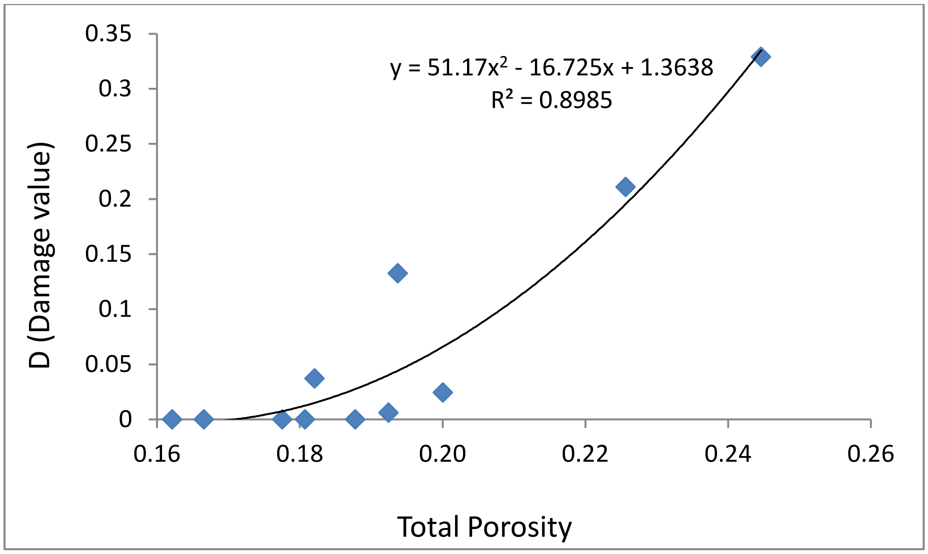

Figure 9.9. Variation of Damage Value by Change in Total Porosity for Both Plain and Fiber Reinforced Mortars

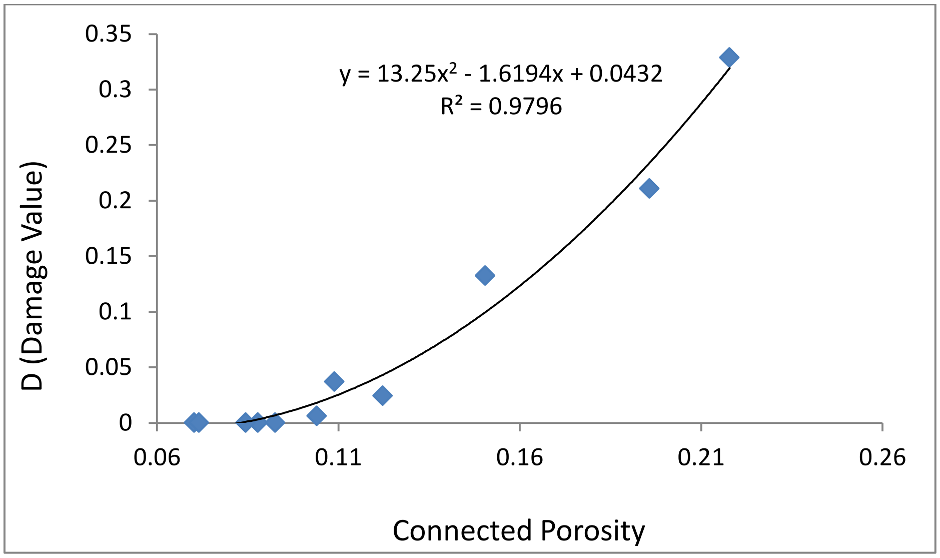

Figure 9.10. Variation of Damage Value by Change in Connected Porosity for both Plain and Fiber Reinforced Mortars

Figure 9.9 and Figure 9.10 present the change of the damage value with change in the total and connected porosity, respectively. The figures show that the damage value increases due to an increase in both total and connected porosity with almost a similar trend. That is, at lower values of porosity (total or connected) there is no significant amount of damage in the specimens while at higher porosity values the damage sharply increases. This trend is very similar to the plots of Figure 7.5 and Figure 7.7. The figures also show that there exists a better correlation between the damage value and the connected porosity than with the total porosity. Thus, damage value seems to be a more suitable parameter to characterize the real behavior of the mortars under compression stress as it is more related to the increase in connectivity rather than just an increase in the voids. Therefore, one may conclude that the simple estimate of damage by means of ultrasonic velocity measurements provides good information about the pore interconnectivity of the cement-based material under stress.

9.4. Hudson Micro-crack Model

As seen previously in Section 9.2, the presence of microcracks in a medium results in a significant reduction in the ultrasonic wave velocities. This change in wave velocity depends on the size, orientation and distribution of the cracks. Hudson [120] derived the overall elastic parameters and speeds of waves in materials containing cracks of different distribution and density. According to his model, the longitudinal wave velocity in a material with randomly oriented cracks is obtained as:

$$\frac{V^2}{V_0^2} = 1 - 2(1 - 2\nu_0)n\frac{a^3\left[2\,U_{11} + \frac{(3 - 2\nu_0 + 7\nu_0^2)U_{33}}{(1 - 2\nu_0)^2}\right]}{15(1 - \nu_0)} \qquad 9.1$$

Where:

V: longitudinal wave velocity of cracked concrete

V_0: longitudinal wave velocity in the absence of cracks

ν_0: Poissions's ratio of uncracked material

n: number of cracks per unit volume

a: mean radius of the cracks

and:

$$U_{11} = \frac{16\,(1 - \nu_0)}{3} \qquad 9.2$$

$$U_{33} = \frac{8\,(1 - \nu_0)}{3} \qquad 9.3$$

Since all the parameters (except na^3) in Equation 9.1 depend on ν_0, this equation can be simplified as:

$$\frac{V^2}{V_0^2} = 1 - A\,(na^3) \qquad 9.4$$

Where:

$$A = \frac{2(1-\nu_0)}{15(1-\nu_0)}\left[2U_{11} + \frac{(3-2\nu_0+7\nu_0^2)U_{33}}{(1-2\nu_0)^2}\right] \qquad 9.5$$

or:

$$1 - \frac{V^2}{V_0^2} = A\,(na^3) \qquad 9.6$$

From our definition of damage value in Chapter 7:

$$D = 1 - \frac{V^2}{V_0^2} \qquad 9.7$$

Therefore:

$$D = A(na^3) \tag{9.8}$$

Equation 9.8 shows the general relationship between the damage and a measure of the crack distribution density.

For cement-based mortars by assuming ν_0=0.2, parameter A would be: A=2.55. Therefore,

$$D=2.55\,(na^3) \tag{9.9}$$

On the other hand, since parameters “n” and “a” define the number of cracks per unit volume and the mean radius of the crack, respectively, the term “ na^3” may be considered as the volume of the cracks per unit area, which as per the assumption made in Section 5.3.4 is nothing but the porosity.

By considering just the second stage of the Damage-Porosity plots of Figure 9.9 and Figure 9.10, which corresponds to the stage of start and propagation of the damage, the plots of Figure 9.9 and Figure 9.10 might be presented as Figure 9.11 and Figure 9.12.

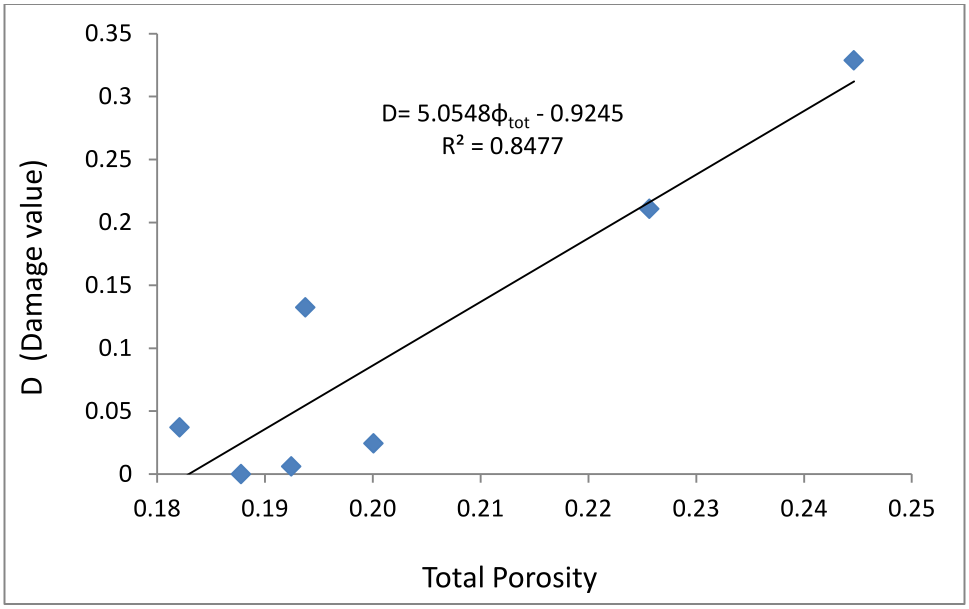

Figure 9.11. Damage-Total Porosity Relationship (Data Corresponding to the Second Stage of Damage-Porosity Behavior)

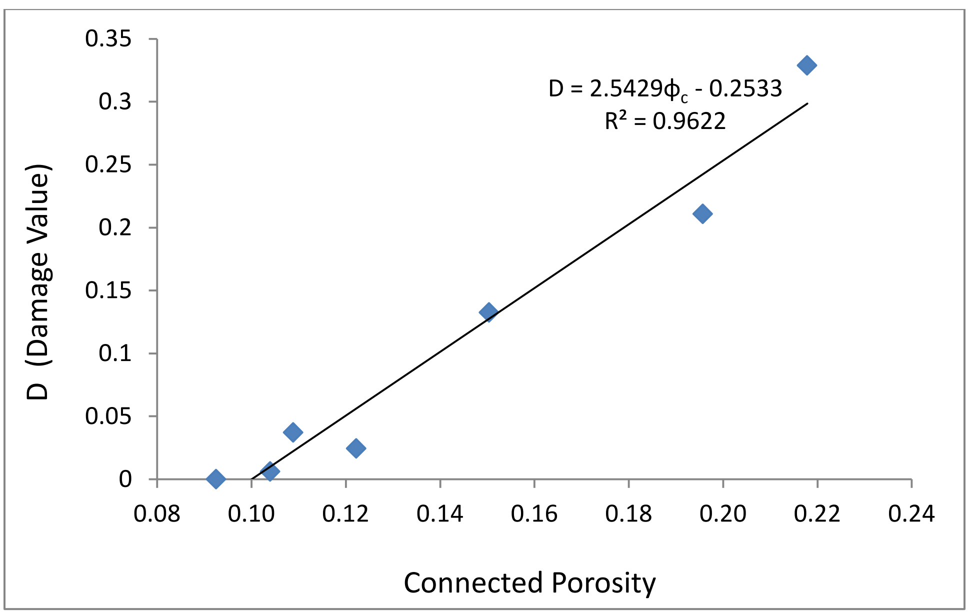

Figure 9.12. Damage-Connected Porosity Relationship (Data Corresponding to the Second Stage of Damage-Porosity Behavior)

The figures depict that the best linear fit is obtained when the damage is expressed as a function of the connected porosity in which according to the linear equation found by regression analysis in Figure 9.12, the coefficient of the connected porosity would be 2.54 which is very close to the value of 2.55 indicated in Equation 9.9.

It should be noted that Hudson's microcrack model is based on the assumption of randomness for the orientation of microcracks which might be reasonable for the concrete under no stress. Although, under uniaxial compressive stress, the microcracks show some degree of preferred orientation which in turn, will cause further anisotropy in the concrete properties, the above results show that Hudson's model may still be valid for cracked concrete. As explained in Chapter 6, the initial increase in the UPV in uniaxially loaded concrete specimens can be attributed to the gradual closing of the microcracks in low levels of stress. However, a further increase in the applied pressure leads to the development of new microcracks. This will cause a decrease in the elastic properties and consequently a decrease in the wave velocities. By measuring the changes in the UPV, one can obtain information about the stress level, the state of cracking and internal damage in materials.

10.Relationship between Water Permeability and UPV in Stressed Concrete

The predictive models for evaluating the service life of concrete structures rely mainly on the mechanical and durability properties as well as the state of stress and current damage in structure. Non-destructive testing (NDT) is the preferred choice for in-situ material property evaluations including durability parameters, where applicable. Relating permeability with ultrasonic pulse velocity offers tremendous potential, especially in condition assessment of existing structures wherein a rapid and non-destructive test method is needed for durability evaluation of concrete.

In this chapter, by using the experimental data presented in previous chapters and application of the available stress-permeability and stress-UPV models, a predictive model for evaluating the permeability of concrete structures under compressive stress by measuring ultrasonic pulse velocity has been presented.

10.1. Permeability-UPV Correlation

The coefficient of water permeability and the ultrasonic pulse velocity are dimensionally similar. The experimental data, illustrated in Chapter 6, was examined for possible correlation between these two parameters. As shown in Figure 10.1 and Figure 10.2, the results of permeability and pulse velocity measurements from both plain and fiber-reinforced mortars were processed through regression analysis to obtain an empirical relationship expressed as:

$$K = Ae^{-BV} \qquad 10.1$$

Where, K is the coefficient of water permeability (m/s), V is the ultrasonic pulse velocity (m/s), and A and B are constants obtained through the regression analysis.

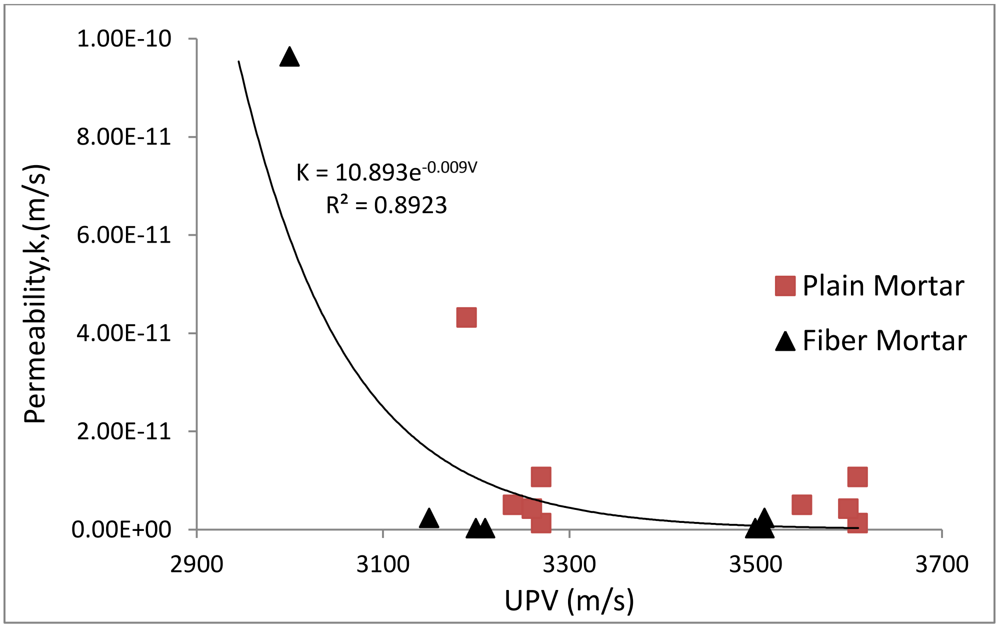

Figure 10.1. Correlation between Permeability Coefficient and UPV of Mortar Type S

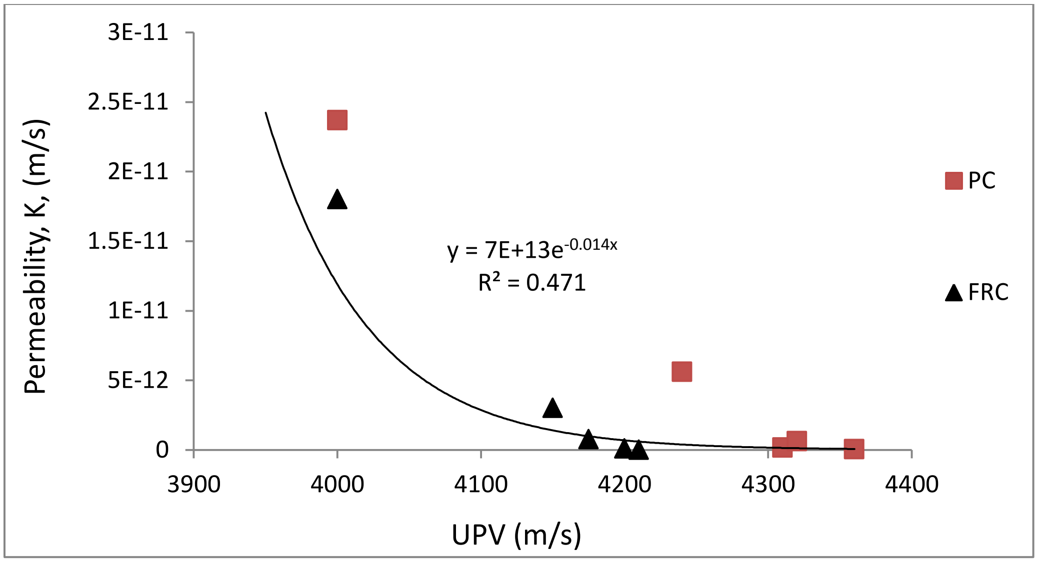

Figure 10.2. . Correlation between Permeability Coefficient and UPV of Concrete

In the present instance, the parameter A and B are: A= 10.893 and B= 0.009 for Type S mortar and A=7E+13 and B= -0.014 for concrete. Equation 10.1 suggests an exponential correlation between the UPV (as the independent variable) and the coefficient of water permeability (as the dependent variable). Further, it implies that at the lower range of pulse velocities, a minor change in the UPV results in a sharp shift in the permeability coefficient, whereas at higher values of pulse velocity, the permeability is less sensitive.

The form of the exponential relationship is in agreement with the results of Shkolnik et al. [78] who found a similar non-linear dependence between permeability and ultrasonic pulse velocity measured for specimens not under stress. While they did not specify the constants, the equation to the curve found in Shkolnik et al.[78] was derived as seen in Figure 10.3.

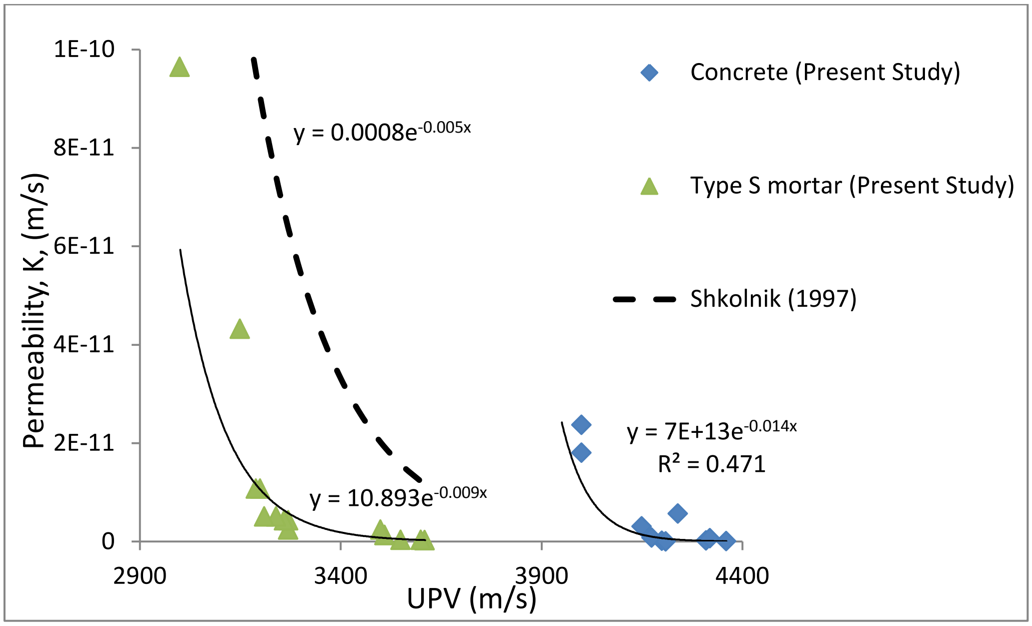

Figure 10.3. Comparison of Results from Different Studies on Correlating UPV with Permeability

This figure shows that although there is similar dependence between UPV and permeability in different types of cement-based materials, it does not follow a single relationship, and there is a shift in the correlation due to different initial microstructure.

It must be noted that the correlation expressed in Equation 10.1 was obeyed more closely within the threshold stress, i.e. in the service load region, whereas there was a visible loss in the goodness-of-fit closer to the peak-load carrying capacity. However, it should be noted that in this study different size and shape of specimens were used in measuring permeability and UPV (cylinder vs. cube) and since these factors have a large effect on the fracture properties of specimens such as crack pattern and cracking process, it may also have influenced the presented correlations. Moreover, the inclusion of the fibers changes the crack pattern from localized to distributed cracks, which also has a huge impact on both permeability and UPV measurements. Figure 10.1 to Figure 10.3 show the variation in permeability and UPV for a wide range of stress levels despite the different crack patterns.

The range of practical values of ultrasonic pulse velocities for cement-based composites is within 2,500 m/s to 4,500 m/s [80, 121]. The corresponding values for the coefficient of water permeability as predicted by Equation 10.1 lie within 10^{-9} m/s to 10^{-15} m/s.

Similar to the method presented in Chapter 9, to eliminate the effect of different initial microstructure, both permeability and UPV values are normalized to the corresponding unstressed values and the results are plotted in Figure 10.4 to Figure 10.6.

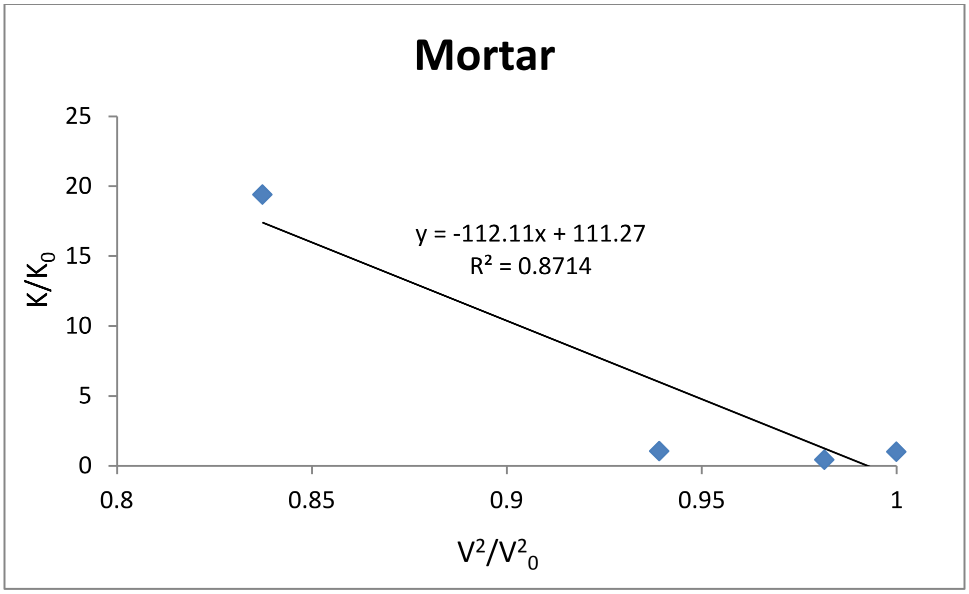

Figure 10.4. Normalized Values of Permeability and UPV for Mortar Type S

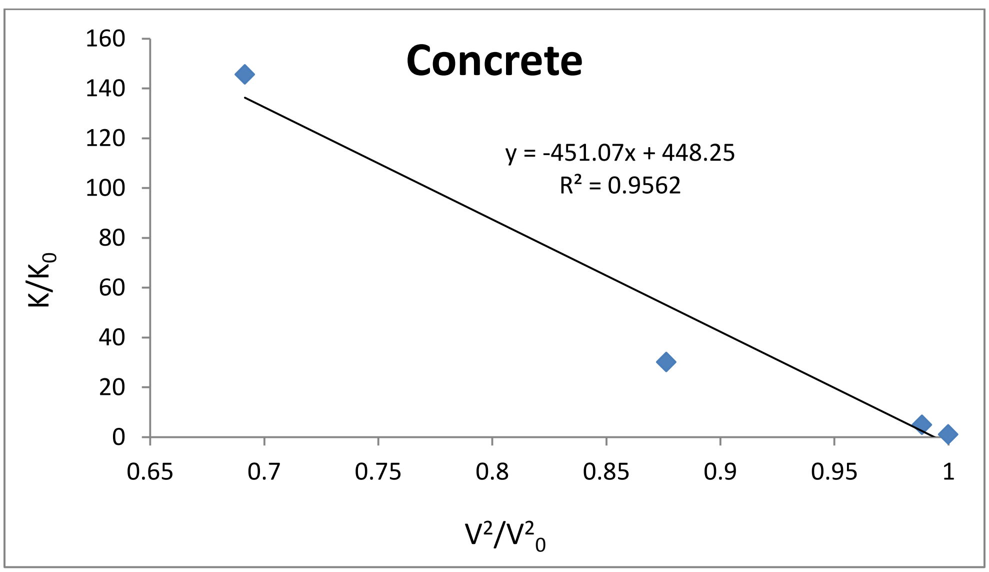

Figure 10.5. Normalized Values of Permeability and UPV for Concrete

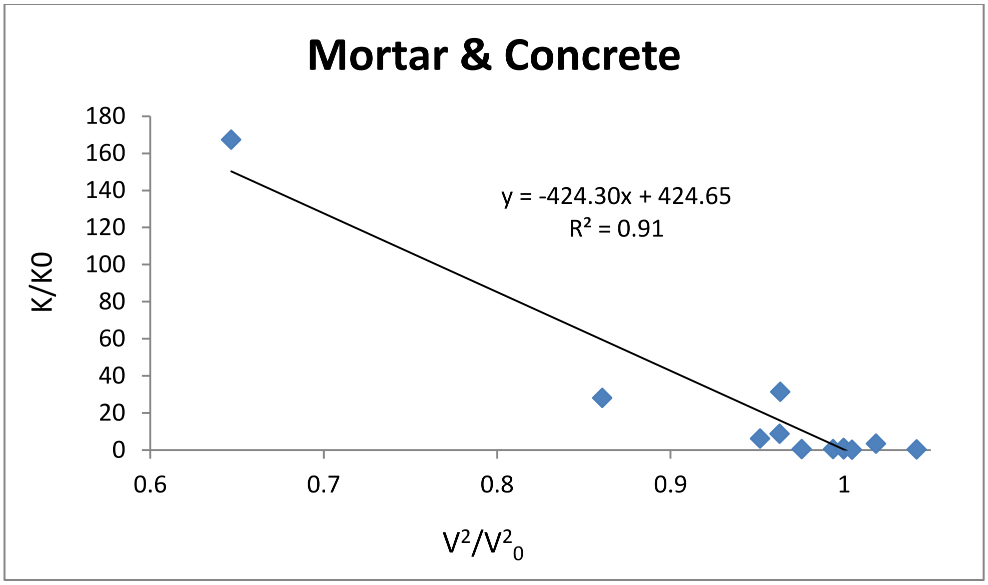

Figure 10.6. Normalized Values of Permeability and UPV for All Mixes

From these figures, it can be seen that there is a linear relationship between normalized values of permeability and UPV for the wide range of mix designs that have been evaluated. In all these cases, this relationship can be expressed as a simple format as following:

$$\frac{K}{K_0} = A\left(1 - \frac{V^2}{V_0^2}\right) \qquad 10.2$$

Where: A≈ 112 and 450 for mortar and concrete mixes, respectively.

This correlation is very similar to the model proposed by Lafhaj et al. [79] where they found a linear relationship between permeability and relative UPV for mortars under no stress (Equation 3.4 in Chapter 3).

As shown in Figure 10.6, the normalized permeability and UPV values for all the mixes (mortar and concrete) can also be expressed as a simple relationship of:

$$\frac{K}{K_0} = 424\ (1 - \frac{V^2}{V_0^2}) \qquad 10.3$$

The value of the regression coefficient (R^2) of Equation 10.3 for the data presented in Figure 10.6 is found to be 0.91 which means that the normalized measured UPV versus normalized permeability for the range of cement-based materials studied here, is correctly described by a linear relationship in the range of mixes considered.

Note that, the effect of cracking on UPV is highly directional in nature (i.e. cracks parallel to the pulse direction have little effect while cracks perpendicular to the direction would have larger effects). Thus, using UPV to evaluate changes in permeability due to cracking would only produce a suitable correlation under specific conditions of stress application wherein the crack direction is either controlled (with respect to the direction of UPV measurement) or completely random (as required by Equation 9.1 in the thesis).

As mentioned earlier, very few reports exist that correlate fluid permeability with pulse velocity in cement-based materials [78, 79]. Further, none of them considers the effect of sustained compressive stress. Lafhaj et al. [79] investigated seven mortar mixes with water to cement ratio varying from 0.3 to 0.6 and proposed a simple linear model between UPV and permeability in unstressed mortars (Equation 3.4 in Chapter 3). Shkolnik et al. [78] also used the same procedure but found an exponential relationship between UPV and permeability for their unloaded specimens. In their studies, the change in ultrasonic pulse velocity and permeability was mainly due to the change in porosity and microstructure of cement-based materials resulting from the change in water to cement ratio. Figure 10.7 and Figure 10.8 present the normalized UPV vs. permeability data from the results of Lafhaj et al. [79] and Shkolnik et al. [78] experiments. In data reproducing and plotting these figures, the initial UPV (V_0) and initial permeability (K_0) are taken as the corresponding UPV and permeability of the specimens with the lowest water to cement ratio and the other values are normalized according to these values. In other words, the specimens with the lowest water to cement ratio have been considered as analogous to unstressed specimens while increasing the water to cement ratio which increases the corresponding values of porosity, has been assumed as analogous to the stressed condition.

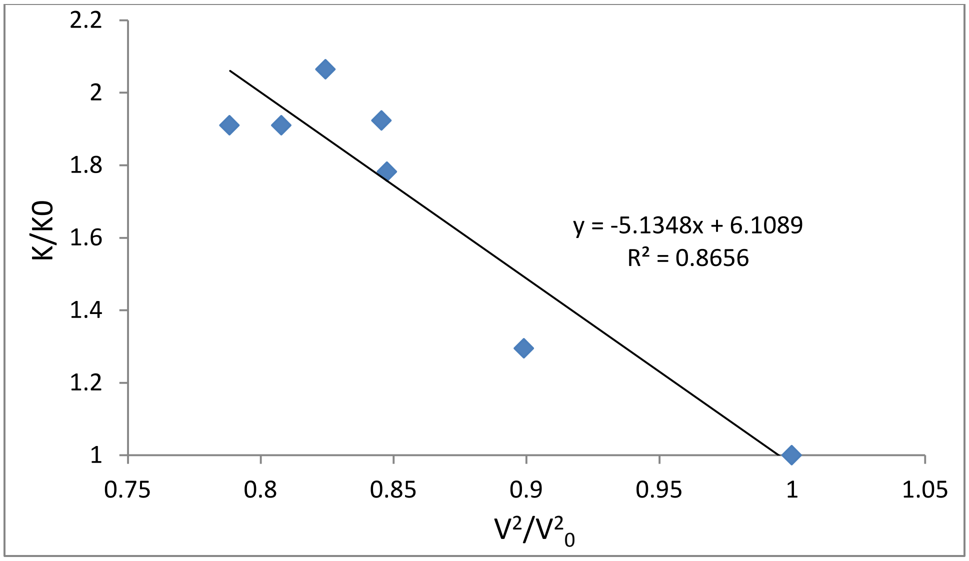

Figure 10.7. Normalized UPV vs. Permeability Reproduced from Lafhaj et al. [79].

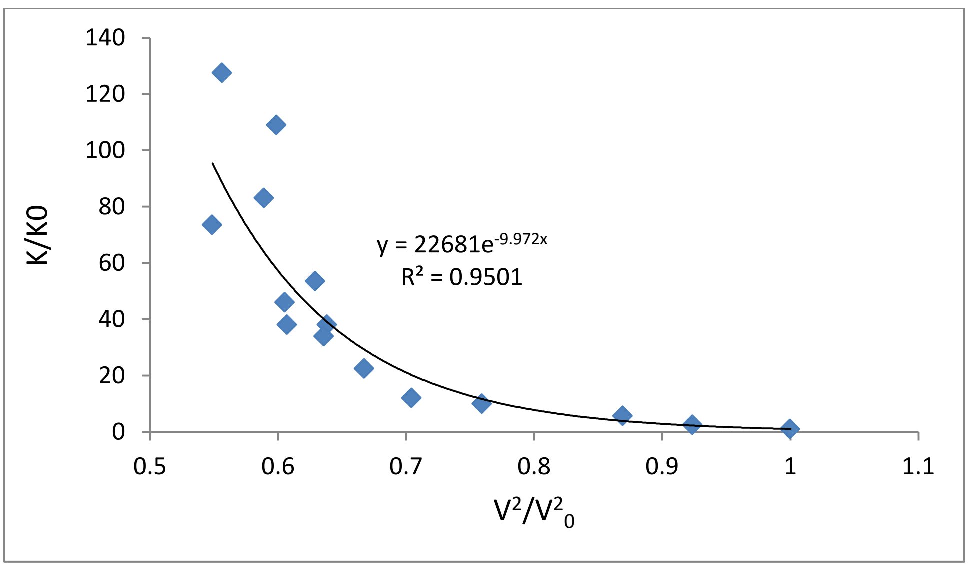

Figure 10.8. Normalized UPV vs. Permeability Reproduced from Shkolnik et al. [78]

According to these figures, while Lafhaj et al. [79] found a linear relationship between the change in permeability and UPV in their unstressed specimens, Shkolnik et al.[78] showed that this relationship is closer to an exponential format. It should be noted that the Lafhaj et al. [79] results are just in a limited range of 0.79 $<V^2/V^2_0<1$ which is corresponding to the change in permeability of just about 2 times the reference permeability whereas Shkolnik experiments covered a wider range of UPV changes $(0.54<V^2/V^2_0<1)$ and up to a corresponding permeability change of about 130 times. Moreover, there are only 3 data points in Shkolnik's study which are in the same range as of Lafhaj's data.

The results of Lafhaj et al. [79] (Figure 10.7) study shows that there is a good linear relationship between the normalized permeability and normalized UPV values in the range of permeability and UPV changes in their study. However, the slope of the linear fit in their study is different from the slope of the linear regression of the present study plotted in Figure 10.6 (compare the coefficient of about 424 in Figure 10.6 to the coefficient of about 5 in Figure 10.7). This is probably due to the different nature of the change in microstructure caused by mechanical stress (the aim of this study) and by the water to cement ratio variation (the goal of Lafhaj et al. study). While the former is attributed to the change in connected porosity, the latter is because of the change in total porosity and hence the two linear plots do not follow the same relationship. The change in the corresponding values of permeability in the two plots mentioned above which is just about 2 times in Lafhaj study compared to about 170 times in present study, verifies this theory as illustrated in Figure 10.9

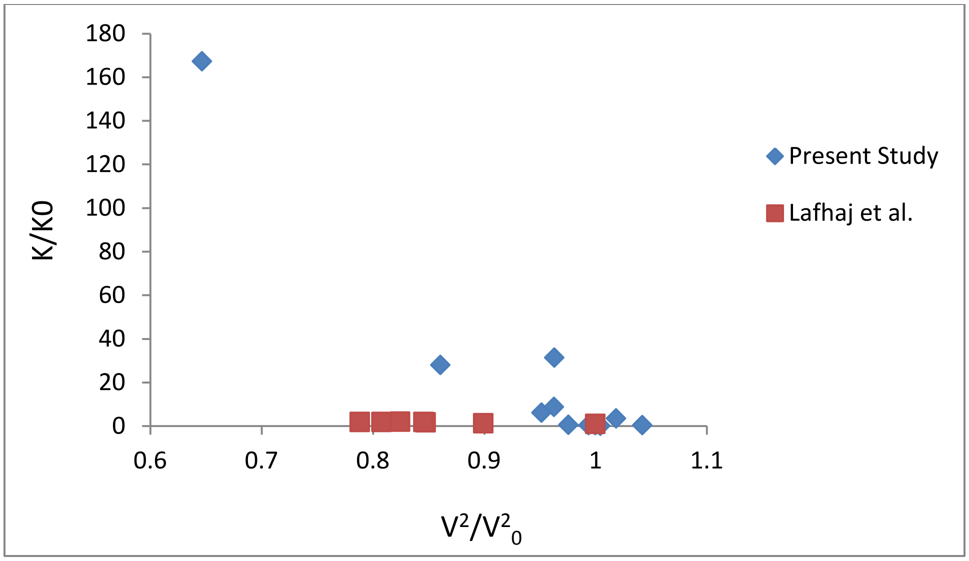

Figure 10.9. Comparison between Lafhaj et al .[79] Data with the Present Study

The figure shows that although both the present study and the results of Lafhaj et al. [79] show a linear relationship between permeability and UPV, due to a different nature of the change in microstructure caused by stress and the water to cement ratio variation, the two sets of data points do not follow a close linear relationship. It should be emphasized that the higher rate of pore connectivity rise in specimens subjected to mechanical stress compared to an increase in water to cement ratio is the main reason for this difference. Moreover, due to the higher number of Shkolnik's data points which follow an exponential trend, the general trend for all the studies obeys an exponential relationship rather than a linear one.

Figure 10.10 illustrates the normalized UPV versus permeability data from the present study along with the Lafhaj et al. [79] and Shkolnik et al. [78] data presented in Figure 10.7 and Figure 10.8, all on the same graph. The figure shows that while at values of V/V_0 close to 1 (between 0.97 and 1) which are corresponding to the UPV of the unstressed or low stressed specimens, the change in permeability of loaded specimens are close to that of the specimens with varying water to cement ratio, by decreasing the UPV, the change in permeability due to the presence of load is much greater compared to its change due to the change of microstructure as a result of increasing the water to cement ratio. This observation shows that the pore connectivity changes much more in the presence of stress rather than its increase due to the increase of the total porosity in higher water to cement ratios.

Figure 10.10 also depicts that the UPV is less sensitive to the change of microstructure due to the loading rather than increases in water to cement ratio. While there was about a 45 percent decrease in UPV due to the increase in water to cement ratio, by loading the specimens up to loads close to failure the decrease in UPV is less than 35 percent. At the same time, comparing Lafhaj et al. [79] results with the present study data revealed that the increase in permeability of stressed specimens is more than that of with increased water to cement ratio. This shows that mechanical stress has a much greater effect on increasing the permeability than decreasing the UPV.

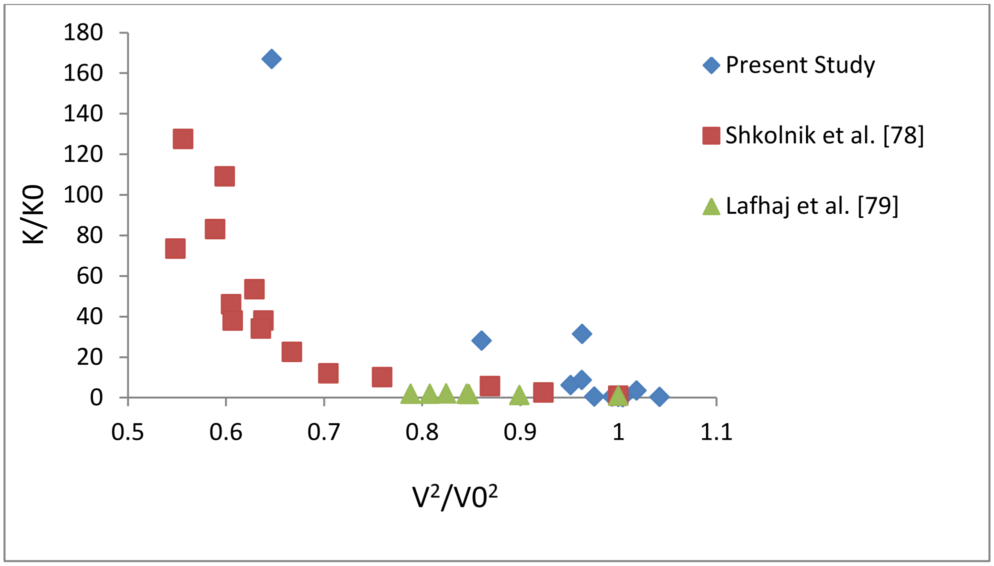

Figure 10.10. Comparing the Data by Shkolnik et al. [78] and Lafhaj et al. [79] with the Present Study

Figure 10.11 illustrates all the data presented in Figure 10.10 along with the linear relationship between normalized UPV and permeability values stated in Equation 10.3. the figure shows that at the same levels of change in UPV, the increase of permeability in loaded specimens are much more than that of unloaded specimens with higher water to cement ratios which clearly distinguish between the effect of increase in cracking with that of higher porosities.

It should be noted that although the Equation 10.3 is found to be the best fitted curve to the experimental values of present study, due to the sharp jump in permeability and sudden drop in UPV values at high levels of stress and consequently no normalized UPV values between 0.65 and 0.85 as well as no normalized permeability values between 32 and 167, there is a question of whether the in-between values of normalized UPV and permeability follow this linear trend or other trends such as exponential. The sharp jump in permeability and sudden drop in UPV is associated with the creating of large single cracks at load levels close to the ultimate.

As illustrated in Figure 10.11, regardless of the method of creating the voids in cement-based materials, whether they create by increasing the water to cement ratio or by application of the stress, normalized permeability versus normalized UPV values can better be presented by an exponential relationship rather than a linear one.

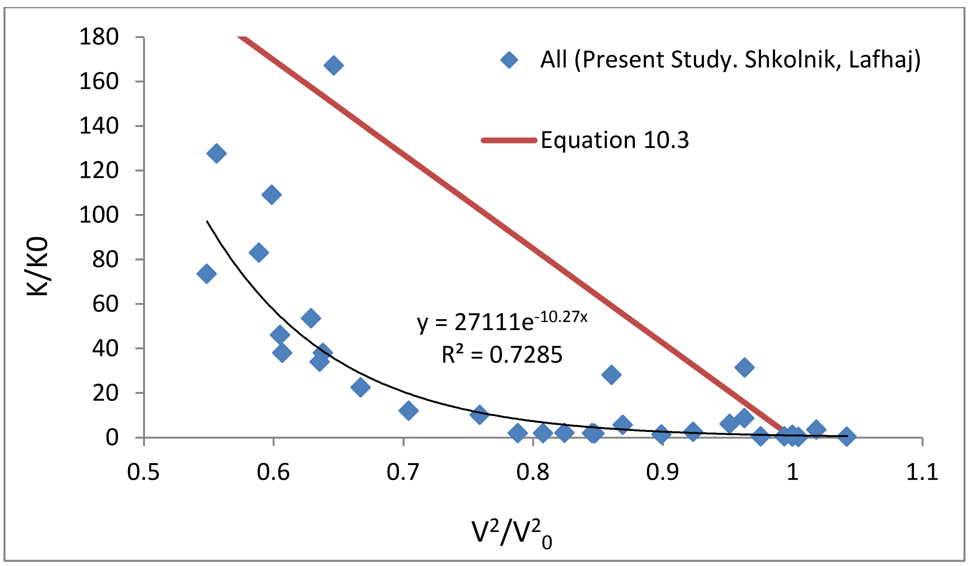

Figure 10.11. All the Data from Lafhaj et al. [79] and Shkolnik et al. [78] and Present Study

Lafhaj et al. [79] data and the linear range of Shkolnik et al. [78] results have been selected and plotted in Figure 10.12 individually and with the results of present study corresponding to the same range of V^2/V_0^2 of these two studies ($0.7<V^2/V_0^2<1$) in Figure 10.13, respectively. Figure 10.12 shows that although both Lafhaj et al. [79] and Shkolnik et al. [78] data are the results of changing the microstructure of cement-based materials by variation in w/c ratio, the change in permeability by change in UPV does not follow the same equation even in the linear range of their test results. Therefore, it is not surprising that plotting the results of these two studies with the present study (which the velocity and permeability changes are stress induced) would result in a scatter plot as shown in Figure 10.13 even in the linear ranges.

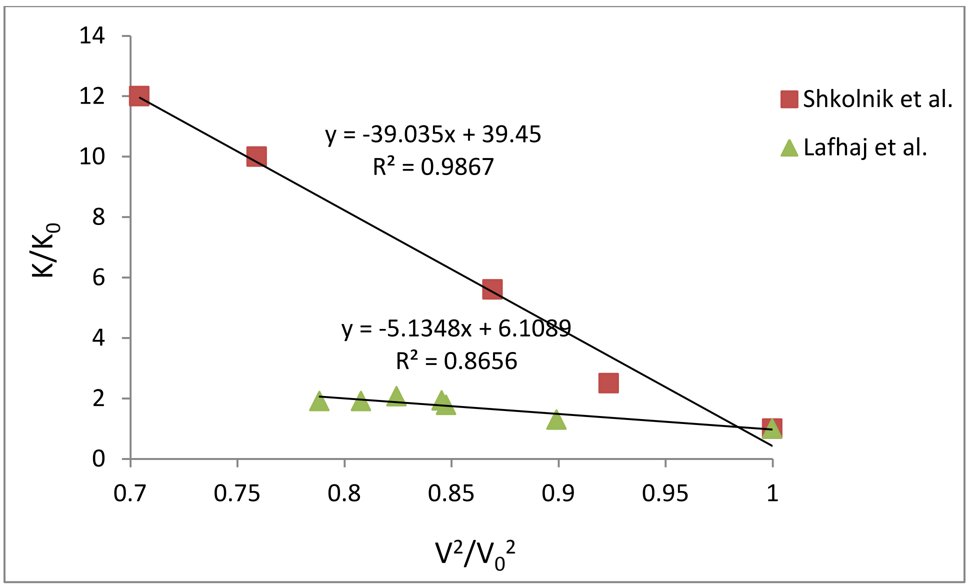

Figure 10.12 Linear Range of the Data by Lafhaj et al. [79] and Shkolnik et al. [78]

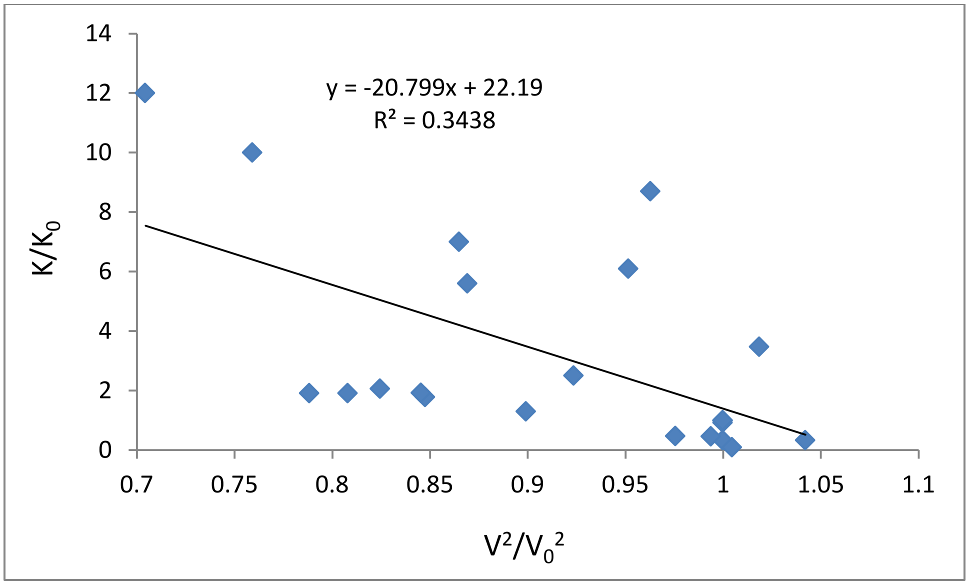

Figure 10.13 Linear Range of the Data by Lafhaj et al. [79], Shkolnik et al. [78] and Present Study

10.2. Permeability- UPV Modeling

10.2.1. Stress-Permeability

Permeability simulation in the concrete requires a model that reflects the relationship between permeability and stress. While there are no such models available for concrete, David et al. [122] suggested an exponential relationship would be suitable for describing the stress dependent permeability. Their results were based on laboratory experiments for five different sandstones. Evans et al. [123] also noted that the stress dependent permeability for granite rocks exhibit an exponential relationship. The exponential relationship for the stress dependent permeability can be expressed as follows:

$$K = K_0 e^{\alpha\sigma} \qquad 10.4$$

Where,

K: Permeability under stress;

K_0: Permeability under no stress;

σ: Stress level (varying from 0 to 1) and

α: Material constant

Or:

$$\frac{K}{K_0} = f_1(\sigma) \qquad 10.5$$

Where:

$$f_1\,(\sigma) = e^{\alpha\sigma} \qquad 10.6$$

Based on the permeability measurement results presented in Figure 6.3 to Figure 6.6 in Chapter 6, the parameters in Equation 10.5 can easily be determined using the curve fitting on the average results of permeability values of mortar and concrete specimens. Since in Equation 10.5 the normalized values of permeability (K/K_0) which are independent of the different initial permeability values for mortars and concrete specimens are considered, the parameters in the exponential relationship are determined for the average of the measured permeability values. In this case, from the curve fitting, the parameter α is about 5.26 and Equation 10.5 can be written as:

$$\frac{K}{K_0} = e^{5.26\sigma} \qquad 10.7$$

10.2.2. Stress-UPV

The stress-dependency of ultrasonic wave velocity is called acoustoelastic effect. The velocity of longitudinal waves propagating in a direction perpendicular to the direction of the uniaxially applied stress in a homogeneous material is given as [124]:

$$\rho_0 V^2 = \rho_0 V_0^2 - \frac{\sigma}{E}[(3\lambda - 6l - 2m - 2\nu(5\lambda + 7\mu - 6l - m)] \quad 10.8$$

Where:

V: wave velocity in stressed condition

V_0: wave velocity in unstressed condition

P_0: density in unstressed condition

σ: the state of stress

ν: Poisson's ratio

E: Modulus of elasticity

l, m, and n: Murnaghan's third order elastic (TOE) constants

λ and μ: the second order elastic (SOE) constants generally known as Lame' constants

By dividing the both sides of Equation 10.8 to $\rho_0 V_0^2$ and considering the dependency of the modulus of elasticity on the stress (Figure 7.1 and Figure 7.2), the relationship between wave velocity and stress can be expressed as:

$$V = V_0\sqrt{1 - f_2(\sigma)} \quad 10.9$$

Where, f_2 (σ) is the function of the applied stress as the variation and the other parameters introduced in Equation 10.8 as the constants.

Equation 10.9 indicates an approximate relationship between the applied uniaxial stress and the ultrasonic wave velocities.

From the UPV-Stress plots presented in Chapter 6, the f_2 (σ) function in Equation 10.9 can easily be determined using the curve fitting on the values of UPV for mortar and concrete specimens. Since in Equation 10.9 the normalized values of UPV (V/V_0) which are independent of the different initial permeability values for mortars and concrete specimens, are considered, the f_2 (σ) is determined for the average of the measured permeability values and can be expressed as:

$$f_2(\sigma) = 2.4\times10^{-3}\, e^{5.18\sigma} \qquad 10.10$$

Taking similar approach for the wave velocities propagating in different directions rather than measured in this study and by using the corresponding equations derived by Takahashi et al. [124], the relationship between the applied stress and the velocities of longitudinal and transverse waves could be obtained.

10.2.3. Permeability- Stress- UPV

By combining Equation 10.5 and Equation 10.9:

$$\frac{K}{K_0} = \frac{f_1\ (\sigma)}{f_2\ (\sigma)}\ (1 - \frac{V^2}{V_0^2}) \qquad 10.11$$

Or:

$$\frac{K}{K_0} = f\ (\sigma)\ (1 - \frac{V^2}{V_0^2}) \qquad 10.12$$

Where:

$$f\ (\sigma) = \frac{f_1(\sigma)}{f_2(\sigma)} \qquad 10.13$$

Equation 10.12 presents the general form of the dependency of stress-permeability-wave velocity in a material. For the mix designs investigated in this research and according to Equation 10.7 and 10.10:

$$f\,(\sigma) = 416\ e^{-0.11\sigma} \qquad 10.14$$

Therefore,

$$\frac{K}{K_0} = 416\ e^{-0.11\sigma}\ (1 - \frac{V^2}{V_0^2}) \qquad 10.15$$

By comparing Equation 10.15 with Equation 10.2, the coefficient A which is calculated using the average values of permeability and UPV in each stress level for mortar and concrete, is found to be a function of stress:

$$A = 416 \times e^{-0.11\sigma} \qquad 10.16$$

By changing the stress levels from 0 (unstressed condition) to 1 (ultimate stressed level), the corresponding values of A varies between 416 and 372.

Figure 10.14 compares the normalized permeability values calculated using Equation 10.3 which considers coefficient A as a constant (A=424) and Equation 10.15 which shows the stress-dependency of this coefficient. The figure depicts that both equations produce almost the same values of normalized permeability and the variation of coefficient A with stress can be neglected.

This result shows that the correlation between normalized values of permeability and UPV in the wide range variety of the cement-based materials studied here can be expressed with a simple relationship expressed in Equation 10.3.

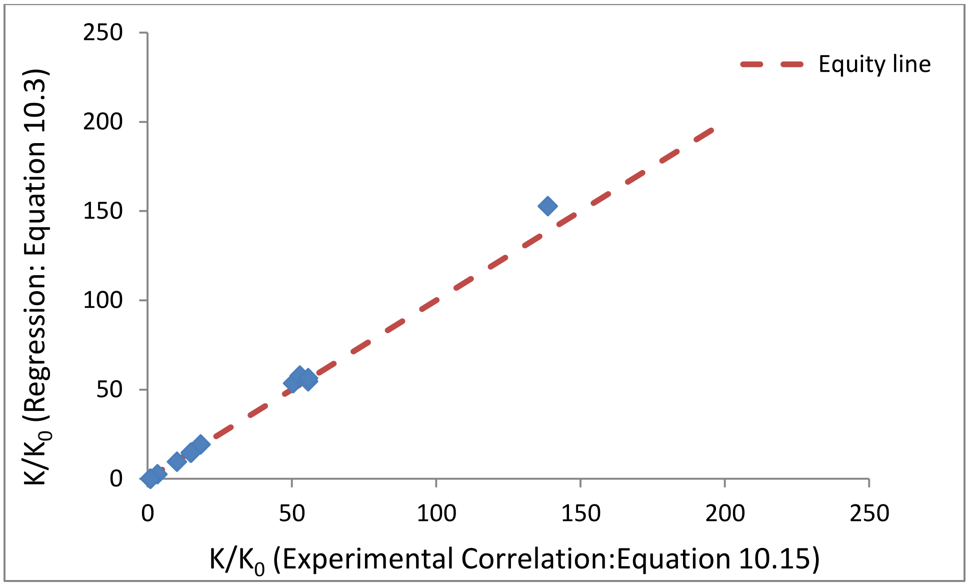

Figure 10.14 Comparing the Normalized Permeability Values

11. Conclusions and Recommendations for Future Studies

11.1. Summary

The overall objective of this dissertation was to find out how the permeability, ultrasonic wave velocity, mechanical stress-induced damage and three-dimensional microstructure of cement-based materials change under different levels of stress. Specifically, the thesis had two distinct objectives: The first goal was to develop a model for predicting the change in water permeability of cement-based materials under stress through the non-destructive method of measuring the corresponding ultrasonic pulse velocity values. The second objective was to finding a method to quantify the change in the three-dimensional microstructure and pore connectivity of the cement-based materials under different levels of loading. Moreover the effect of incorporation of polypropylene fibers was investigated.

For reaching the first goal, experimental programs were designed to measure both the water permeability and ultrasonic pulse velocity of mortar and concrete specimens under the simultaneous application of compressive stress. A permeability test setup capable of measuring the water permeability of mortar and concrete specimens under the simultaneous effect of compression stress was developed. The set up was further modified to pay special attention to measure the permeability coefficients under the conditions of the steady state of the flow by monitoring the real-time flow rate of water in permeability tests. Four sets of cement-based mix designs including: plain mortar, fiber reinforced mortar, plain concrete and fiber reinforced concrete were investigated in both water permeability and UPV experiments. All the tests were carried out under stresses which varied from 0 percent (unstressed condition) to 90 percent of ultimate. Based on the experimental results and using the available general models of permeability-stress and UPV-stress, a permeability-UPV model was proposed. The results were also compared to the few existing permeability-UPV models for unstressed cement-based materials.

In the second phase, by employing the x-ray tomography scan technique the three-dimensional images from the mortar specimens subjected to different levels of stress were taken. The images were analyzed to study the effect of loading on the three-dimensional microstructure of cement-based materials. For this part, parameters such as total porosity, void specific surface area, void shape factor, void size distribution and void spacing factor were calculated for each stress level and the results were discussed. For the purpose of studying the change in connected porosity of the cement-based materials under stress, by using a connected component labeling algorithm and further analyzing the labeled components, the number of connected pores in each stress level was calculated. Moreover, a parameter called “connected porosity” which is defined as the percentage of the connected pores in a specimen, was defined and calculated.

Finally, for quantifying the amount of damage in the specimens under loading, a stress-induced damage parameter was defined and the changes in water permeability, ultrasonic pulse velocity, three-dimensional microstructure properties and the void connectivity with the damage value under stress were investigated accordingly.

11.2. Overall Conclusions

From the work presented and discussed in this dissertation, the following conclusions can be drawn:

1. Under compression, the water permeability of cement-based materials may be evaluated after achieving equilibrium in flow. The permeability coefficient is sensitive to the applied compressive stress beyond a certain threshold value, which corresponds to 20% of the compressive strength in plain specimens and 30% of the strength in polypropylene fiber-reinforced specimens for the range of compressive strengths studied here.

2. Inclusion of the fibers in cement-based mix designs increases the threshold stress level and hence makes them more resistant to the transportation of deleterious substances. However, in high stress levels close to ultimate, due to the creation and propagation of a single large crack, the effectiveness of the fibers may diminish.

3. It has been shown that the propagation velocities of the waves in cement-based materials are stress-dependent. This stress-dependency of the waves should be taken into account when concrete structures are inspected by acoustic techniques. If the “stress-wave velocity” relationship is established, by measuring the wave velocities in concrete structure under service conditions, the state of stress can be calculated. As shown, the change in the wave velocities at certain stress levels can be attributed to the state of the stress-induced damage in cement-based materials. By measuring the change in UPV (on unloaded specimen and during the course of stress application), information about stress level, the state of cracking and internal damage in cement-based materials can be obtained.

4. The behavior of UPV under compression stress can adequately be modeled by Sayers microcrack model as well as the Hudson’s acoustoelastic model.

5. A sharp increase in permeability occurs at stress levels of about 60% of the compressive strength in all of the studied materials. By introducing a damage value parameter, the onset of damage value was found to occur around the same stress level. These findings support a design approach which limits service load stresses to 60% of peak capacity.

6. A non-linear dependence exists between the coefficient of water permeability and the velocity of ultrasonic pulses through cement-based materials under compression. However, the normalized permeability values can be related to the normalized wave velocities by a linear correlation with a good accuracy.

7. Using available stress-permeability and stress-UPV models, a mathematical permeability-stress-UPV model was developed and calibrated by application of the experimental results of this study. However, the low sensitivity of the stress term of this model to the stress level values allows replacing it by a constant coefficient. In other words, although both permeability and UPV have been proven to be stress-dependent, the normalized permeability-UPV relationship for loaded cement-based materials can be related to each other independent of the applied stress.

8. The comparison of this study's results with the finding of few available studies on permeability-UPV relationship in cement-based materials under no stress shows that at the V/V_0 closer to 1, all the models predict close results for permeability. On the other hand, by reducing the V/V_0, the permeability of stressed specimens (present study) changes at a much higher rate than that of unstressed models. This finding was explained by the difference in the mechanism governing microstructural changes. So that under stress, the microstructure changes due to the creation of cracks and increase in the pore connectivity. On the other hand, in previously available models, the change is just due to the change in total porosity.

It has been concluded that the pore connectivity changes much more in the presence of stress while a difference in mix design parameters alters the total porosity instead.

9. The x-ray tomography scanning technique provides valuable information about the three-dimensional microstructure of cement-based materials. The developed method for finding the number and percentage of the connected pores in cement-based materials has found to have a much better correlation with the transport properties than that of total porosity.

10. Application of compressive stress increases the connected porosity at a much faster rate than total porosity. Whereas the total porosity registered an increase of a mere 30% upon stressing a cement-based mortar sample to failure, the corresponding increase in the connected porosity was about 120% over the same load range. This illustrates that more than the creation of new voids, it is the forging of connectivity between existing pores and microcracks that leads to permeability. In other words, under stress, the process of propagating and interconnecting of the existing pores are more dominant than creation of new cracks. This indirectly shows the significance of a single crack (or a few large cracks) in governing water transport close to the failure load under compression.

11. The newly defined and measured connected porosity parameter is able to predict the permeability of mortars with a higher coefficient of determination than the total porosity.

12. The results of this study show that the UPV depends not only on the amount of the pores and voids in cement-based materials but also on their interconnectivity. However, the connectivity is not as much effective on UPV as it is on permeability. In other words, the velocities of ultrasonic wave in materials depend mainly on the amount of the total voids which affect density and modulus of elasticity of the material and are not sensitive to void connectivity as much as permeability is.

13. The damage value parameter defined here has showed a better correlation with the connected porosity changes than with the total porosity of mortar specimens under stress.

14. One application for the findings of this study would be measuring the permeability and UPV of unstressed concrete as part of mix design or quality control/quality assurance stage of the project. By measuring the change in the UPV of concrete in service, one may obtain information about the stress level, the state of cracking and internal damage in materials.

11.3. Recommendations for Future Studies

Although this research is the most comprehensive study on the effect of stress on permeability and UPV of cement-based materials to date, there are a few research areas that might be useful to even gain a broader knowledge on this subject. Moreover, for the three-dimensional microstructural studies using x-ray tomography scanning technique, there are advancements necessary in order to improve our confidence in the results and improve the range of information that can be gained from these experiments. Therefore, there are a few recommendations for future researches in this area:

1) For verifying the validity of proposed permeability-stress-UPV model for wider ranges of cement-based materials, studying other mix designs such as high strength concrete and lightweight concrete as well as incorporating different types and dosages of fibers is recommended. It is also recommended to use specimens with the similar shape and size for both permeability and UPV measurements in future studies.

2) For future studies on the effect of stress on permeability of concrete, it is recommended to elevate the load in lower increments between 50-90% of ultimate stress to capture more data points in this region to confirm whether the observed trend is valid for all the stress levels.

3) The investigation of the effect of stress on the relationship between permeability and other relevant NDT techniques such as electrical resistivity in which depends mainly on the pore connectivity is suggested.

4) One of the changes which is needed in the x-ray tomography experiments is to improve the test set up for being capable of taking the three-dimensional images while specimens are simultaneously under stress. Moreover, investigating cylindrical specimens with larger sizes is suggested. It would also be good to expand the range of resolutions to something around 1 μm. This would allow for studies of smaller voids for getting more realistic values of pore connectivity change under stress.

5) Using the same procedure for finding the pore connectivity in 2D images, it is recommended to develop a similar program to find 3D connectivity. The results would give a more realistic representation of the change of concrete microstructure and its relationship to permeability under stress.

References

[1] J. P. Broomfield, *Corrosion of Steel in Concrete: Understanding, Investigation and Repair*. E. & F.N. Spon Ltd, 1997.

[2] P. Carter, "A national agenda for technological research and development in road and inter-modal transportation," Transportation Association of Canada, 1999.

[3] Anonymous "Future highway needs: A 10 year view of alberta's transportation needs," Alberta Infrastructure & Transportation (AIT), 2001.

[4] W. E. Norris, D. J. Naus and H. L. Graves, "Inspection of nuclear power plant containment structures," *Nucl. Eng. Des.*, vol. 192, pp. 303-329, 9/1, 1999.

[5] M. Choinska, A. Khelidj, G. Chatzigeorgiou and G. Pijaudier-Cabot, "Effects and interactions of temperature and stress-level related damage on permeability of concrete," *Cem. Concr. Res.*, vol. 37, pp. 79-88, 1, 2007.

[6] H. R. Samaha and K. C. Hover, "Influence of microcracking on the mass transport properties of concrete," *ACI Materials Journal*, vol. 89, pp. 416-424, 1992.

[7] A. Bentur, S. Diamond and N. S. Berke, *Steel Corrosion in Concrete: Fundamentals and Civil Engineering Practice.* Taylor & Francis, 1997.

[8] E. Poulsen and L. Mejlbro, *Diffusion of Chloride in Concrete: Theory and Application.* Taylor & Francis, 2006.

[9] P. K. Mehta, *Concrete in Marine Environment'.* Routledge Publication, 1991.

[10] K. K. Aligizaki, *Pore Structure of Cement-Based Materials: Testing, Interpretation and Requirements.* Taylor & Francis, 2006.

[11] P. K. Mehta and P. J. M. Monteiro, *Concrete: Structure, Properties and Materials.* Prentice Hall, 1993.

[12] A. M. Neville, *Properties of Concrete'.* John Wiley & Sons, 1996.

[13] J. Marchand and B. Gerard, "Microstructure-based models for predicting transport properties," E&FN Spon, 1997.

[14] P. A. M. Basheer, "Permeation analysis," in *Handbook of Analytical Techniques in Concrete Science and Technology,* V. S. Ramachandran and J. J. Beaudoin, Eds. William Andrew, 2001, .

[15] P. B. Bamforth, "The relationship between permeability coefficients for concrete obtained using liquid and gas," *Magazine of Concrete Research,* vol. 39, pp. 3-11, 1987.

[16] L. J. Klinkenberg, "The permeability of porous media to liquids and gases," *Drilling and Production Practice,* 1941.

[17] Anonymous "Permeability testing of site concrete: A review of methods and experience," Concrete Society, Tech. Rep. 31, 1985.

[18] J. Crank, *The Mathematics of Diffusion.* Oxford university press, 1983.

[19] L. Tang, "Chloride transport in concrete-Measurement and prediction," 1996.

[20] C. M. Hansson, H. Strunge, J. B. Markussen and T. Frolund, "The effect of cement type on the diffusion of chloride," *Nordic Concrete Research,* pp. 70-80, 1985.

[21] M. Hoseini, "The Effect of Different Surface Coatings on the Diffusion of the Chloride Ion into Concrete in Persian Gulf Region Comparing with results of Laboratory Experiments and Economical Analysis for Life Cycle Cost’," 2003.

[22] N. Banthia and A. Bhargava, "Permeability of stressed concrete and role of fiber reinforcement," *ACI Materials Journal,* vol. 104, 2007.

[23] G. Vondran and T. Webster, "Relationship of Polypropylene Fiber Reinforced Concrete to Permeability," *Special Publication,* vol. 108, pp. 85-98, 1988.

[24] H. G. Wheat, "Using polymers to minimize corrosion of steel in concrete," *Cement and Concrete Composites,* vol. 24, pp. 119-126, 2002.

[25] A. H. J. Al-Tayyib and M. Mesfer, "Corrosion of steel reinforcement in polypropylene fiber reinforced concrete structures," *ACI Mater. J.,* vol. 87, 1990.

[26] P. Zoltanetzky, J. Parnes and C. Gordon, "Four-year study: Effects of polypropylene fibers in reducing corrosion of rebars in concrete," in *Workshop on Fiber Reinforced Cements and Concretes,* 1994, .

[27] M. A. Sanjuan, C. Andrade and A. Bentur, "Effect of crack control in mortars containing polypropylene fibers on the corrosion of steel in a cementitious matrix," *ACI Mater. J.,* vol. 94, 1997.

[28] D. Whiting and A. Walitt, Eds., *Permeability of Concrete.* ACI (Amrican Concrete Institute), 1988.

[29] Anonymous "Standard test method for water permeability of concrete," *CRD-C48-92*, 1992.

[30] Anonymous "Test method for water permeability of concrete using triaxial cell," *CRD-C163-92,* 1992.

[31] Anonymous "Concrete hardened - determination of the depth of penetration of water under pressure," *ISO/DIS 7031,* .

[32] J. Kropp, "Concrete Durability–An approach towards performance testing, Final report of RILEM Technical Committee 116-PCD," *Materials Structures*, vol. 32, pp. 163–173, 1999.

[33] A. Kermani, "Permeability of stressed concrete," *Building Research & Information*, vol. 19, pp. 360-366, 1991.

[34] K. Wang, D. C. Jansen, S. P. Shah and A. F. Karr, "Permeability study of cracked concrete," *Cem. Concr. Res.,* vol. 27, pp. 381-393, 1997.

[35] C. M. Aldea, S. P. Shah and A. Karr, "Permeability of cracked concrete," *Mater. Struct.,* vol. 32, pp. 370-376, 1999.

[36] C. M. Aldea, M. Ghandehari, S. P. Shah and A. Karr, "Estimation of Water Flow through Cracked Concrete under Load," *ACI Mater. J.,* vol. 97, 2000.

[37] J. Rapoport, C. M. Aldea, B. Ankenman and A. Karr, "Permeability of cracked steel fiber-reinforced concrete," *J. Mater. Civ. Eng.,* vol. 14, pp. 355, 2002.

[38] J. Rapoport, C. M. Aldea, B. Ankenman and A. Karr, "Permeability of cracked steel fiber-reinforced concrete," National Institute of Statistical Sciences, Tech. Rep. 115, 2001.

[39] A. Biparva, "Permeability and durability of high volume fly ash concrete under an applied compressive stress," 2005.

[40] N. Hearn and G. Lok, "Measurement of permeability under uniaxial compression: a test method," *ACI Mater. J.,* vol. 95, 1998.

[41] T. Sugiyama, T. W. Bremner and T. A. Holm, "Effect of stress on gas permeability in concrete," *ACI Mater. J.,* vol. 93, 1996.

[42] V. Picandet, A. Khelidj and G. Bastian, "Effect of axial compressive damage on gas permeability of ordinary and high-performance concrete," *Cem. Concr. Res.,* vol. 31, pp. 1525-1532, 2001.

[43] A. Bhargava and N. Banthia, "Measurement of concrete permeability under stress," *Exp Tech,* vol. 30, pp. 28-31, 2006.

[44] J. S. Lawler, D. Zampini and S. P. Shah, "Permeability of cracked hybrid fiber-reinforced mortar under load," *ACI Mater. J.,* vol. 99, 2002.

[45] D. Ludirdja, R. L. Berger and J. F. Young, "Simple method for measuring water permeability of concrete," *ACI Mater. J.,* vol. 86, 1989.

[46] S. Yoon, K. Wang, W. J. Weiss and S. P. Shah, "Interaction between loading, corrosion, and serviceability of reinforced concrete," *ACI Mater. J.,* vol. 97, pp. 637-644, 2000.

[47] N. Banthia, A. Biparva and S. Mindess, "Permeability of concrete under stress," *Cem. Concr. Res.,* vol. 35, pp. 1651-1655, 2005.

[48] C. M. Aldea, S. P. Shah and A. Karr, "Effect of cracking on water and chloride permeability of concrete," *J. Mater. Civ. Eng.*, vol. 11, pp. 181, 1999.

[49] M. Tsukamoto and J. D. Worner, "Tightness of Fiber Concrete, Darmstadt Concrete," *Annual Journal on Concrete and Concrete Structures,* vol. 5, pp. 215-225, 1990.

[50] AASHTO T277, "Standard method of test for rapid determination of the chloride permeability of concrete," .

[51] C. M. Aldea, M. Ghandehari, S. P. Shah and A. Karr, "Combined effect of cracking and water permeability of concrete," in *Fourteenth Engineering Mechanics Conference, ASCE-ME2000,* Austin,Texas, .

[52] J. S. Lawler, D. Zampini and S. P. Shah, "Microfiber and macrofiber hybrid fiber-reinforced concrete," *J. Mater. Civ. Eng.,* vol. 17, pp. 595, 2005.

[53] D. C. Jansen and S. P. Shah, "Effect of length on compressive strain softening of concrete," *J. Eng. Mech.,* vol. 123, pp. 25, 1997.

[54] N. Hearn and R. H. Mills, "A simple permeameter for water or gas flow," *Cem. Concr. Res.,* vol. 21, pp. 257-261, 1991.

[55] J. J. Kollek, "The determination of the permeability of concrete to oxygen by the Cembureau method—a recommendation," *Mater. Struct.,* vol. 22, pp. 225-230, 1989.

[56] J. G. Cabrera and C. J. Lynsdale, "A new gas permeameter for measuring the permeability of mortar and concrete," *Magazine of Concrete Research,* vol. 40, pp. 177-182, 1988.

[57] M. Saito and H. Ishimori, "Chloride permeability of concrete under static and repeated compressive loading," *Cem. Concr. Res.,* vol. 25, pp. 803-808, 1995.

[58] S. D. Santiago and H. K. Hilsdorf, "Fracture mechanisms of concrete under compressive loads," *Cem. Concr. Res.,* vol. 3, pp. 363-388, 1973.

[59] N. Hearn, "Effect of shrinkage and load-induced cracking on water permeability of concrete," *ACI Mater. J.,* vol. 96, 1999.

[60] D. Breysse and B. Gerard, "Cracking of Concrete Relevance and Effects, Tightness of Concrete with Respect to Fluids," *RILEM TC-146 TCF State-of-the-Art Report,* 1997.

[61] B. Gerard, D. Breysse, A. Ammouche, O. Houdusse and O. Didry, "Cracking and permeability of concrete under tension," *Mater. Struct.,* vol. 29, pp. 141-151, 1996.

[62] B. Gerard, H. W. Reinhardt and D. Breysse, "Measured transport in cracked concrete," *Penetration and Permeability of Concrete: Barriers to Organic and Contaminating Liquids: State-of-the-Art Report Prepared by Members of the RILEM Technical Committee 146-TCF,* pp. 265, 1997.

[63] C. A. Clear, *The Effects of Autogenous Healing upon the Leakage of Water through Cracks in Concrete.* Cement and Concrete Association, 1985.

[64] ASTM C1202, "Standard Test Method for Electrical Indication of Concrete’s Ability to Resist Chloride Ion Penetration," *Annual Book of ASTM Standards,* vol. 4, .

[65] W. S. Najjar, H. C. Aderhold and K. C. Hover, "The application of neutron radiography to the study of microcracking in concrete," *Cement, Concrete and Aggregates*, vol. 8, pp. 103-109, 1986.

[66] P. Locoge, M. Massat, J. P. Ollivier and C. Richet, "Ion diffusion in microcracked concrete," *Cem. Concr. Res.,* vol. 22, pp. 431-438, 1992.

[67] R. Jones, *Non-Destructive Testing of Concrete.* University Press, 1962.

[68] ASTM C597-09, "Standard Test Method for Pulse Velocity Through Concrete," *Annual Book of ASTM Standards,* vol. 4, .

[69] G. Trtnik, F. Kavčič and G. Turk, "Prediction of concrete strength using ultrasonic pulse velocity and artificial neural networks," *Ultrasonics,* vol. 49, pp. 53-60, 1, 2009.

[70] S. Mindess, "Acoustic emission and ultrasonic pulse velocity of concrete," *International Journal of Cement Composites and Lightweight Concrete*, vol. 4, pp. 173-179, 8, 1982.

[71] J. H. Bungey, "The validity of ultrasonic pulse velocity testing of in-place concrete for strength," *NDT International,* vol. 13, pp. 296-300, 12, 1980.

[72] S. Popovics, J. L. Rose and J. S. Popovics, "The behaviour of ultrasonic pulses in concrete," *Cem. Concr. Res.,* vol. 20, pp. 259-270, 1990.

[73] R. Jones, "A method of studying the formation of cracks in a material subjected to stress," *British Journal of Applied Physics*, vol. 3, pp. 229, 1952.

[74] I. O. Yaman, N. Hearn and H. M. Aktan, "Active and non-active porosity in concrete Part I: Experimental evidence," *Mater. Struct.,* vol. 35, pp. 102-109, 2002.

[75] I. O. Yaman, H. M. Aktan and N. Hearn, "Active and non-active porosity in concrete part II: evaluation of existing models," *Mater. Struct.,* vol. 35, pp. 110-116, 2002.

[76] S. Popovics and J. S. Popovics, "A critique of the ultrasonic pulse velocity method for testing concrete," *NDT and E International,* vol. 30, pp. 260-260, 1997.

[77] S. F. Selleck, E. N. Landis, M. L. Peterson, S. P. Shah and J. D. Achenbach, "Ultrasonic investigation of concrete with distributed damage," *ACI Mater. J.,* vol. 95, 1998.

[78] I. E. Shkolnik, O. Udegbunam and H. M. Aktan, "Ultrasonic methods of evaluating concrete permeability," in *Proc. of the Conference on NDT in Civil Engineering,* pp. 111-120.

[79] Z. Lafhaj, M. Goueygou, A. Djerbi and M. Kaczmarek, "Correlation between porosity, permeability and ultrasonic parameters of mortar with variable water/cement ratio and water content," *Cem. Concr. Res.,* vol. 36, pp. 625-633, 2006.

[80] S. Popovics and J. S. Popovics, "Effect of stresses on the ultrasonic pulse velocity in concrete," *Mater. Struct.,* vol. 24, pp. 15-23, 1991.

[81] C. L. Nogueira and K. J. Willam, "Ultrasonic testing of damage in concrete under uniaxial compression," *ACI Mater. J.,* vol. 98, 2001.

[82] T. T. Wu and T. F. Lin, "The stress effect on the ultrasonic velocity variations of concrete under repeated loading," *ACI Mater. J.,* vol. 95, 1998.

[83] Z. N. Radaković-Guzina, "Ultrasonic assessment of damage in concrete under axial loads," 1997.

[84] B. P. Flannery, H. W. Deckman, W. G. Roberge and K. L. D'amico, "Three-dimensional X-ray microtomography," *Science,* vol. 237, pp. 1439, 1987.

[85] National Library of Medicine, "Medical Subject Headings (MeSH)," 2011.

[86] D. P. Bentz, D. A. Quenard, H. M. Kunzel, J. Baruchel, F. Peyrin, N. S. Martys and E. J. Garboczi, "Microstructure and transport properties of porous building materials. II: Three-dimensional X-ray tomographic studies," *Mater. Struct.,* vol. 33, pp. 147-153, 2000.

[87] H. E. Martz, D. J. Scheberk, G. P. Roberson and P. J. M. Monteiro, "Computerized tomography analysis of reinforced concrete," *ACI Mater. J.,* vol. 90, 1993.

[88] I. L. Morgan, H. Ellinger, R. Klinksiek and J. N. Thompson, "Examination of concrete by computerized tomography," vol. 77, 1980.

[89] N. Shashidhar, "X-ray tomography of asphalt concrete," *Transportation Research Record: Journal of the Transportation Research Board,* vol. 1681, pp. 186-192, 1999.

[90] E. N. Landis, A. L. Petrell, S. Lu and E. N. Nagy, "Examination of pore structure using three-dimensional image analysis of microtomographic data," *Concrete Science and Engineering(France),* vol. 2, pp. 162-169, 2000.

[91] D. P. Bentz, N. S. Martys, P. Stutzman, M. S. Levenson, E. J. Garboczi, J. Dunsmuir and L. M. Schwartz, "X-ray microtomography of an ASTM C109 mortar exposed to sulfate attack," in *MATERIALS RESEARCH SOCIETY SYMPOSIUM PROCEEDINGS,* 1995, pp. 77-77.

[92] S. R. Stock, N. K. Naik, A. P. Wilkinson and K. E. Kurtis, "X-ray microtomography (microCT) of the progression of sulfate attack of cement paste," *Cem. Concr. Res.,* vol. 32, pp. 1673-1675, 2002.

[93] N. N. Naik, A. C. Jupe, S. R. Stock, A. P. Wilkinson, P. L. Lee and K. E. Kurtis, "Sulfate attack monitored by microCT and EDXRD: influence of cement type, water-to-cement ratio, and aggregate," *Cem. Concr. Res.,* vol. 36, pp. 144-159, 2006.

[94] T. J. Chotard, M. P. Boncoeur-Martel, A. Smith, J. P. Dupuy and C. Gault, "Application of X-ray computed tomography to characterise the early hydration of calcium aluminate cement," *Cement and Concrete Composites,* vol. 25, pp. 145-152, 1, 2003.

[95] L. Helfen, F. Dehn, P. Mikulik and T. Baumbach, "Synchrotron-radiation X-ray tomography: a method for the 3D verification of cement microstructure and its evolution during hydration," *SPECIAL PUBLICATION-ROYAL SOCIETY OF CHEMISTRY*, vol. 292, pp. 89-100, 2004.

[96] E. Gallucci, K. Scrivener, A. Groso, M. Stampanoni and G. Margaritondo, "3D experimental investigation of the microstructure of cement pastes using synchrotron X-ray microtomography ([mu] CT)," *Cem. Concr. Res.*, vol. 37, pp. 360-368, 2007.

[97] D. P. Bentz, S. Mizell, S. Satterfield, J. Devaney, W. George, P. Ketcham, J. Graham, J. Porterfield, D. Quenard and F. Vallee, "The visible cement data set," *Journal of Research of the National Institute of Standards and Technology,* vol. 107, pp. 137-148, 2002.

[98] S. Lu, E. N. Landis and D. T. Keane, "X-ray microtomographic studies of pore structure and permeability in Portland cement concrete," *Mater. Struct.*, vol. 39, pp. 611-620, 2006.

[99] E. Nagy, "Application of x-ray microtomography to the three-dimensional study of concrete fracture energy," 1998.

[100] E. N. Landis, E. N. Nagy, D. T. Keane and G. Nagy, "Technique to measure 3d work-of-fracture of concrete in compression," *J. Eng. Mech.*, vol. 125, pp. 599, 1999.

[101] E. N. Landis and E. N. Nagy, "Three-dimensional work of fracture for mortar in compression," *Eng. Fract. Mech.*, vol. 65, pp. 223-234, 2000.

[102] E. N. Landis, E. N. Nagy and D. T. Keane, "Microstructure and fracture in three dimensions," *Eng. Fract. Mech.*, vol. 70, pp. 911-925, 2003.

[103] E. N. Landis, "Damage variables based on three-dimensional measurements of crack geometry," *Strength, Fracture and Complexity*, vol. 3, pp. 163-173, 2005.

[104] E. N. Landis, T. Zhang, E. N. Nagy, G. Nagy and W. R. Franklin, "Cracking, damage and fracture in four dimensions," *Mater. Struct.*, vol. 40, pp. 357-364, 2007.

[105] ASTM C270-10., "Standard Specification for Mortar for Unit Masonry," 2010.

[106] ASTM C1437-07, "Standard Test Method for Flow of Hydraulic Cement Mortar," *ASTM International*, .

[107] T. H. Ahmed, *Reservoir Engineering Handbook.* Gulf Professional Pub., 2006.

[108] ASTM C617-10, "Standard Practice for Capping Cylindrical Concrete Specimens," 2010.

[109] ASTM C469., "Standard Test Method for Static Modulus of Elasticity and Poisson's Ratio of Concrete in Compression," .

[110] R. C. Gonzalez and R. E. Woods, *Digital Image Processing.* 2002.

[111] Z. Zhang, F. Ansari and N. Vitillo, "Automated determination of entrained air-void parameters in hardened concrete," *ACI Mater. J.*, vol. 102, 2005.

[112] H. Toutanji, S. McNeil and Z. Bayasi, "Chloride permeability and impact resistance of polypropylene-fiber-reinforced silica fume concrete," *Cem. Concr. Res.,* vol. 28, pp. 961-968, 7, 1998.

[113] M. Nagabhushanam, V. Ramakrishnan and G. Vondran, "Fatigue Strength of Fibrillated Polypropylene Fiber Reinforced Concretes," *Transp. Res. Rec.,* 1989.

[114] ACI 2010, "ACI Concrete Terminology," 2010.

[115] J. Simo and J. Ju, "Strain-and stress-based continuum damage models--I. Formulation," *Int. J. Solids Structures,* vol. 23, pp. 821-840, 1987.

[116] W. R. Franklin, "CONNECT - Find 3D Connected Components," 1999.

[117] L. He, Y. Chao, K. Suzuki and K. Wu, "Fast connected-component labeling," *Pattern Recognit,* vol. 42, pp. 1977-1987, 2009.

[118] N. Negroponte, "Raster scan approaches to computer graphics," *Comput. Graph.,* vol. 2, pp. 179-193, 1977.

[119] K. Suzuki, I. Horiba and N. Sugie, "Linear-time connected-component labeling based on sequential local operations," *Comput. Vision Image Understanding,* vol. 89, pp. 1-23, 2003.

[120] J. Hudson, "Wave speeds and attenuation of elastic waves in material containing cracks," *Geophysical Journal of the Royal Astronomical Society,* vol. 64, pp. 133-150, 1981.

[121] S. Popovics, *Strength and Related Properties of Concrete: A Quantitative Approach.* John Wiley & Sons Inc, 1998.

[122] C. David, T. F. Wong, W. Zhu and J. Zhang, "Laboratory measurement of compaction-induced permeability change in porous rocks: Implications for the generation and maintenance of pore pressure excess in the crust," *Pure Appl. Geophys.*, vol. 143, pp. 425-456, 1994.

[123] J. P. Evans, C. B. Forster and J. V. Goddard, "Permeability of fault-related rocks, and implications for hydraulic structure of fault zones," *J. Struct. Geol.*, vol. 19, pp. 1393-1404, 1997.

[124] S. Takahashi and R. Motegi, "Stress dependency on ultrasonic wave propagation velocity," *J. Mater. Sci.*, vol. 22, pp. 1850-1856, 1987.

Appendix A

Fast Connected Component Labeling Code Used for Labeling the Connected Components

```
/***********************************************************************
*****

 Program Name: flccl.c Ver.1.0.0

 Authors      : Lifeng He, Ph.D. & Kenji Suzuki, Ph.D.

              : Department of Radiology, The University of Chicago

 Date Created: 10/08, 2006

 Description: Fast linear-time connected-component labeling algorithm.

 Reference    : He L., Chao Y., Suzuki K., and Wu K.,  • Fast connected-component
labeling. • h Pattern Recognition, vol. 42, pp. 1977-1987, 2009.

 Related References: He L., Chao Y., and Suzuki K.,  • A run-based two-scan labeling
algorithm. • h IEEE Transactions on Image Processing, vol. 17, pp. 749-756, 2008.

                 : Suzuki K., Horiba I., and Sugie N.,  • Linear-time connected-component
labeling based on sequential local operations. • h Computer Vision and Image
Understanding, vol. 89, pp. 1-23, 2003.

***********************************************************************
****/
```

```
#include <stdio.h>

#include <math.h>

#include <stdlib.h>

#include <time.h>

#include <string.h>


#define XSIZE_MAX 4096

#define YSIZE_MAX 4096

#define TMAX 1048576     /* the maximum number of provisional labels */

#define FB 0

#define FO 1

#define SUCCESSIVE_NUM 1  /* When the successive numbers for connected
components
                          are needed, it is on. */


int img[YSIZE_MAX*XSIZE_MAX];

######################################################

int xsize, ysize, label;

char output_img_name[256];

int newl, no_of_components;
```

```
#######################################################

void iinit1(int *, int, int);

int read_pbm_img(char *, int *, int *, int *);
#######################################################
#######################################################
int output_img(char *, int *, int, int);

int main(int argc, char *argv[])
{
  int   i, j, k;
  int   dat;
  int   c0, c1, c2, c3, c4, c5;
  double t0, t1, t2, t3;
  char buf[256];
  int x, y;
  char c;

  FILE  *fp, *fq;
```

```
t0 = (double)clock()/CLOCKS_PER_SEC;

if(argc==1) {
  printf("\n USAGE:  flccl-4096 imagename.pbm  \n\n");
  exit(0);
}

label=1;

fq = fopen(argv[1], "r");

if(fq == NULL) {
  printf(" \n %s does not exist!\n\n", argv[1]);
  return -1;
}

do {
  fgets(buf, 256, fq);
} while(buf[0] == '#');  // skip over comments

if(buf[0] != 'P' || buf[1] != '1') {
```

```
  fclose(fq);
  printf(" \n The input image is not binary ascii PBM format! \n\n");
  return -1;
}

do {
  fgets(buf, 256, fq);
} while(buf[0] == '#'); // skip over comments
sscanf(buf, "%d %d", &xsize, &ysize);
//  printf("%d %d\n", xsize, ysize);

i=0;
while((c=fgetc(fq))!=EOF){
  if(c=='0'){
    img[i]=0;
    i++;
  }
  else if(c=='1'){
    img[i]=1;
    i++;
  }
```

```
  //    printf("%d", img[i-1]);
 }
 //  printf("%d\n", i);


 fclose(fq);


 t1 = (double)clock()/CLOCKS_PER_SEC;


 c5=xsize*(ysize-1)-1;


 for(c4=xsize; c4 < c5; c4++){
  //    printf("%d ", img[c4]);
  if(img[c4]!=FB){
    if(img[c4-xsize]!=FB){
        img[c4]=img[c4-xsize];
    }
    else if(img[c4-1]!=FB){
        img[c4]=img[c4-1];
        if(img[c4-xsize+1]!=FB){
########################################################
        }
```

```
    }
    else if(img[c4-xsize-1]!=FB){
        img[c4]=img[c4-xsize-1];
        if(img[c4-xsize+1]!=FB){
########################################################
        }
    }
    else if(img[c4-xsize+1]!=FB){
        img[c4]=img[c4-xsize+1];
    }
    else{
        //img[c4] = list_last[label] = ctbl[label] = label;
        img[c4] = label;
########################################################
########################################################
########################################################
        label++;
        //                              printf("%d ", label);
    }
  }
 }
```

```
// }
/* the second scan, rewrite pixels with the corresponding label. */
if(SUCCESSIVE_NUM){
  /* Arrange labels. Making the number for different connected components in
   output images from 1 to 'label', where 'label' is the number of the
   connected components in the images
  */
  iinit1(arr, label, 0);
  newl = 1;
  for (c4=xsize; c4<c5; c4++) {
    dat=ctbl[img[c4]];
    if (dat != FB){
        if (arr[dat] != 0) {
          img[c4] = arr[dat];
        }
        else {
          arr[dat] = newl;
          img[c4] = newl;
          newl++;
        }
```

```
    }
  }
}
else{
  for (c4=xsize; c4<c5; c4++) {
    img[c4] = ctbl[img[c4]]; // replaced by the label corresponding to the label j, ctbl[j]
  }
  no_of_components=compute_no_of_components(label);
}

t2 = (double)clock()/CLOCKS_PER_SEC;

output_img(argv[1], img, xsize, ysize);

t3 = (double)clock()/CLOCKS_PER_SEC;

printf("\n");
printf("Labeling connected components in [%15s]......  \n\n", argv[1]);
printf("          Running time for labeling: %5.5lf[sec]   \n",  (t2-t1));
printf("Running time with input and output: %5.5lf[sec]  \n",  (t3-t0));
```

```
  if(SUCCESSIVE_NUM){
    printf("    Number of connected components: %d \n", newl-1);
  }
  else{
    printf("    Number of connected components: %d \n", no_of_components);
  }
  printf("      Number of previsional labels: %d \n", label-1);
  printf("                   The output file: %s \n", output_img_name);
}

########################################################
########################################################
  int k;

  if(i<j) {  //if Sj is combined to Si
    k=j;

    do{
      //no_of_resolve++;
      ctbl[k]=i;
      k=list_next[k];
```

```
    }while(k!=-1); // until list ends

##########################################################
##########################################################
##########################################################
  }
  else if(i>j) {  //Si is combined into Sj
    k=i;

    do {
      //no_of_resolve++;
      ctbl[k]=j;
      k=list_next[k];
    }while(k!=-1);

    list_next[list_last[j]]=i;
    list_last[j]=list_last[i];
  }
}

##########################################################
```

```
  int i, no=0;


  for(i=0; i < label; i++) {        // a list is corresponding to a component
#######################################################
      no++;      //  increase the number of lists
    }
  }
  return no;
}



int   output_img(char *img_in_name, int *img, int xsize,int ysize)
{
  FILE  *fpo;
  int i=0, k;


  while(img_in_name[i]!='.'){
    output_img_name[i]=img_in_name[i];
    i++;
  }
  output_img_name[i]='\0';
```

```
strcat(output_img_name, ".labeled");

if ((fpo=fopen(output_img_name, "wb")) == NULL) {
  printf("Writing file open error ! %s\n", output_img_name);
  return((int)NULL);
}
else {
  k=1;
  for(i=0; i<xsize*ysize; i++){
    if(k==xsize){
           fprintf(fpo, "%d\n", img[i]);
      k=1;
    }
    else{
           fprintf(fpo, "%d ", img[i]);
           k++;
    }
  }
  fclose(fpo);
}
```

```
}

/****** Initialize 1-D int type array . ******/
void iinit1(int *img, int size, int cnst)
    /*** Input and output variables ***/
    /*int   *img;/* An int type image. */
    /*** Output variables ***/
    /*** Input variables ***/
    /*int   size;/* Size of an image. */
    /*int   cnst;*/
{
  /*** Local variables ***/
  int   i;/* Loop counter. */
  for(i=0; i<size; i++)
    *(img + i) = cnst;
```

Appendix B

The cross sections of plain and fiber reinforced mortars analyzed to calculate the number and percentage of connected pores

Plain Mortar (Top section)

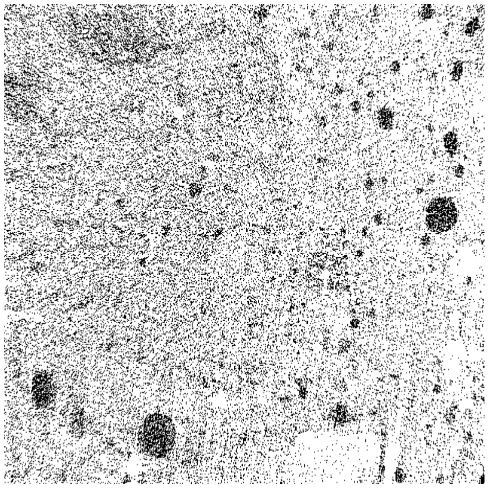

(a) 0% f'_c

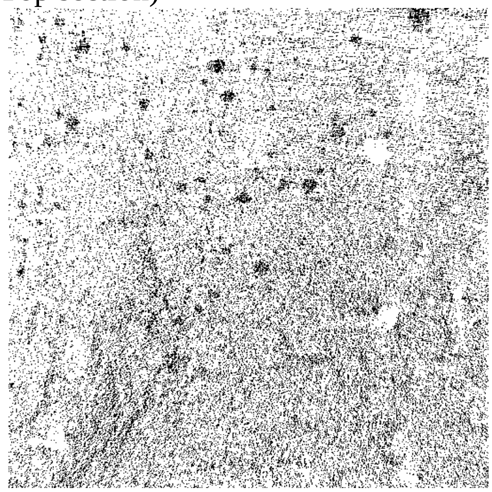

(b): 29% f'_c

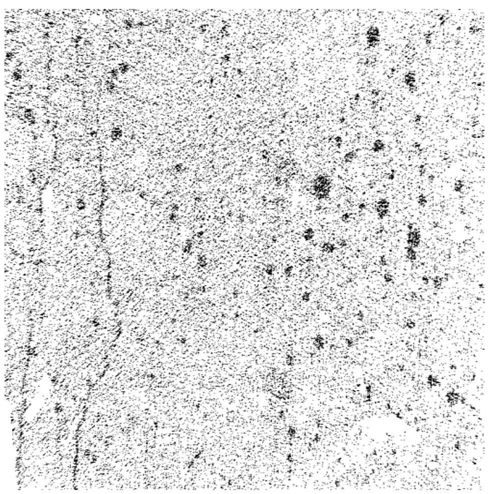

(c): 59% f'_c

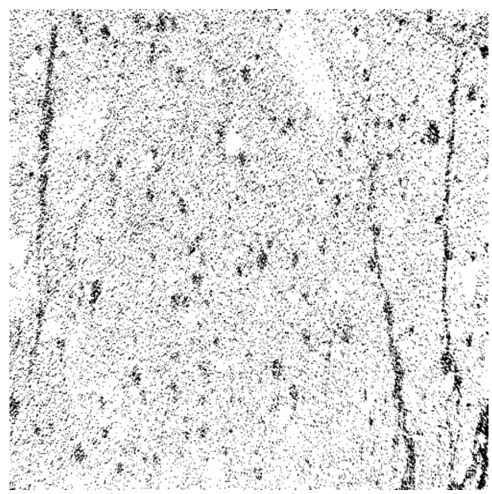

(d): 88% f'_c

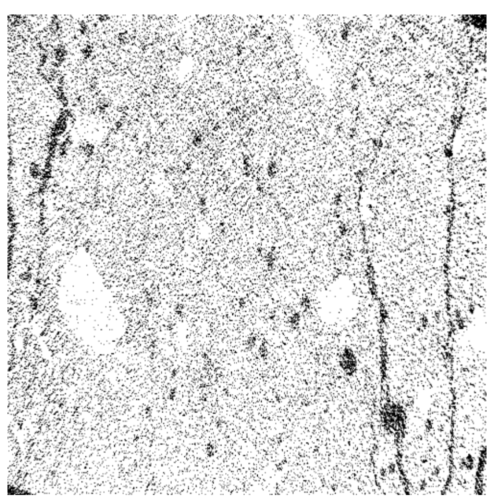

(e): 100% f'_c

Plain Mortar (Middle Section)

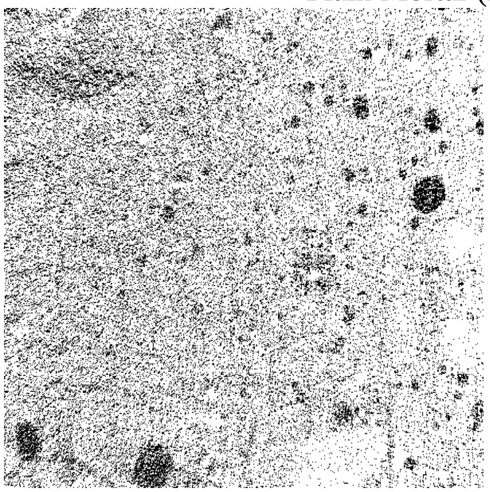

(a): 0% f'_c

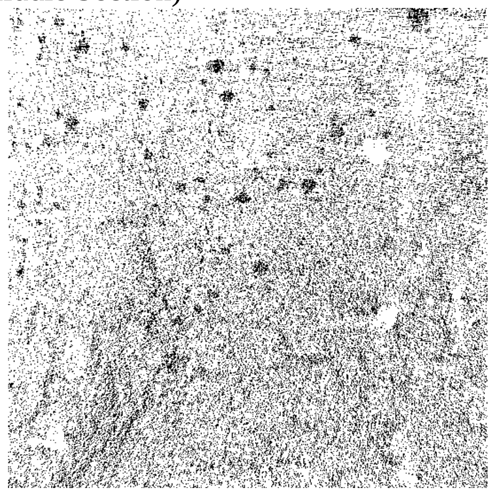

(b): 29% f'_c

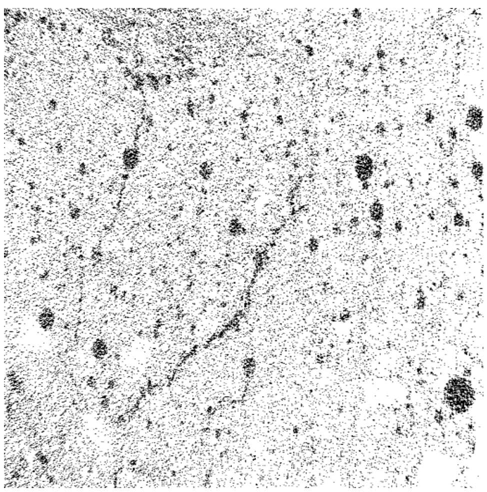

(c): 58% f'_c

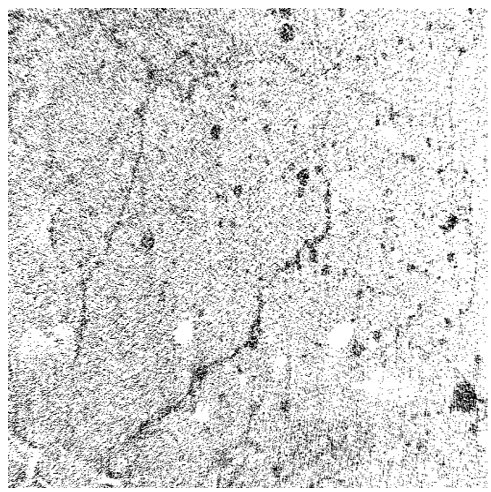

(d): 88% f'_c

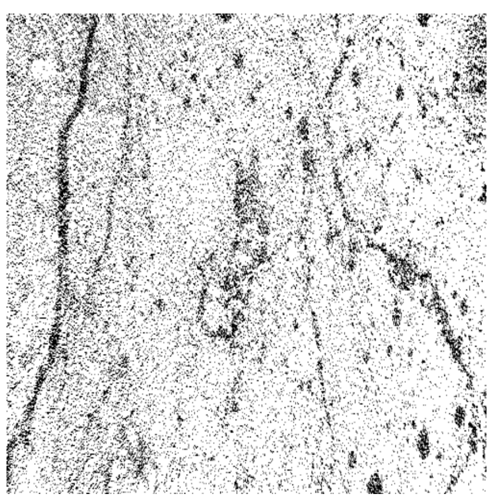

(e): 100% f'_c

Plain Mortar (Bottom Section)

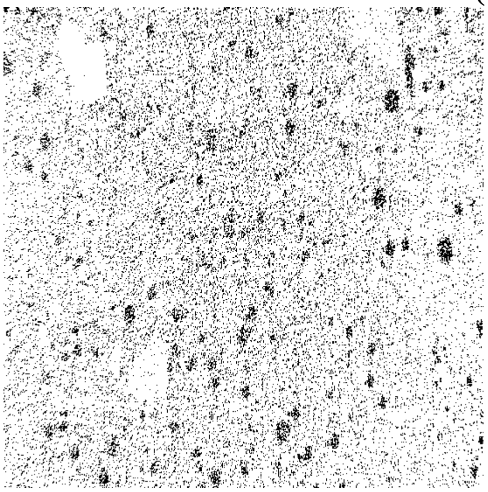

(a): 0% f'$_c$

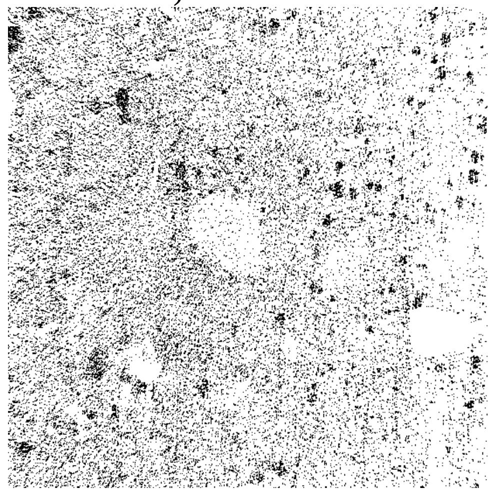

(b): 29% f'$_c$

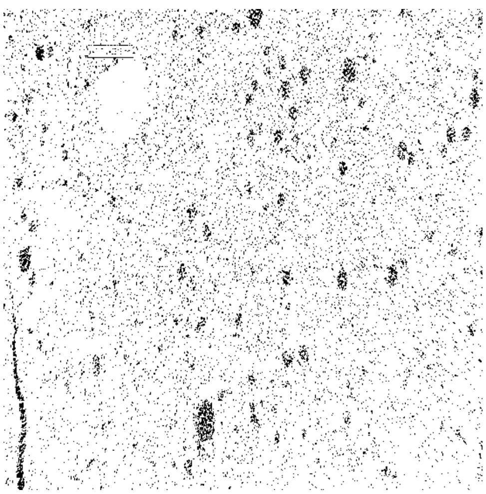

(c): 59% f'$_c$

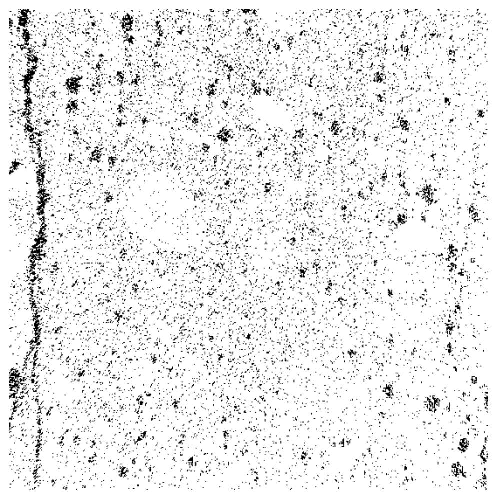

(d): 88% f'$_c$

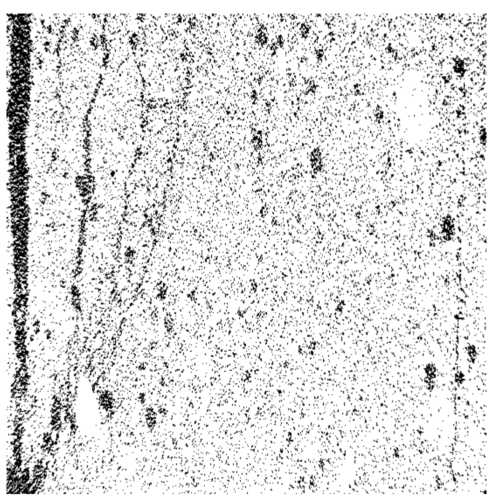

(e): 100% f'$_c$

Fiber Reinforced Mortar (Top section)

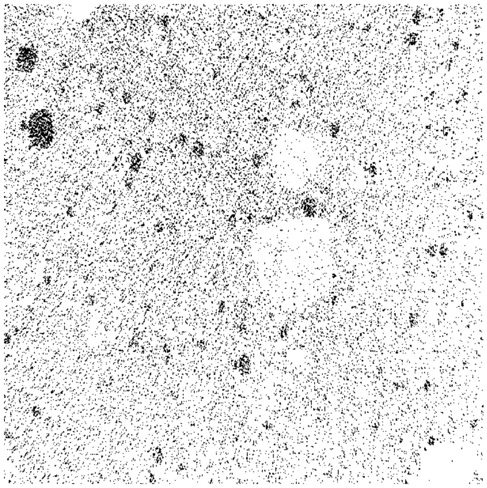

(a): 0% f'_c

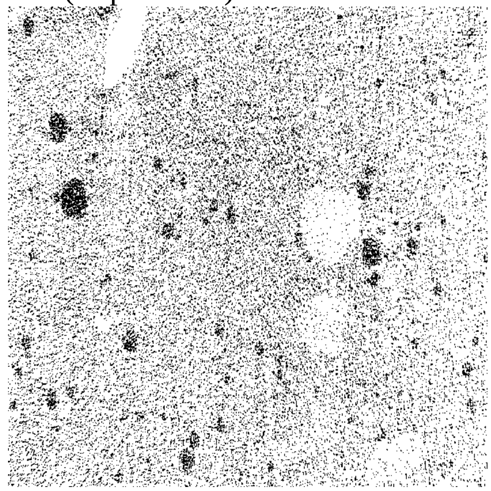

(b): 22% f'_c

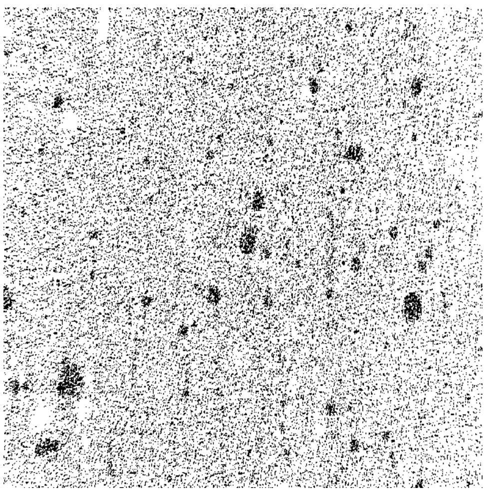

(c): 44% f'_c

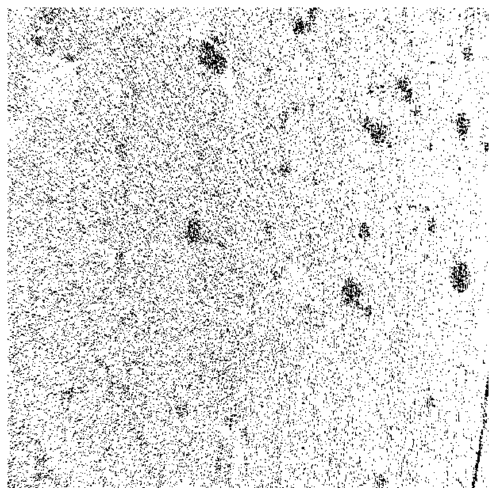

(d): 67% f'_c

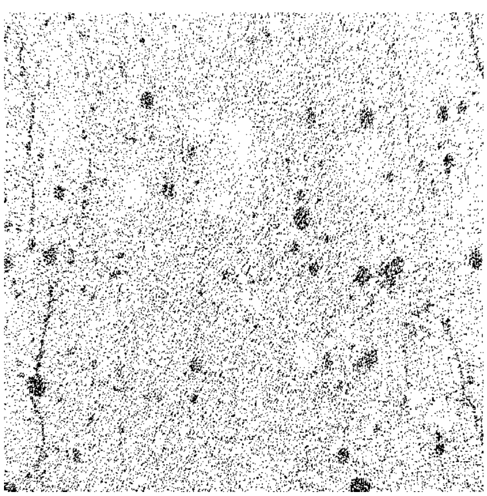

(e): 89% f'_c

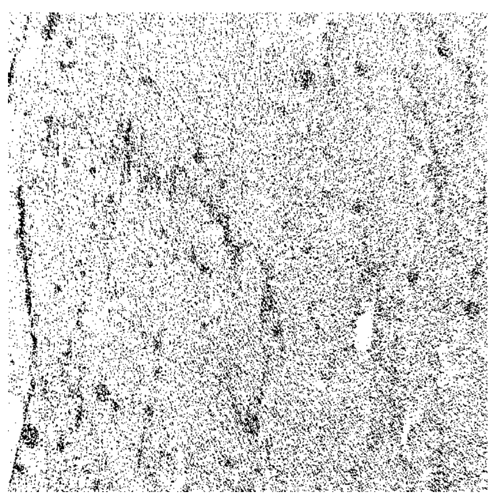

(f): 100% f'_c

Fiber Reinforced Mortar (Middle section)

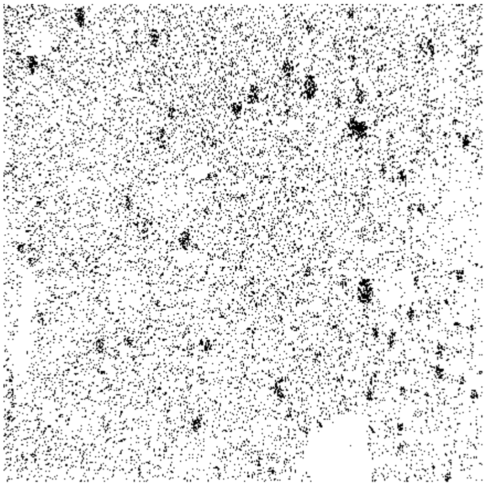

(a) 0% f'_c

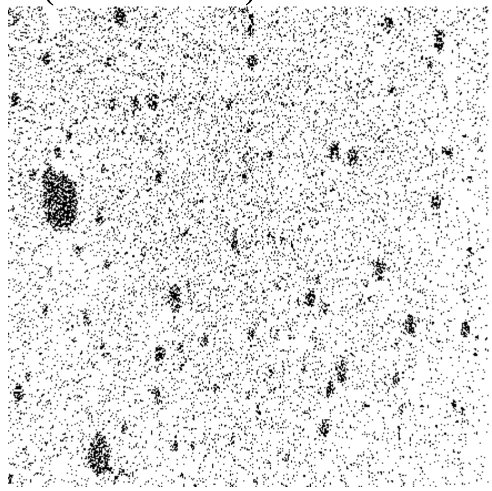

(b): 22% f'_c

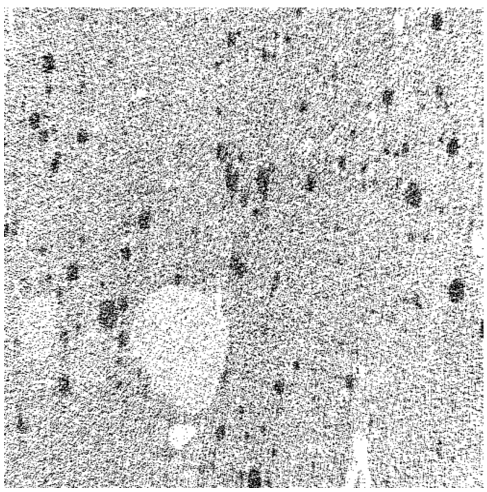

(c): 44% f'_c

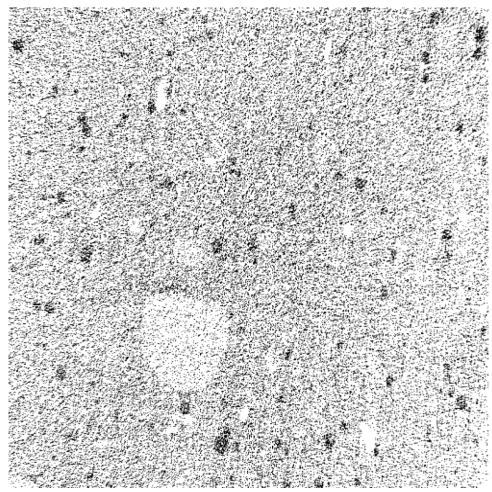

(d): 67% f'_c

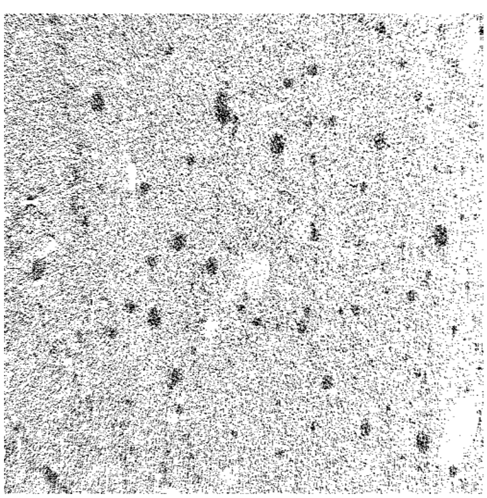

(e): 89% f'_c

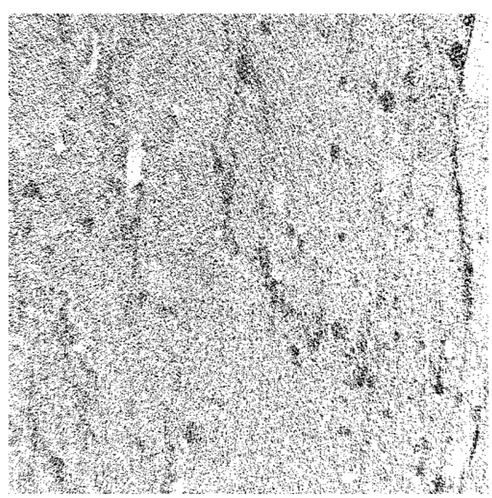

(f): 100% f'_c

Fiber Reinforced Mortar (bottom section)

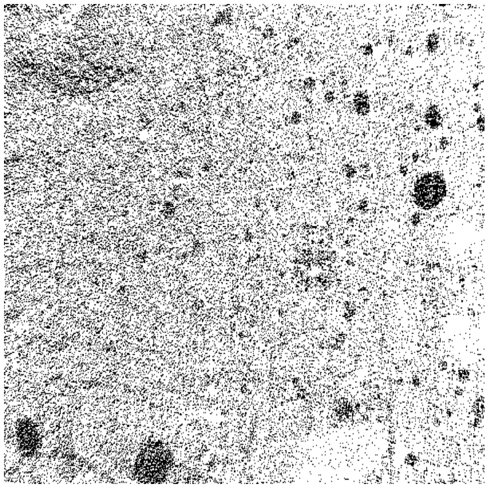

(a): 0% f'_c

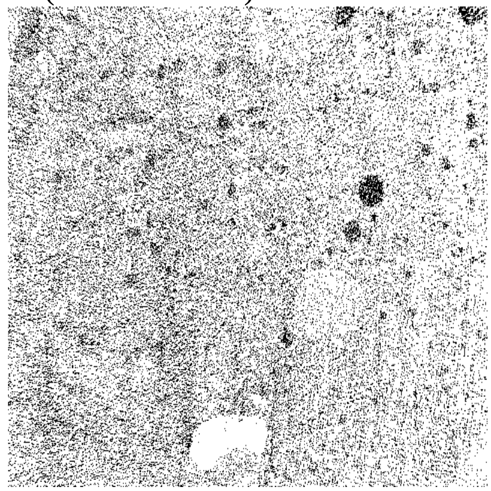

(b): 22% f'_c

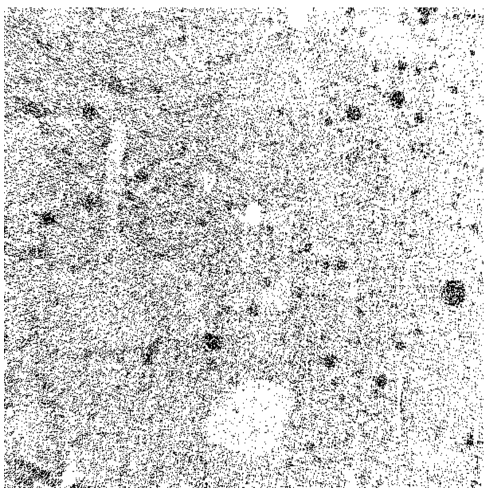

(c): 44% f'_c

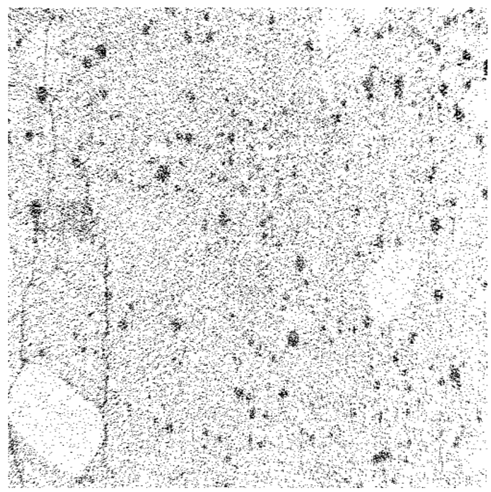

(d): 67% f'_c

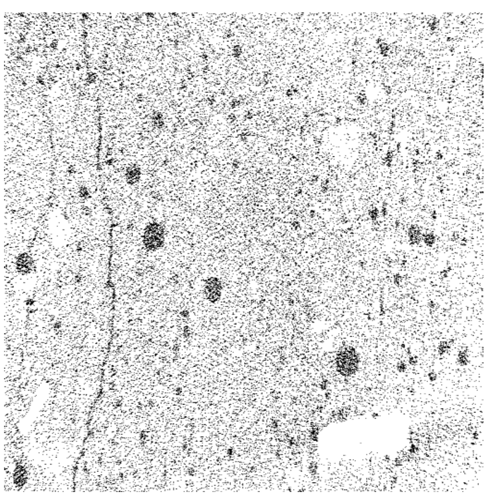

(e): 89% f'_c

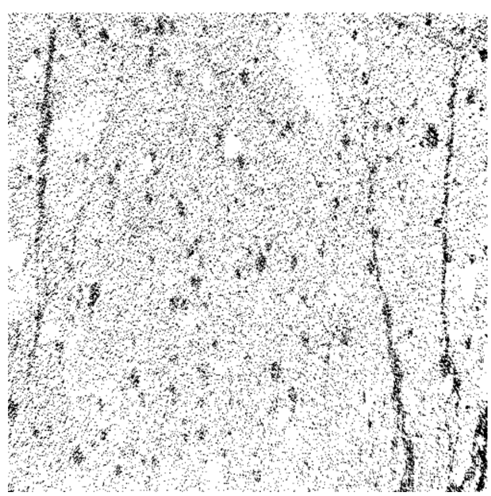

(f): 100% f'_c